TECHNICAL REPORT
(Fourth Annual Progress Report for the period
February 1, 1967 - January 31, 1968)

DETONATIONS IN TWO PHASE MEDIA AND DROP SHATTERING STUDIES

by

E. K. Dabora, K. W. Ragland, and A. A. Ranger

J. A. Nicholls
Principal Faculty Investigator

prepared for

NATIONAL AERONAUTICS AND SPACE ADMINISTRATION

May 1968

Department of Aerospace Engineering
UNIVERSITY OF MICHIGAN
Ann Arbor, Michigan

FOREWORD

This report covers the progress made from February 1, 1967 to January 31, 1968 on a continuing study of the relation of two-phase detonations to liquid rocket motor instability under NASA Contract NASr 54(07). The study is under the direction of Professor J.A. Nicholls, Department of Aerospace Engineering. Mr. Bruce Clark of NASA Lewis Research Center, is the technical monitor.

ACKNOWLEDGMENT

The authors wish to thank D. Giere, H. Radcliff, R. Stitt, C. Smith and W. Whitman for their assistance in carrying out the experiments and in data reduction. Mr. Stitt was also of considerable help in the preparation of this report which was expertly typed by Mrs. E. Sherbrook.

TABLE OF CONTENTS

ABSTRACT

Recent experimental results on detonations in two phase mixtures of liquid fuel and gaseous oxygen are presented. The fuel (diethylcyclohexane) was in either a spray form or liquid film on the walls of the detonation tube. For the spray case three drop sizes were used: $290\,\mu$, $940\,\mu$, and $2600\,\mu$. It is found that the smaller the drop size, the faster the detonation develops into a steady-state. The steady velocity is found to be lower than the ideal Chapman-Jouguet velocity. The difference is 2-10% for the $290\,\mu$ and $940\,\mu$ sprays and 30-35% for the $2600\,\mu$. Heat transfer measurements and inferred frictional losses to the walls are used in conjunction with a reaction length controlled by the breakup of the drops to arrive at a relationship that shows a direct dependence of velocity difference on the drop size. The calculated differences are 4%, 10%, and 26% for the $290\,\mu$, $940\,\mu$, and $2600\,\mu$ sprays respectively.

New photographs of the detonation phenomenon in a single stream of $2600\,\mu$ drops show that the combustion in the wake of the drops results in explosions that feed the main front. Pressure peaks behind the front confirm this observation.

Detonation velocities of a fuel film along one wall and two walls of the square tube are also lower than the ideal Chapman-Jouguet velocities. The velocity in the one wall case was lower than the two walls case even though the mixture ratio in the former was slightly higher. Streak schlieren and direct luminosity photographs show ignition delays of 28-36 μsec (1 wall) and 7-19 μsec (2 walls).

Some new results on the breakup of inert drops behind shock waves based on streak photographs are also presented. The photographs allowed a quantitative definition of the breakup time which seems to correlate well with previous, rather subjective estimates. An analytical treatment of the breakup phenomenon based on a boundary layer stripping model is made and the results are compared with the experiments.

LIST OF FIGURES

NOMENCLATURE

(A Roman numeral after a definition refers to the
section where that definition is used.)

A	dimensionless velocity at interface
a	acceleration
C_D	drag coefficient
C_H	heat transfer coefficient defined in Eq. (2.3)
c	specific heat
D	drop diameter
D_o	initial drop diameter ($t = 0$)
g	acceleration due to gravity
h_2	enthalpy behind shock
h_w	enthalpy at wall
k	constant $\simeq 5$ (II) thermal conductivity (App.)
ℓ	distance between drops
M	Mach number
M_2	Mach number of the convective flow behind a shock
M_G	Mach number of C-J detonation (equivalent all gaseous case)
M_S	Mach number of detonation in spray
M_s	shock Mach number
m	mass
m_o	initial mass of drop
P_1	pressure in driven section (IV), initial pressure (II)
$(P_3/P_1)_G$	pressure ratio across C-J detonation in spray
$(P_3/P_1)_S$	pressure ratio across C-J detonation (equivalent all gaseous case)
Q	mass flow rate per unit width of plate

q	heat transfer rate
q_D	dynamic pressure behind a detonation
q_s, q_2	dynamic pressure behind a shock
R	drop radius
Re	Reynolds number
r_h	hydraulic radius = area/perimeter
$r(x)$	radial distance from axis
S	projected surface area
$\overline{T}$	dimensionless time = $(\rho_g/\rho_\ell)^{1/2} (u_2 t/D_o)$
$\overline{T}_b$	dimensionless breakup time
T_3/T_1	static temperature ratio across C-J detonation
t	time
t_b	breakup time of drops
U	free-stream velocity
u	velocity
u_2	velocity of convective flow behind shock
u_∞	axial free-stream velocity
u_g	velocity of gas
u_ℓ	velocity of liquid
u_{mean}	mean velocity of liquid layer
u_s	detonation velocity
u_{so}	ideal detonation velocity
u_λ	velocity at free surface of film
V	velocity
W	drop velocity
We	Weber's number = $\rho_2 u_2^2 D_o/\sigma$
$\overline{X}_b$	dimensionless length at breakup
x	length
x	reaction length (II), dimensionless length = x/D_o (IV)

x_b	distance at breakup
α	angle on streak photograph (III) coefficient of resistivity (App.)
α_g	boundary layer shape factor (gas)
α_ℓ	boundary layer shape factor (liquid)
β	gas to liquid density ratio
γ	ratio of specific heats
γ_3	ratio of specific heats at C-J plane
δ_ℓ	boundary layer thickness of liquid
ϵ_b	experimental constant
λ	film thickness
μ	viscosity
ν_g	kinematic viscosity of gas
ν_ℓ	kinematic viscosity of liquid
ρ	density
ρ_1	density ahead of wave
ρ_2	density immediately behind wave
ρ_3	density at C-J plane
ρ_3/ρ_1	density ratio across C-J detonation
ρ_g	density of gas
ρ_ℓ	density of liquid
τ	time corresponding to $W = .95\, u_2$
τ_b	non-dimensional breakup time $= t_b\, u_s/D$
τ_m	non-dimensional time corresponding to maximum C_H
τ_o	shear stress
$\bar{\tau}$	non-dimensional time $= \tau\, u_2 \beta^{1/2}/D_o$
ϕ	liquid fuel/oxidizer mass ratio
χ	distance corresponding to $W = .95\, u_2$
$\bar{\chi}$	non-dimensional distance χ/D_o

I. INTRODUCTION

The work which will be described in this report represents the most recent part of our continuing effort on the study of two-phase detonations and the accompanying investigation of the breakup of liquid drops by gaseous convective flows. Our previous work on the subject has been presented in several reports[1, 2, 3] where studies similar or pertinent to the subject by other workers were also reviewed.

The main areas that will be covered in this report will be the description of the reaction zone behind the detonation wave in sprays, the effect of the drop size on the development and the velocity of the wave, the relationship between the reaction length and breakup time of the drops, a more detailed experimental investigation of the film detonation, and a treatment of a drop breakup model and its comparison with the experimental breakup results of non-burning drops under the action of convective flows generated by shock waves.

1

II. EXPERIMENTAL RESULTS ON SPRAY DETONATIONS

The experimental facility for studying two-phase detonations has been described before[3]. It consists of the following main items:

(a) a device for producing a fuel spray[4],

(b) a vertical tube (1.64 in. square x ~ 12 ft long) in which the liquid spray is mixed with the gaseous oxygen,

(c) an initiation device which consists of a gaseous $(2H_2 + O_2)$ detonation driven shock tube, and

(d) instrumentation for monitoring and observing the phenomenon; this includes streak or spark source photography, pressure transducers[5], and thin film heat transfer gauges.

A schematic diagram of the apparatus is shown in Fig. 2.1 and a schematic diagram to identify the locations in the tube where measurements are made is shown in Fig. 2.2.

1. Photographic Observations

Three drop sizes were used in the experiments, namely 290μ, 940μ, and 2600μ and the fuel was diethylcyclohexane (DECH). A picture of the spray in the test section is usually taken shortly before the detonation wave passes over it. The purpose is to allow an accurate measurement of the mixture ratio. For the smaller drops, where coalescence of the drops takes place as they fall along the tube and where some of the drops are lost by adherence to the tube walls, the photograph provides the only means of calculating the mixture ratio. On the other hand, for the larger drops where no coalescence takes place, it is possible to calculate the mixture ratio from a knowledge of the volumetric flow rate and the shedding frequency, which is the same as the vibration frequency imposed on the drop generator.
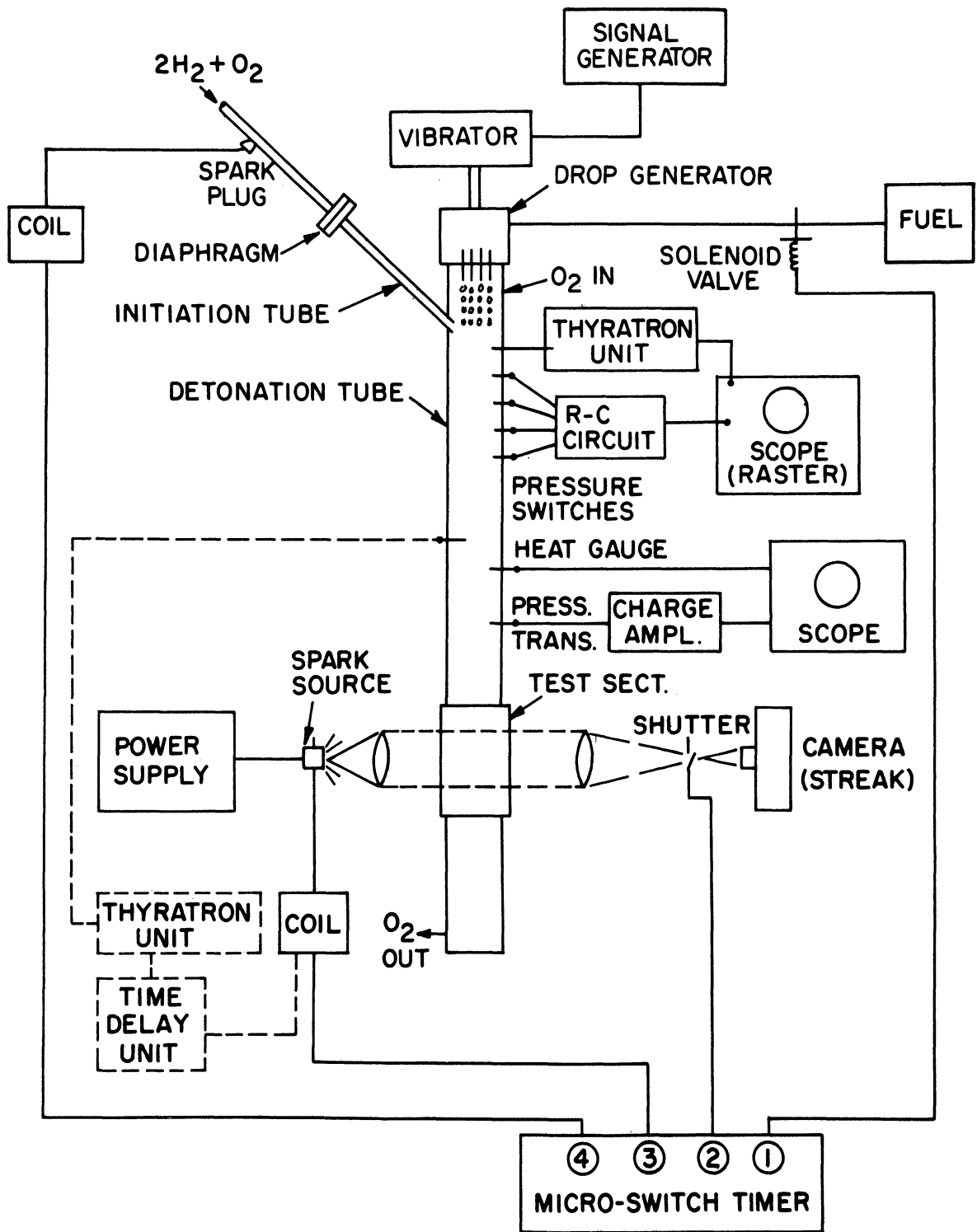
Fig. 2.1. Schematic diagram of spray detonation apparatus.

3
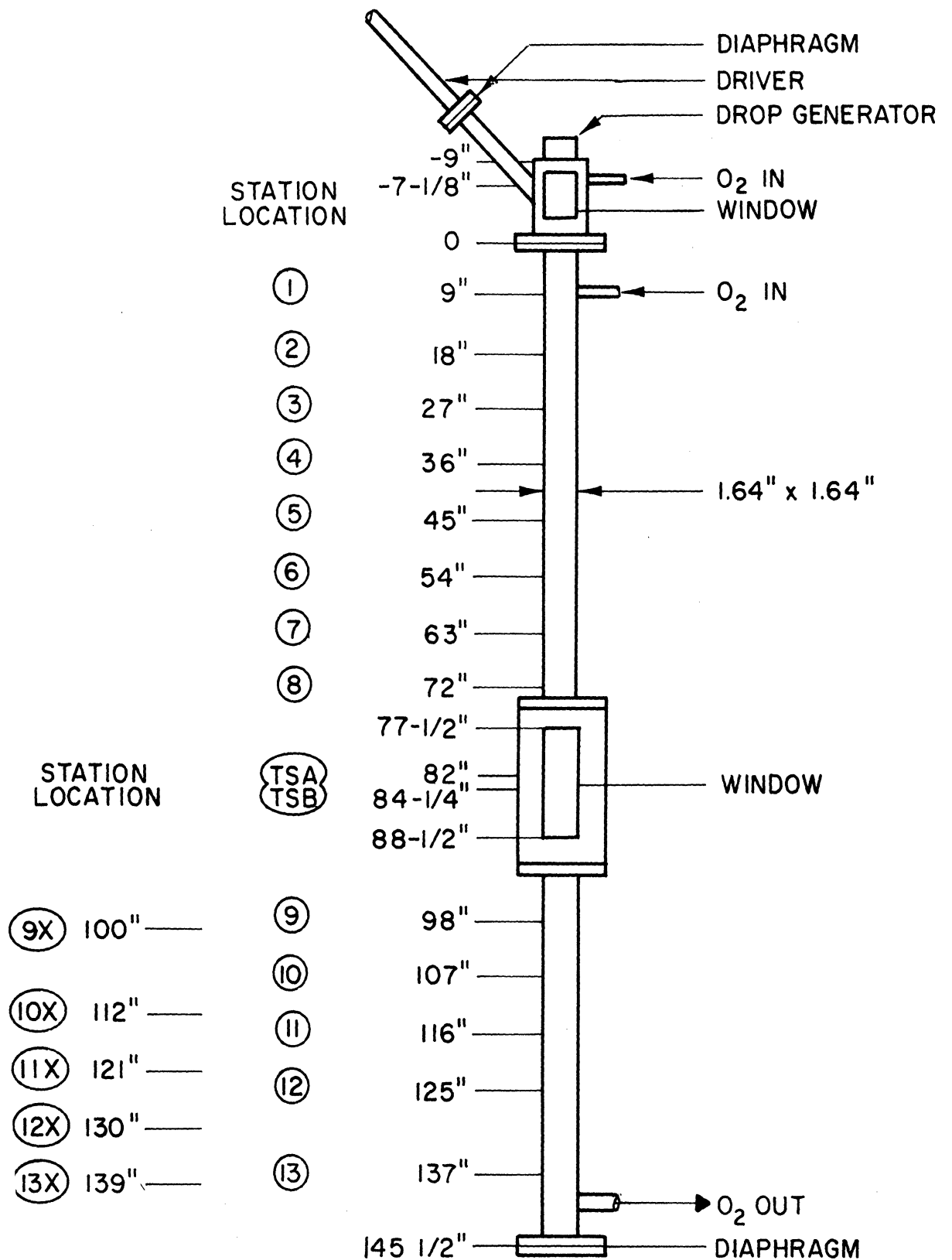
Fig. 2.2. Schematic diagram of combustion tube showing transducer locations.

Examples of streak photographs of the detonation phenomenon are shown in Fig. 2.3-2.4. Figure 2.3 is a schlieren of a detonation in a 290μ spray. The dark horizontal lines before the detonation front represent drops which happen to be in the slit and the dark zone behind the front shows the extent of the interaction between the gaseous convective flow and the drops. This zone, which is interpreted to represent the breakup time of the drop, is estimated in this example to be about 20 μsec for a detonation travelling at 5500 ft/sec. The equivalence ratio in this case is 0.3.

More details of the trajectory of the drops and their fate can be obtained from photographs of the detonation of a single stream of 2600μ drops as shown in Fig. 2.4, which is a combined shadow and direct light photograph. As the drop is passed by the main shock wave, it starts to deform instantly as can be seen from the shadow portion of the photograph. Because the convective gaseous flow is supersonic, a bow shock appears with its standoff distance increasing as the drop continues to deform. A wake behind the drop, evidently composed of small particles of fuel stripped away by the convective flow and mixed with the gaseous oxygen, starts to ignite violently and apparently obliterates the bow shock of the preceding drop. Some secondary shocks arising from the explosion of the wake can be seen in the shadow portion of the photograph. In some cases[3] it was found that combustion started at the stagnation point of the drop.

Further details of the process taking place in the tube as a whole can be obtained from spark schlieren photographs such as shown in Fig. 2.5. This figure is a composite of three photographs taken at three different time delays and arranged so as to show details for about 12 in. behind the front. The exposure time of each photograph is $\simeq 0.2$ μsec which is the duration of the spark source. To avoid over-exposure from direct radiation, an electromagnetic shutter[6] was placed at the focal point of the second schlieren lens. Details of the shutter are described in Appendix I. In Fig. 2.5, one
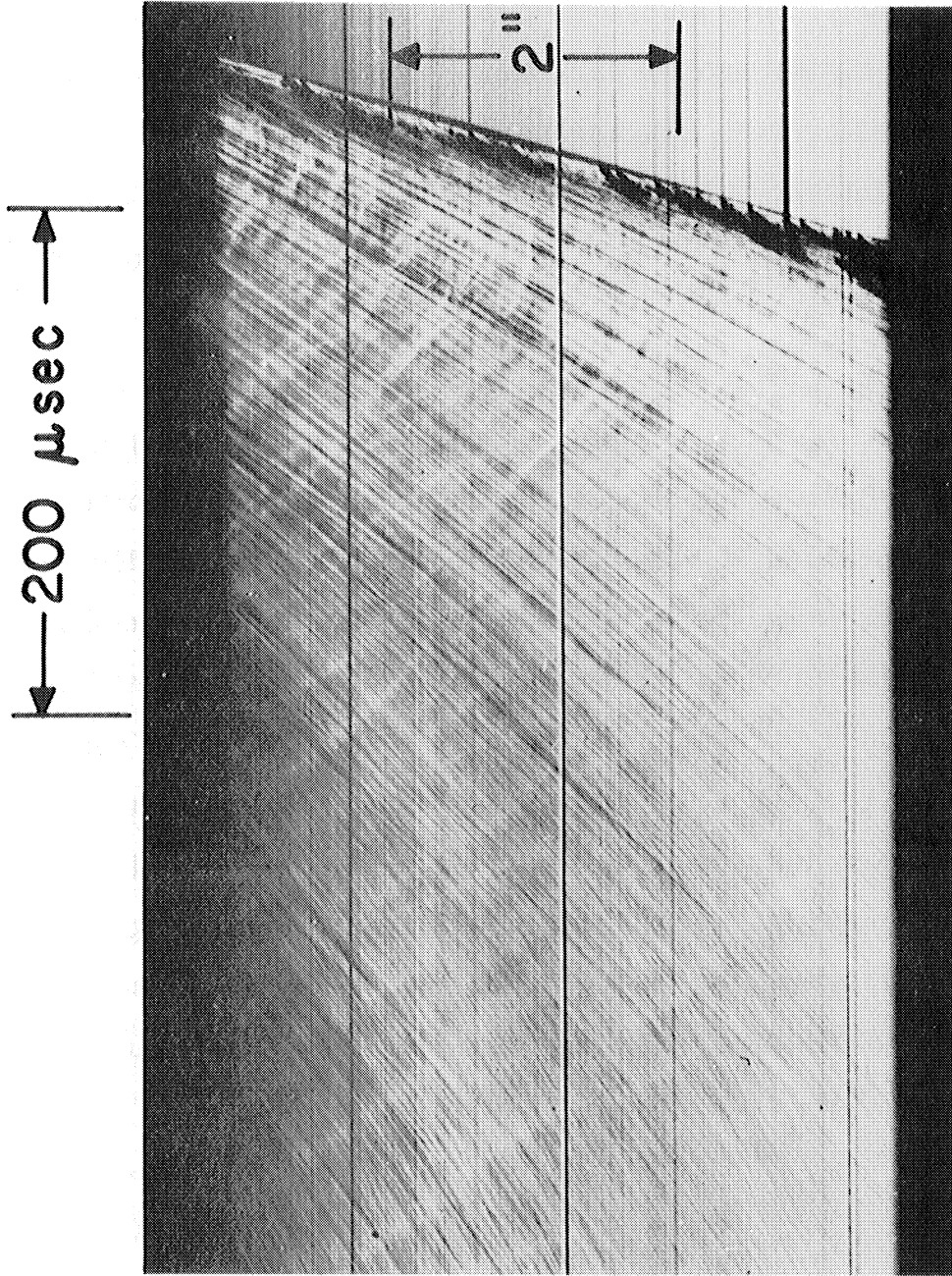
Fig. 2.3. Schlieren streak photograph of detonation in 290μ spray (run no. 380).

6
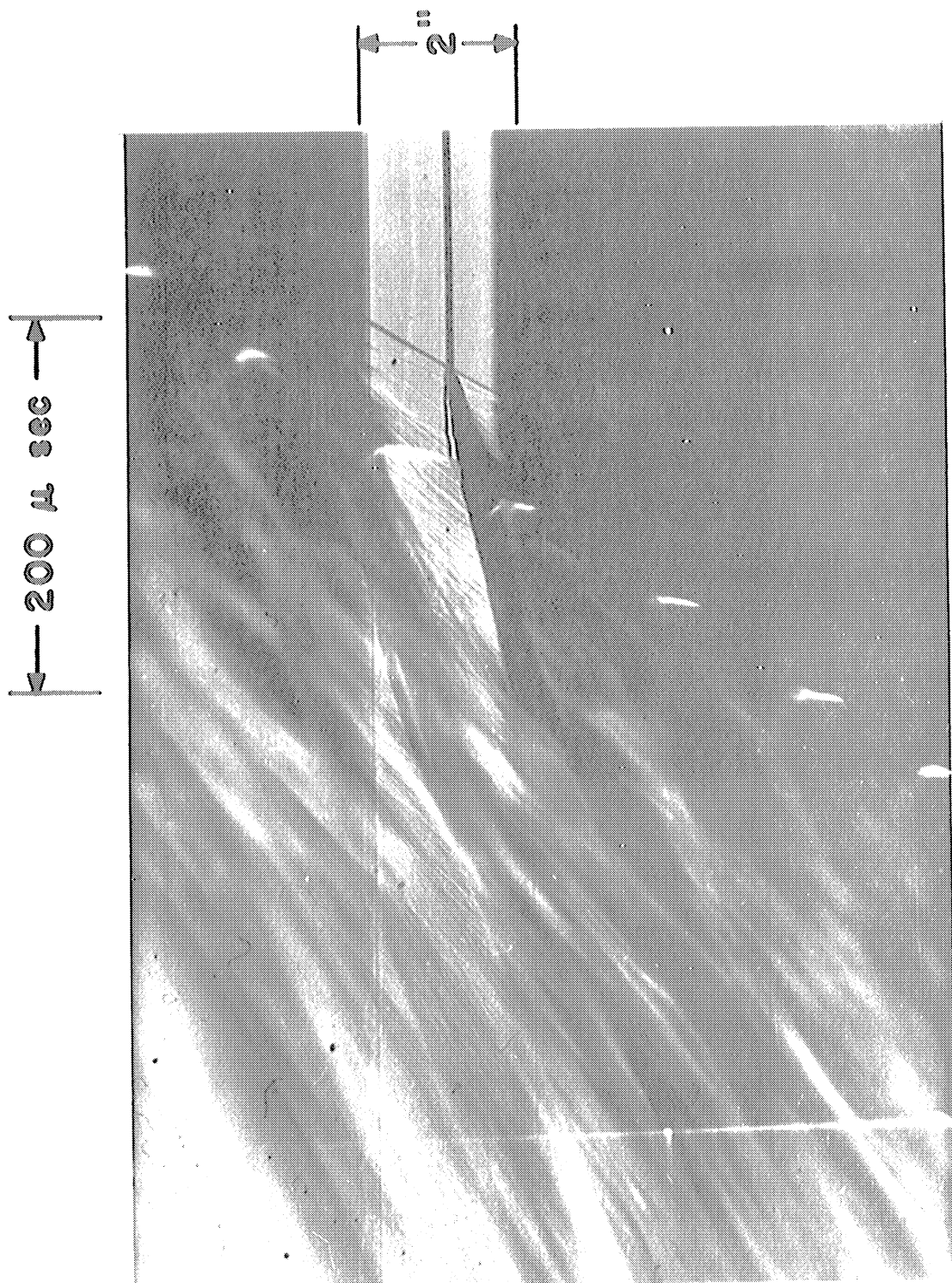
Fig. 2.4. Combined shadow and direct luminosity streak photograph of the detonation over a single stream of 2600μ drops (run no. 278).
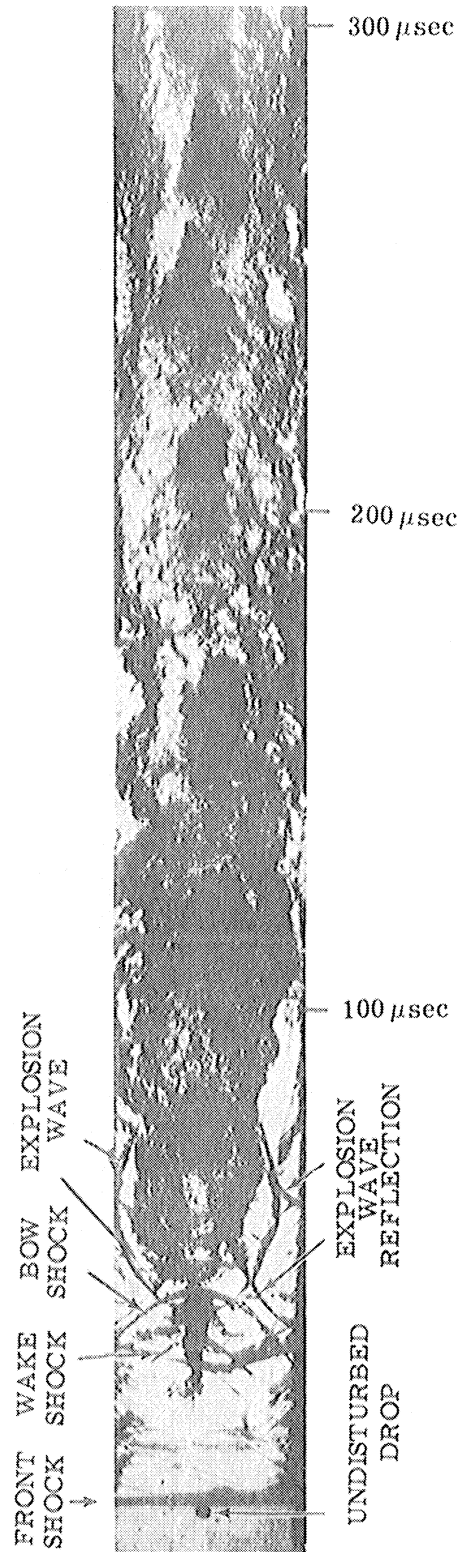
Fig. 2.5. Spark source (.2 μsec exposure) photograph of the detonation of single stream of 2600μ drops showing details of the phenomenon (run no. 452, 435, 436).

8

can see the deformation of the drop, the wake, the bow shock and the spherical explosion wave around the second drop behind the front. One can also see wake shocks behind the first drop. It is apparent that the identity of the drop can still be recognized for at least 300 μsec behind the wave. From the streak photographs it was estimated that the drop is consumed in about 500-600 μsec for this case in which the equivalence ratio is 0.23 and the velocity is about 3500 ft/sec.

Pressure measurements confirmed the existence of the spherical explosion in that spikes of double-to-triple the pressure behind the front were observed. Figure 2.6 shows a spark photograph of the detonation phenomenon and the corresponding pressure record obtained by a lead metaniobate pressure transducer[5] (the raster trace on top of the pressure trace is for velocity measurement and should be ignored). Due to the inertia of the drop, the drop moves a very short distance during the time covered by both the spark photograph and the pressure record. Thus the pressure record gives a rough indication of the pressure field behind the detonation front. The first pressure jump is fairly constant and is compatible with the expected shock pressure. At about 24 and 40 μsec, pressure peaks are attained due, probably, to the wake shock and the bow shocks respectively. At 64 μsec the high pressure peak-over twice the original pressure increase—must be due to the explosion wave seen around the second drop behind the wave front. Continued pressure fluctuations are most likely due to non-uniform combustion. The fluctuations in the pressure trace for the first 20 μsec can be attributed to weakened waves resulting from the explosion waves of drops already passed by the front. Such waves can be easily discerned in the photograph shown in Fig. 2.7.

The above described picture of the reaction zone behind the front becomes more complicated when the drops are closer together than shown in Fig. 2.5-2.7, as interactions between the flow fields around the drops and

100 μSEC

80

60

40

20

←STA. TSB→

80psi

20 μSEC/DIV.
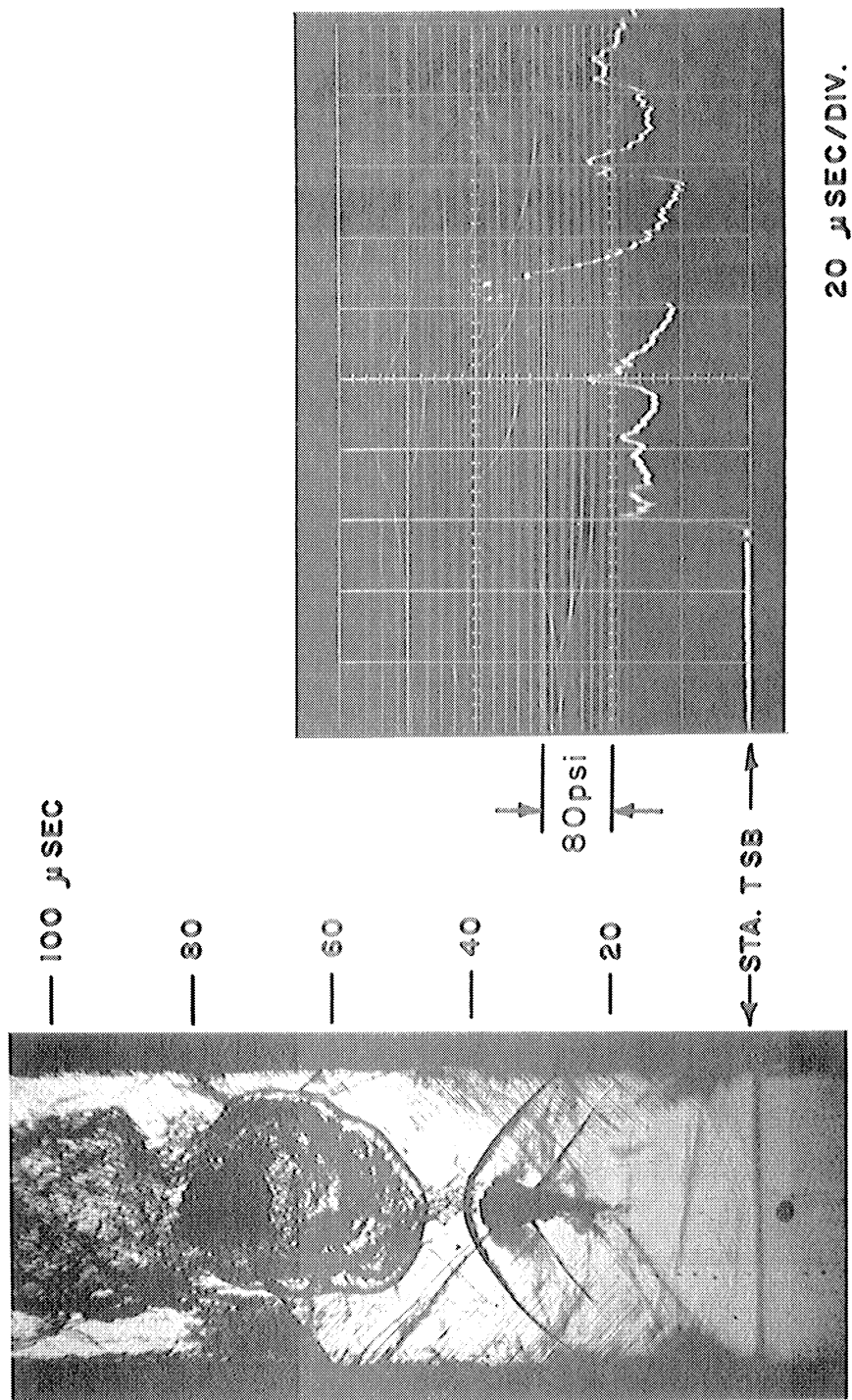
Fig. 2.6. Spark source photograph of single stream 2600μ drop detonation and corresponding pressure at the wall.
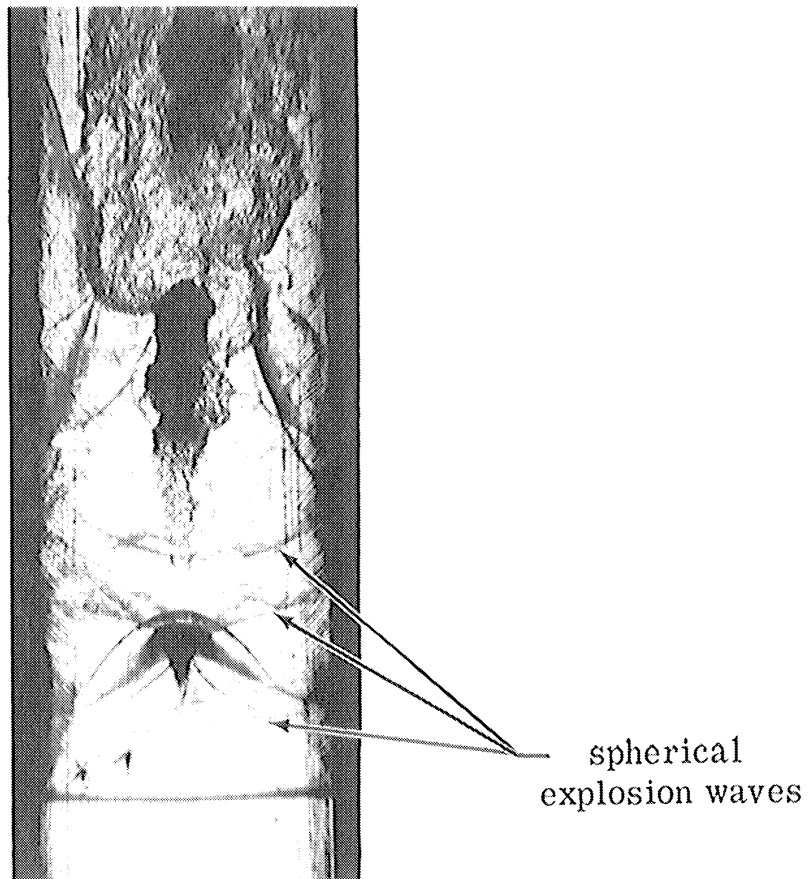
Fig. 2.7. Spark source photograph of single stream 2600μ drop detonation showing successive spherical explosion waves.

the accompanying shocks become more frequent. This can be seen in Fig. 2.8 which shows the zone behind the front of detonations travelling at 5200 ft/sec for both 2600μ and 940μ sprays.

2. Effect of Drop Size on Detonation Development Distance

Measurement of the detonation velocity throughout the length of the tube can give an indication of the distance (or time) needed before the detonation reaches a steady or nearly steady velocity. Figure 2.9 shows the velocity variation with distance from the initiation point for three different drop size sprays with equal equivalence ratio of 0.25 at distances beyond 4 ft from the fuel injection point. It can be seen that the development time is shorter the smaller the drop size. It should be pointed out that this effect would have been more pronounced were it possible to have a constant mixture ratio throughout the tube. As it was, because of the nature of the spray generator[4], the mixture ratio in the first 4 ft is leaner for the 290μ spray and richer for the 940μ and the 2600μ drops. This non-uniform mixture distribution would tend to either delay the detonation development in the 290μ spray or speed it up in the 940μ and the 2600μ sprays.

The effect of drop size on the development time at other mixture ratios can be seen from Fig. 2.10 and 2.11. In Fig. 2.10 the development time for the 290μ spray at an equivalence ratio of $\cong 0.6$ can be seen to be much shorter than that of the same drop size spray of Fig. 2.9 where the equivalence ratio is lower. It can also be seen, by comparison with Fig. 2.11, that the development time is shorter than that of the larger drop size spray even though the equivalence ratio in the latter case is close to stoichiometric.

3. Effect of Fuel Volatility on Spray Detonations

Almost all of the spray detonation experiments were performed with DECH as fuel. The vapor pressure of DECH at room temperature is 1.45 mm Hg so that assuming oxygen at atmospheric conditions to be saturated by the vapor, it results in an equivalence ratio of 0.02 and, therefore, the
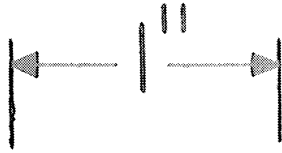
Fig. 2.8. Spark source photograph of the detonation of
(a) 4 streams of 2600μ drops (run no. 465)
and (b) 940μ spray (run no. 445).
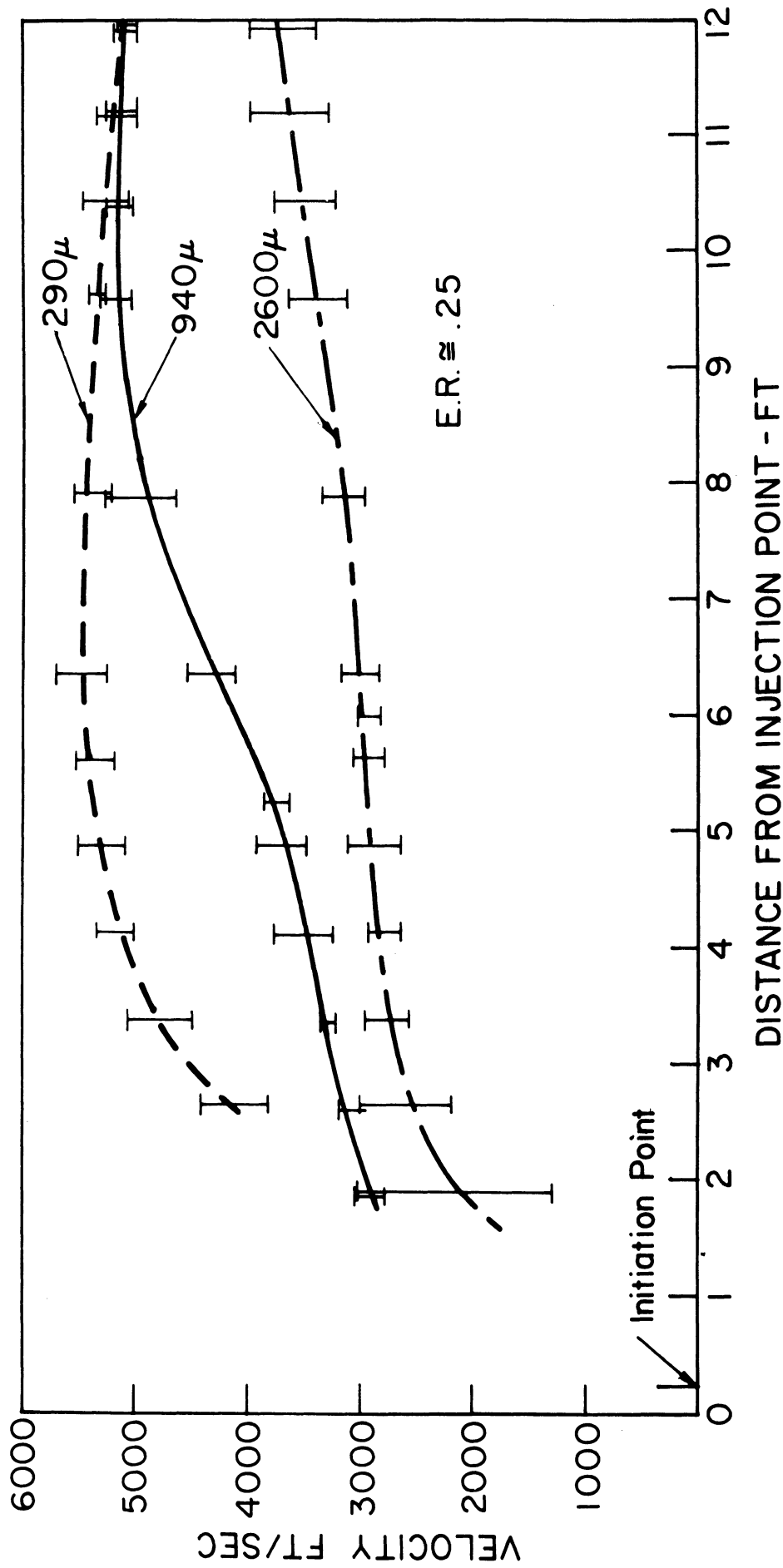
Fig. 2.9. Propagation velocity vs. distance from injection point for
equivalence ratio ≅ 0.25.

14
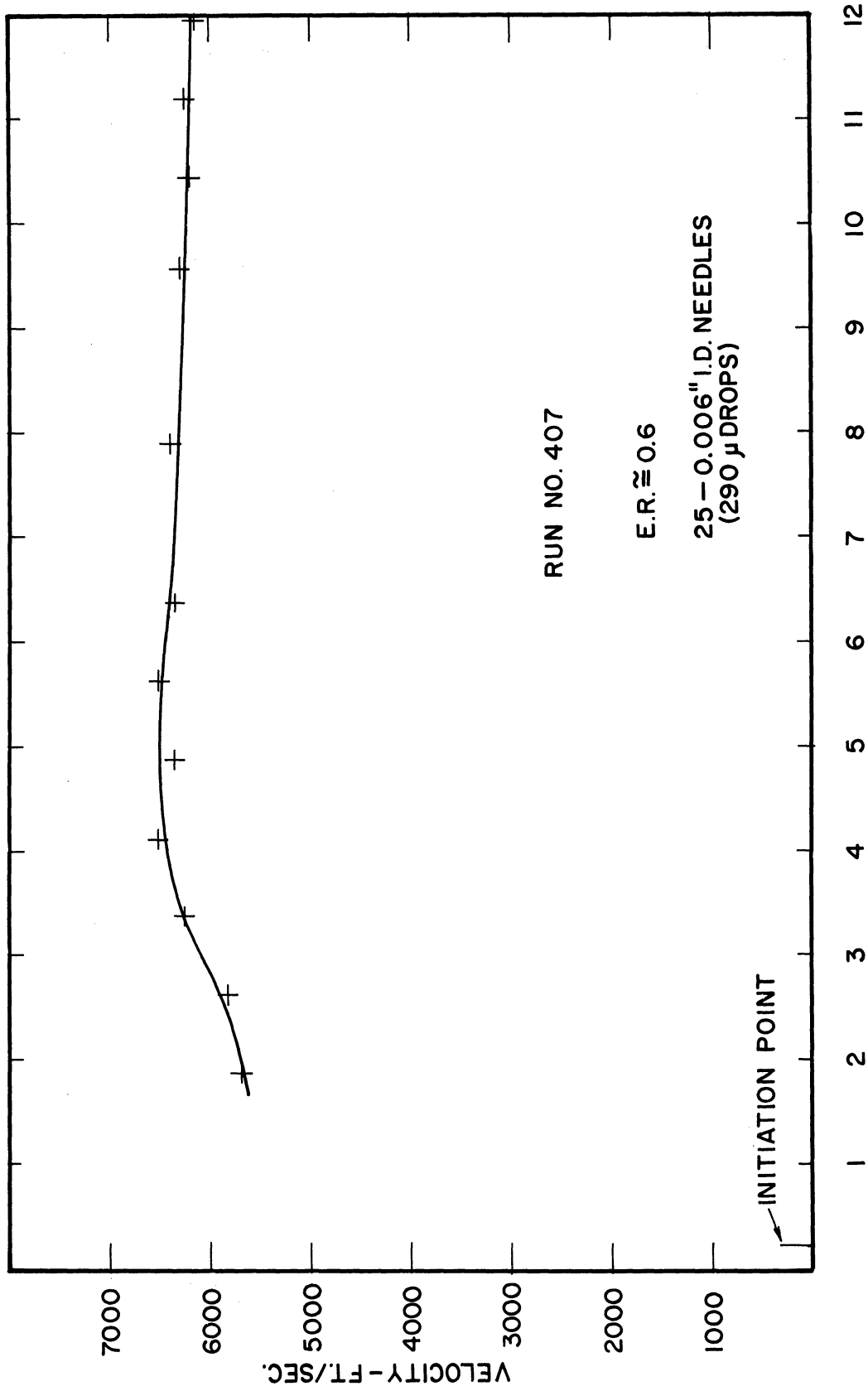
Fig. 2.10. Propagation velocity vs. distance from injection point for equivalence ratio ≅ 0.6.
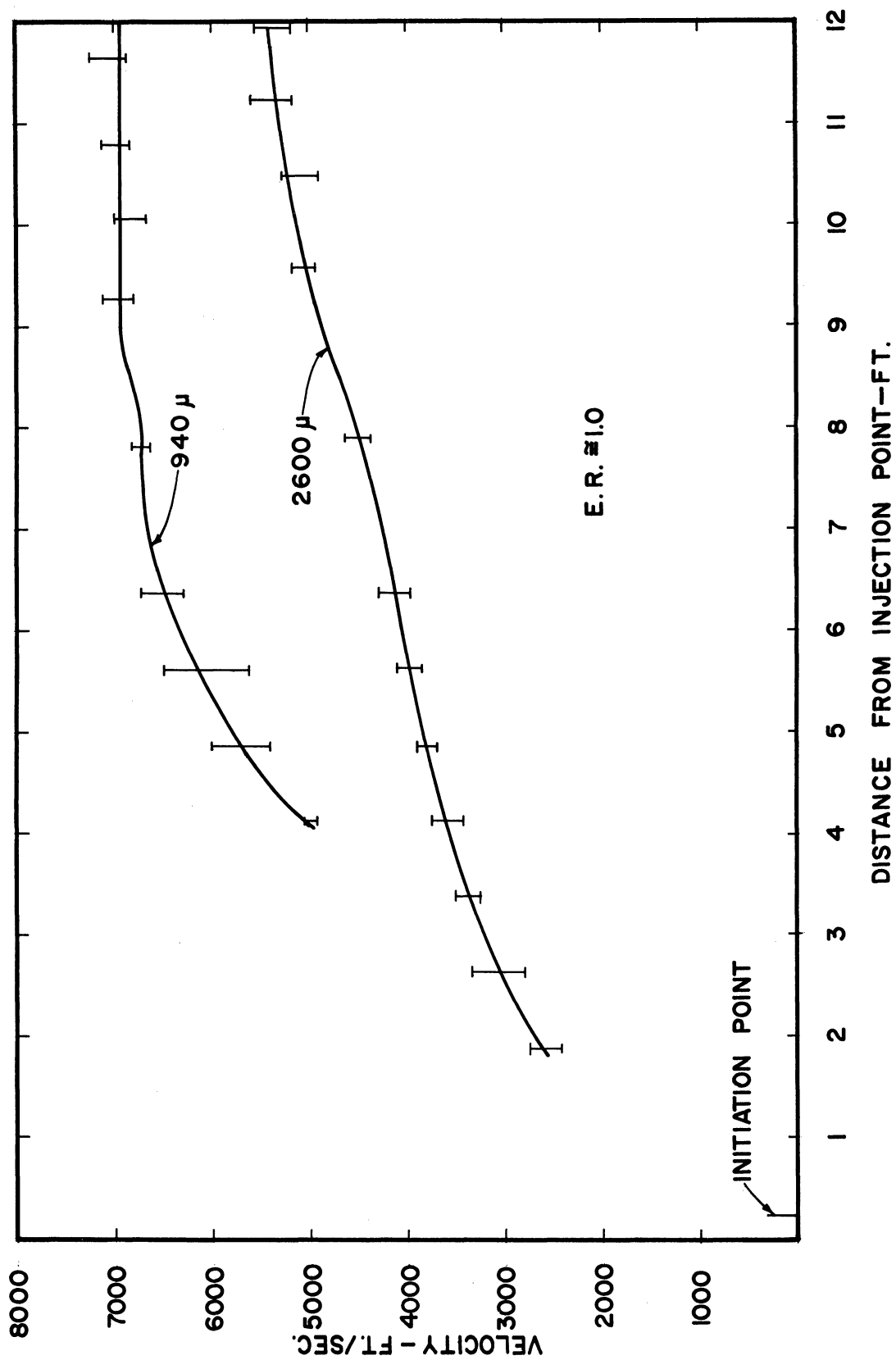
Fig. 2.11. Propagation velocity vs. distance from injection point for equivalence ratio ≅ 1.0.

16

quantity of the fuel in the vapor phase is negligibly small compared to that of the liquid phase for even the leanest mixtures tested. To see whether fuels with higher volatility would have any effect on the detonation phenomenon two other fuels were considered for testing, namely, n-octane (vapor pressure = 11 mm Hg) and benzene (vapor pressure = 80 mm Hg). The saturated oxygen-fuel vapor mixtures would result in equivalence ratios of 0.18 and 0.957 respectively. However, it is not expected that the oxygen in the tube would be saturated as the spray fuel is introduced only 2-4 sec before initiation.

The Chapman-Jouguet (CJ) detonation parameters for these two fuels with oxygen were calculated by the methods outlined in Ref. 3 and 7 which makes use of the computer program of Ref. 8. The results of the calculation are plotted in Fig. 2.12 and 2.13; they are similar to those of DECH-O_2 mixtures[3,7]. These results are of course for ideal situations where no frictional or heat transfer losses in the reaction zone are considered. The losses are related to the extent of the reaction zone, which could be affected by the volatility of the fuel.

A few runs were made with 2600μ drops of benzene in oxygen. The detonation velocity variation with distance was very similar to DECH-O_2 detonations under the same conditions. Photographs of the reacton zone indicate similar structure also, as shown in Fig. 2.14a. Figure 2.14b shows a time exposure ($\simeq 150$ μsec) of the flame behind the shock. In this instance the top part of the flame would be about 150 μsec behind the shock. It is clear that the flame is centered in the tube. The lack of combustion near the wall indicates that neither the residence time of the drops in the tube prior to the passage of the detonation front, nor the time after the passage of the front (when diffusion is expected to be enhanced by the increased surface area due to drop stripping) were sufficient for appreciable diffusion or mixing of the fuel with oxygen. From the velocity data and photographs
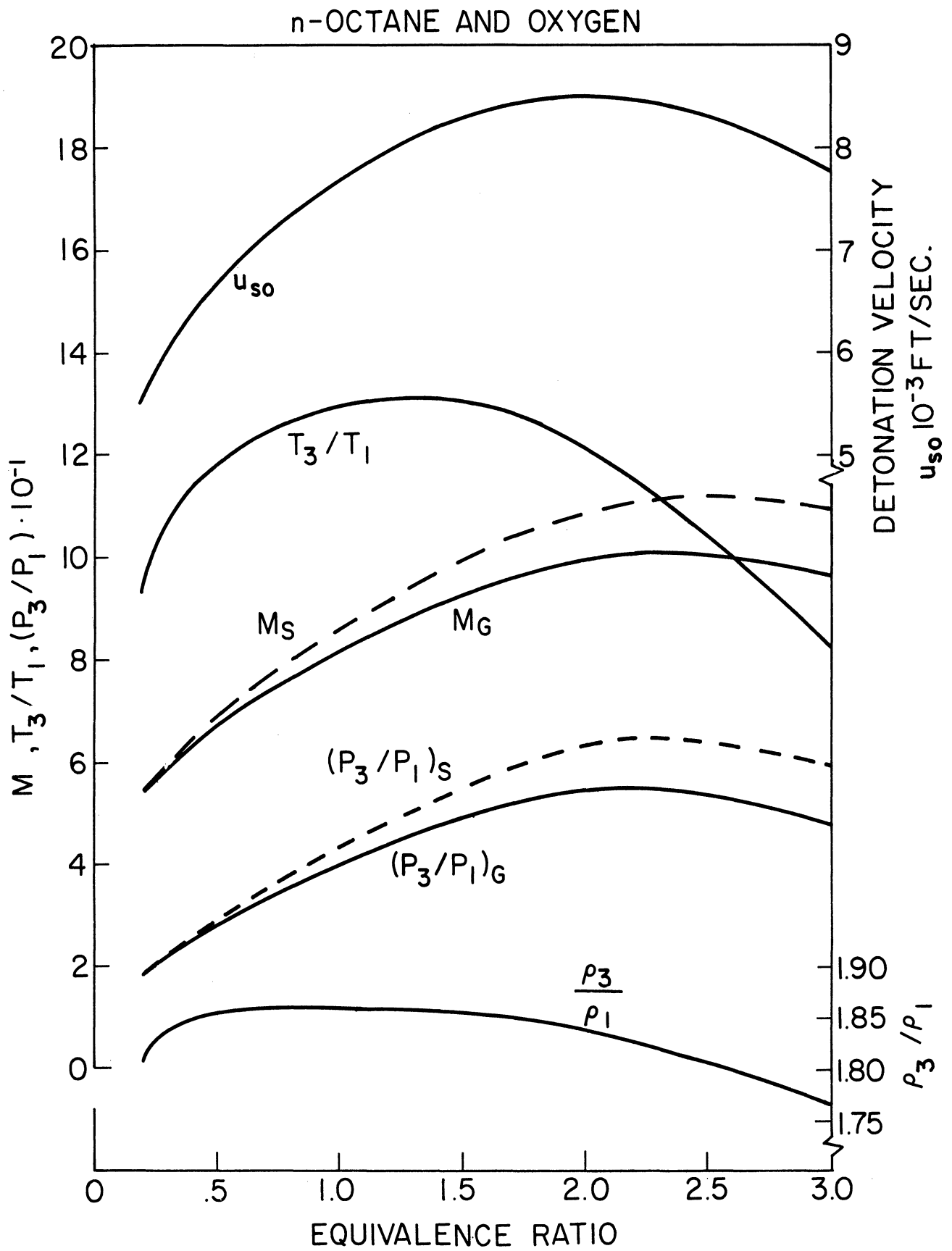
Fig. 2.12. Properties of n-octane-O_2 detonations.
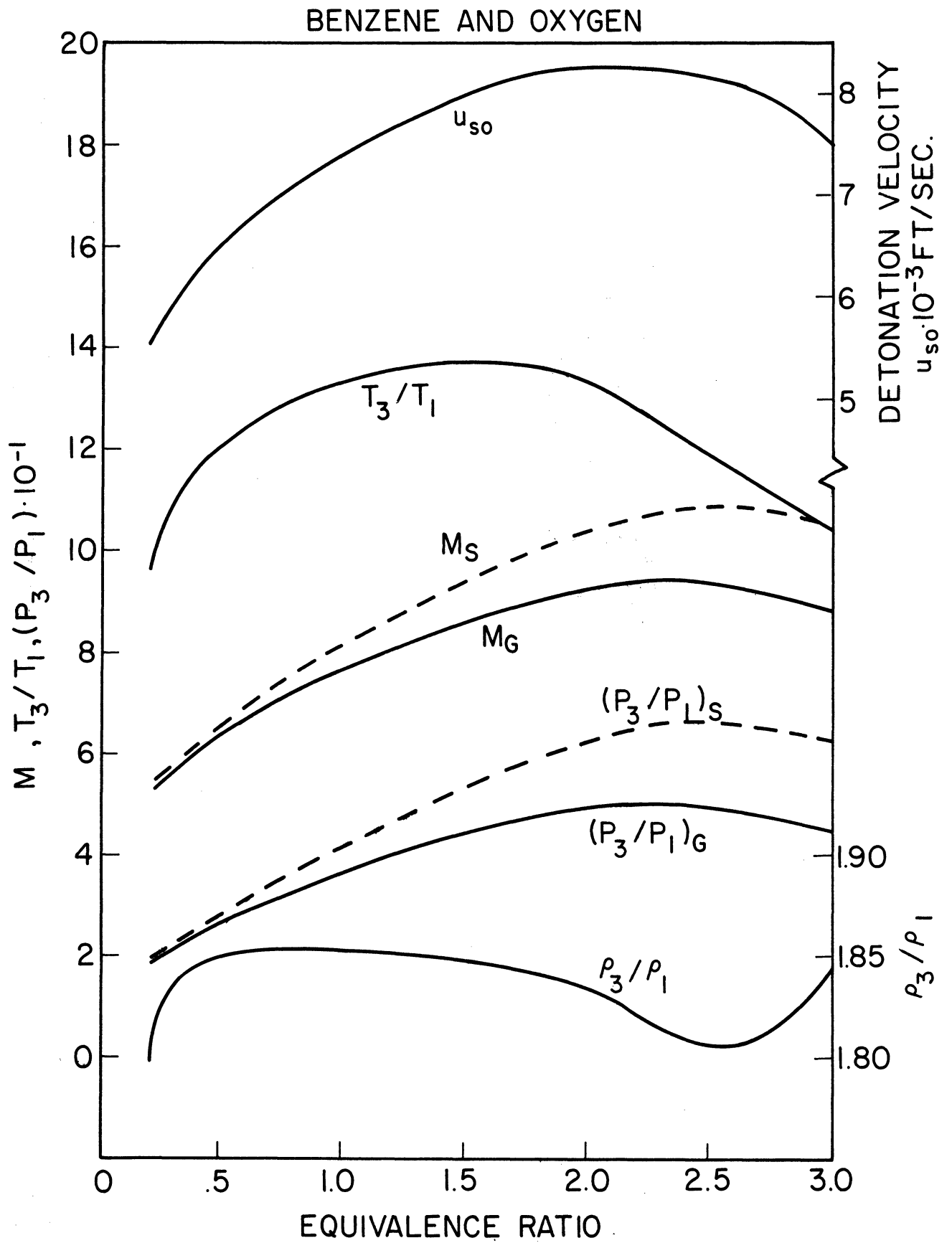
Fig. 2.13. Properties of benzene-O_2 detonations.
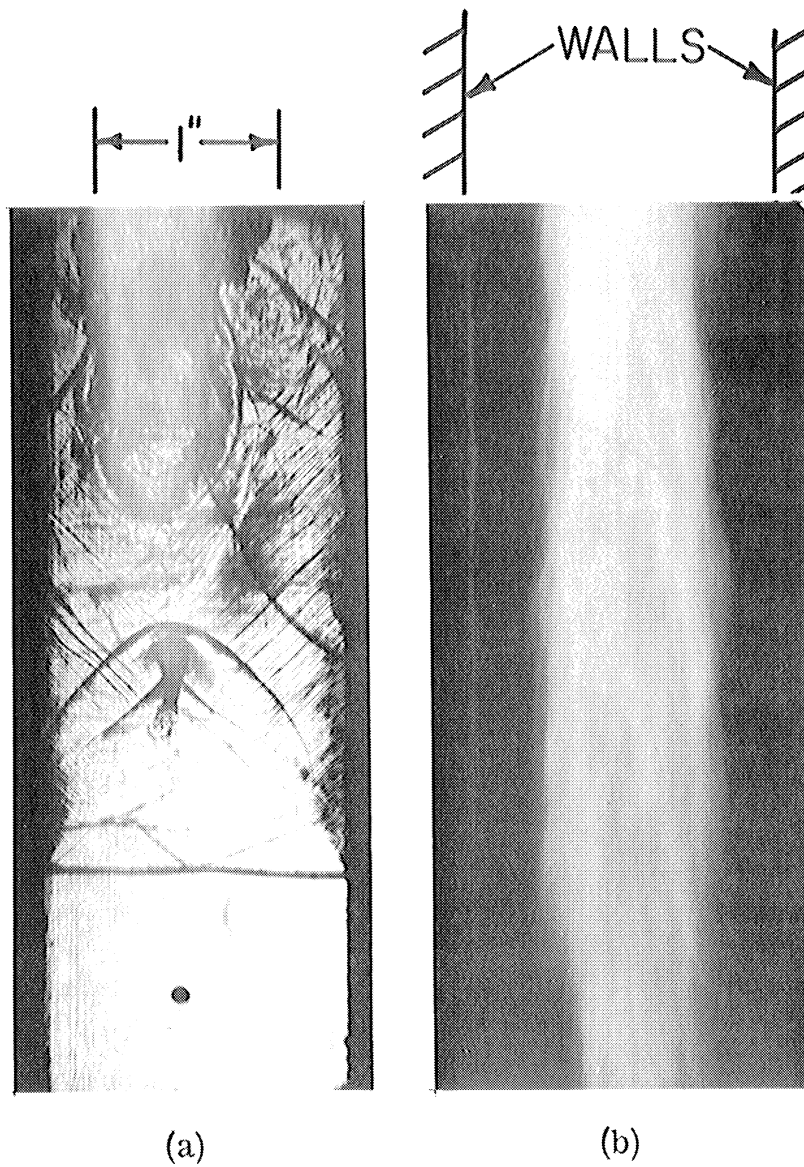
Fig. 2.14. Photographs of benzene-O_2 detonation, 2600μ drops, single stream.
(a) spark source; (b) self luminous radiation only.

of the zone behind the wave it is tentatively concluded that no basic difference exists between fuels with high volatility and low volatility as far as the detonation phenomenon is concerned.

4. Effect of Drop Size on Velocity Difference

Measurement of the steady velocity was made for mixtures at equivalence ratios ranging from 0.2 to 1.0. The data for the three drop sizes is shown in Fig. 2.15 and is compared with the calculated theoretical CJ velocity[2]. It can be seen that the velocity difference is about 2-10% for the 290μ and the 940μ sprays but about 30-35% for the 2600μ. This difference will be shown to be due to heat transfer and friction losses to the tube walls in the reaction region.

The reaction region here is assumed to be the region between the front of the wave and the CJ plane. In this region the flow is complicated by drop deformation and breakup, interactions of the two phases, and the chemical reaction due to combustion. However, it is reasonable to assume a one-dimensional flow near the front, which appears to be reasonably planar, as well as after all interactions have subsided. Such an assumption was made before[3,9] so that the one-dimensional conservation equations where frictional and heat losses were taken into consideration resulted in an equation that can be reduced to the following form:

$$\frac{u_s}{u_{so}} = \left\{ 1 + \left[C_D + 2 \left(\gamma_3^2 - 1 \right) C_H \right] \frac{\bar{x}}{(1 + \phi) \, r_h} \frac{u_2^2}{u_s (u_s - u_2)} \right\}^{-1/2} \tag{2.1}$$

The drag and heat transfer coefficients are defined[9] as

$$C_D \equiv \int_2^3 \tau_o \, dx \Big/ \frac{1}{2} \bar{x} \, \rho_2 \, u_2^2 \tag{2.2}$$
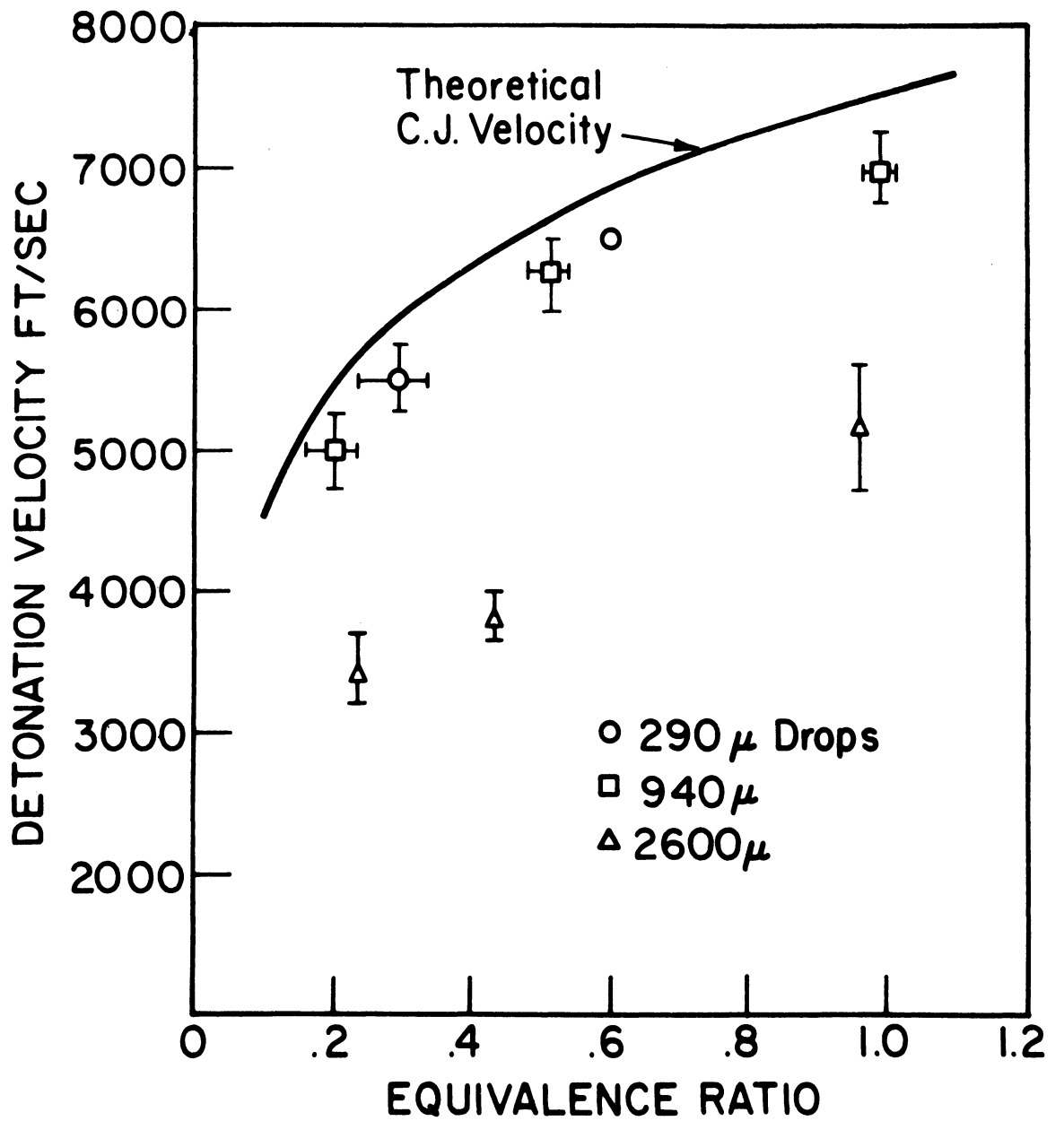
Fig. 2.15. Comparison of experimental detonation velocity
with the ideal C-J velocity.

and

$$C_H \equiv \int\limits_2^3 q\ dx \Bigg/ \rho_2\ u_2 \left(h_2 + \frac{u_2^{\,2}}{2} - h_w \right) \tag{2.3}$$

The heat transfer rate, q, was measured by a thin film gauge, a rugged version of which is described in Appendix I. Thus, an estimate of C_H and, if a Reynolds' analogy is assumed, of C_D can be obtained. Estimation of the reaction length, $\bar{x}$, can be made by assuming that it is controlled by the breakup time as will be evidenced later. From work done at this laboratory and elsewhere[10,11] on the breakup of inert drops by shock waves, the breakup time, t_b, can be related to the dynamic pressure of the convective flow and the drop diameter D, as follows:

$$t_b \Big/ D = k\ \rho_\ell^{\,1/2} \left(\frac{1}{2}\ \rho_2\ u_2^{\,2} \right)^{-1/2} \tag{2.4}$$

where k is a constant $\simeq$ 5 and ρ_ℓ is the liquid density (a similar relation was obtained by Clark[12] on the breakup of liquid jets). Some recent experimental results by Jaarsma and Derksen[13] on the breakup of burning and non-burning drops confirm the above relationship. However, they found k to be about 4.5.

Streak photographs of the spray detonation indicated that the time for the breakup of the drop was about double the time calculated by this equation. It is reasoned that since the drop in a detonation is subjected to a varying dynamic pressure, due to the continuously changing conditions behind the front, a better estimate of the actual breakup time in a detonation would be obtained if an average dynamic pressure is used.

23

The dynamic pressure behind a shock can be shown to be

$$q_s = \frac{1}{2} \rho_1 u_s^2 \left(\frac{\rho_2}{\rho_1}\right)\left(1 - \frac{\rho_1}{\rho_2}\right)^2 \tag{2.5}$$

Similarly behind a detonation, the dynamic pressure is

$$q_D = \frac{1}{2} \rho_1 u_s^2 \left(\frac{\rho_3}{\rho_1}\right)\left(1 - \frac{\rho_1}{\rho_3}\right)^2 \tag{2.6}$$

Comparing the products of the last two terms in Eq. (2.5) and (2.6), and assuming a constant $\gamma = 1.4$, one can show, since

$$\frac{\rho_2}{\rho_1} = \frac{(\gamma + 1) M^2}{M^2 (\gamma - 1) + 2} \tag{2.7}$$

and

$$\frac{\rho_3}{\rho_1} = \frac{(\gamma + 1) M^2}{\gamma M^2 + 1} \tag{2.8}$$

that $q_D/q_s < 10\%$ for $M > 3$. Thus, an average dynamic pressure equal to half of that in Eq. (2.4) can be used. Equation (2.4), then, can be modified to read:

$$t_b/D = 2k \left(\frac{\rho_\ell}{\rho_1}\right)^{1/2} \left(\frac{\rho_1}{\rho_2}\right)^{1/2} \left(\frac{1}{u_2}\right) \tag{2.9}$$

or in terms of the shock velocity:

$$\tau_b \equiv t_b u_s/D = 10 \left(\frac{\rho_\ell}{\rho_1}\right)^{1/2} \left(\frac{\rho_1}{\rho_2}\right)^{1/2} \left(1 - \frac{\rho_1}{\rho_2}\right)^{-1} \tag{2.10}$$

24

This equation gives a value of τ_b = 162 for M = 3 which decreases to 120 for M → ∞.

With $\bar{x}$ assumed equal to $t_b u_s$ and with $C_D = 2C_H$, Eq. (2.1) can now be written as

$$\frac{u_s}{u_{so}} = \left[1 + \frac{20D}{(1 + \phi)\, r_h}\, \gamma_3^2\, C_H \left(\frac{\rho_\ell}{\rho_1}\right)^{1/2} \left(\frac{\rho_2}{\rho_1}\right)^{1/2} \left(1 - \frac{\rho_1}{\rho_2}\right)\right]^{-1/2} \qquad (2.11)$$

Examples of heat transfer coefficient data are shown in Fig. 2.16 and 2.18 for detonation in 2600μ sprays. In Fig. 2.16, the data correspond to M = 3.3. Two different gauges stationed 1 ft apart were used. The response of the guages can be very similar as can be seen in Fig. 2.17. Heat transfer data corresponding to M ≅ 5 are shown in Fig. 2.18. Examination of Fig. 2.16 and 2.18 show that C_H rises sharply at $\tau_m \cong t u_s / D \cong 200$ when M ≅ 3.3 and at $\tau_m \cong 100$ when M ≅ 5. Thus, it appears that the point where C_H reaches a maximum follows the same trend as the nondimensional breakup time. Comparing τ_b and τ_m one finds the difference is not in the same direction for M near 3 as for M near 5. An important difference may be that in the case of M ≅ 5 the drops are initially subjected to pressures higher than the critical pressure of DECH (25 atm). This is not true for M ≅ 3. Further investigation is needed to ascertain whether the possible difference is indeed important. For the present we assume that the maximum C_H signals the end of the reaction zone and therefore conclude that the reaction length is controlled by the breakup time.

It should be noted that the product of the last two density ratio terms in Eq. (2.11) should correspond to u_s. However this product would not differ by much if values corresponding to u_{so} were used. Furthermore, for mixtures leaner than twice stoichiometric, an increase in ϕ corresponds to an increase in u_{so} and therefore in the product of the density terms. Thus Eq. (2.11) can be approximated by
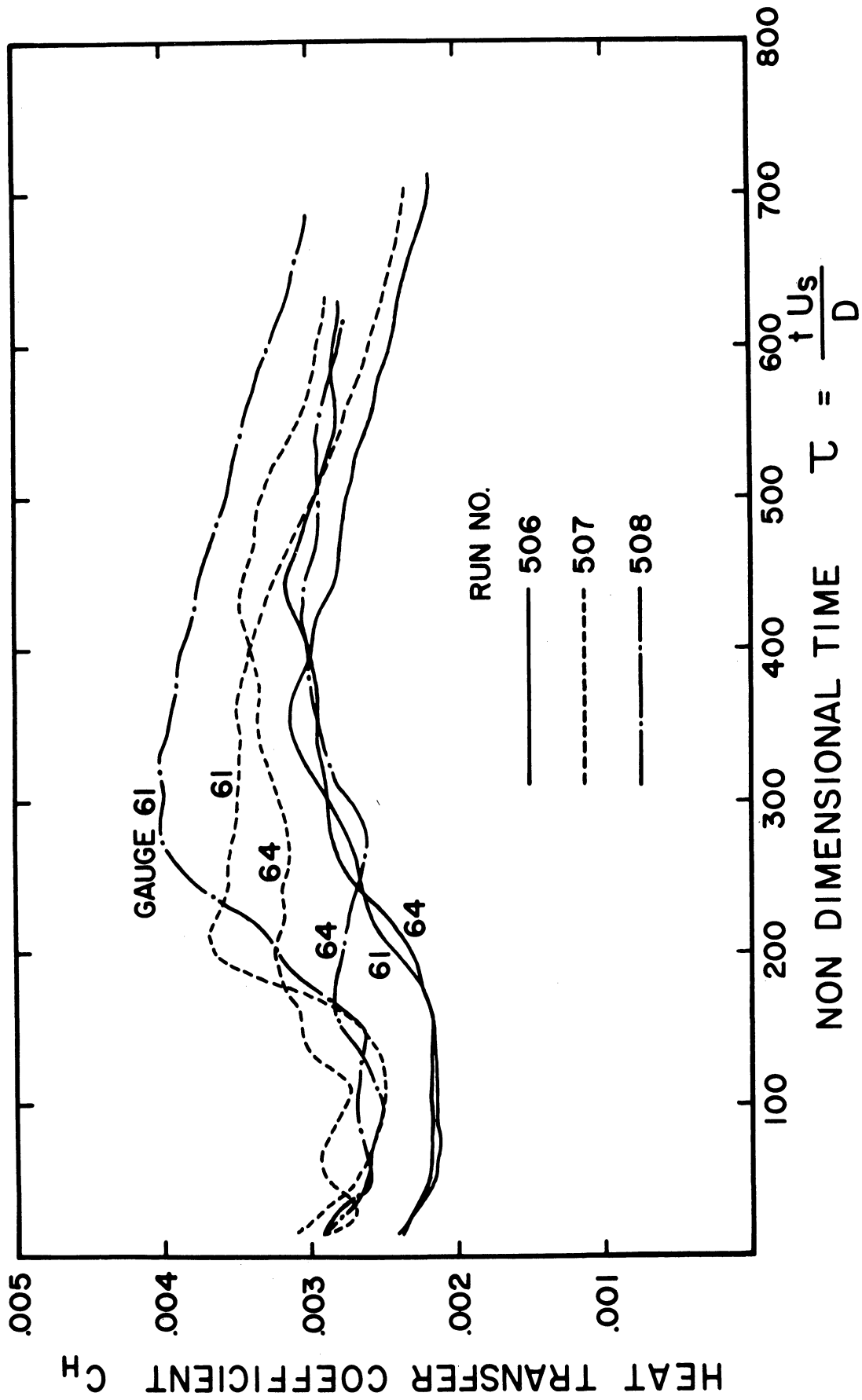
Fig. 2.16. Heat transfer coefficient vs. non-dimensional time for $M \cong 3.3$.
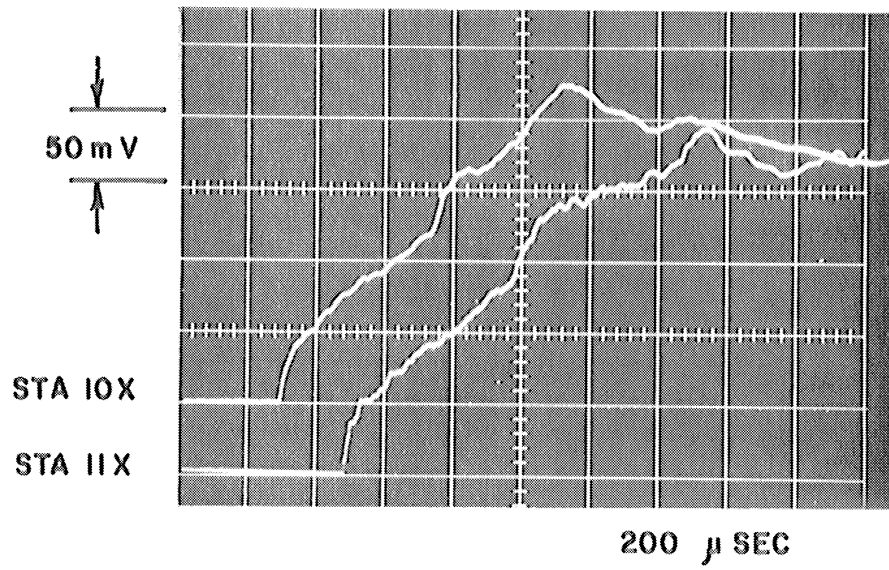
Fig. 2.17. Response of heat transfer gauge to single stream 2600μ drop detonation, M ≅ 3.3 (run no. 506).
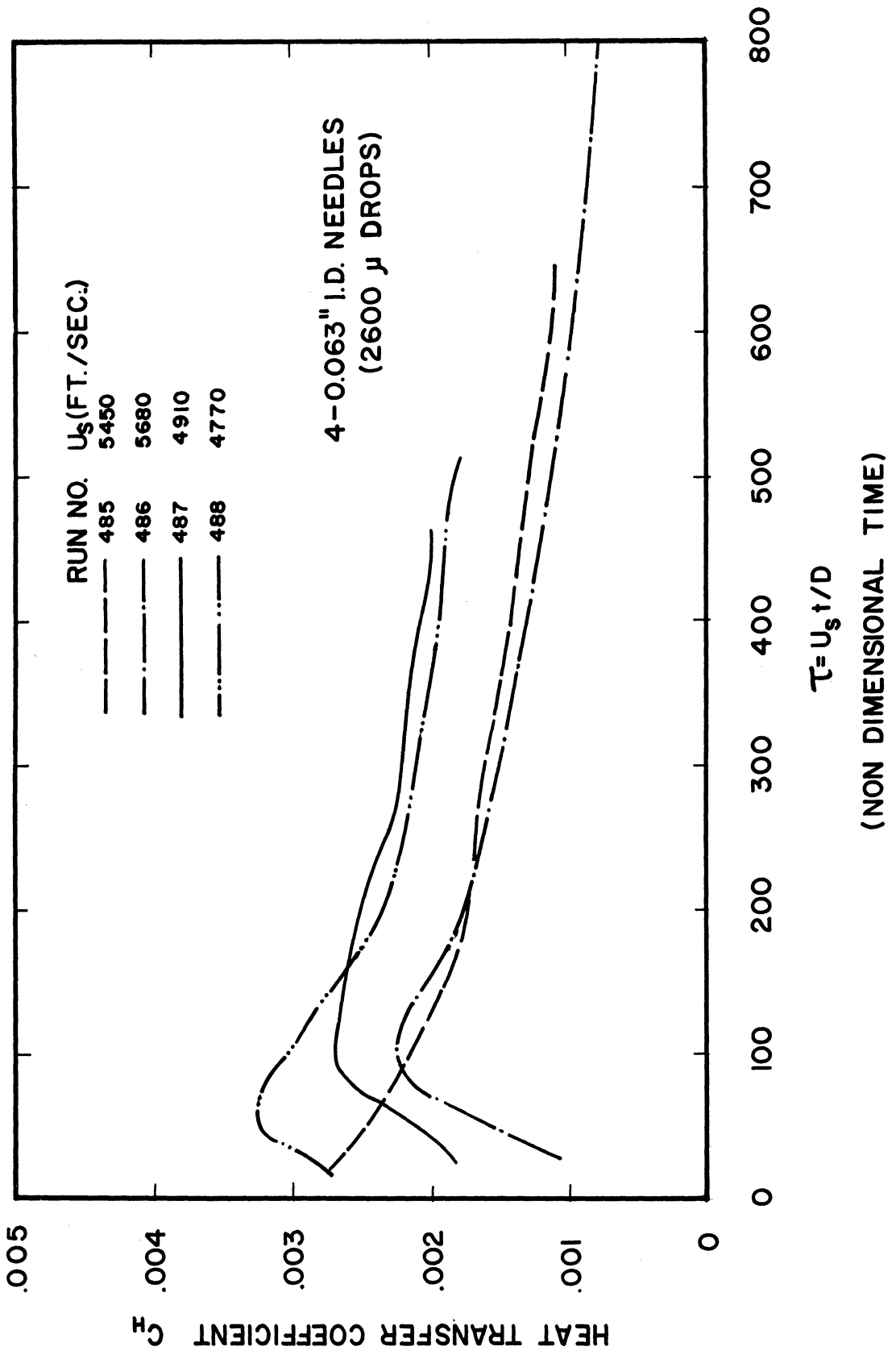
Fig. 2.18. Heat transfer coefficient vs. non-dimensional time for $M \cong 5$.

$$\frac{u_s}{u_{so}} = \left[1 + \frac{30D}{r_h} \gamma_3^2 \left(\frac{\rho_\ell}{\rho_1} \right)^{1/2} C_H \right]^{-1/2} \tag{2.12}$$

Using a value of $C_H = 2.5 \times 10^{-3}$ (which is our best up-to-date estimate) and $\gamma_3 = 1.2$, we obtain for our tube ($r_h = 1.04$ cm) for D = 2600μ, 940μ and 290μ, u_s/u_{so} = 0.76, 0.90 and 0.96 respectively. These values are in reasonable agreement with the experimental results shown in Fig. 2.15. Thus although the structure of the spray detonation is very complicated, it appears that the one-dimensional theory with frictional and heat transfer losses in a reaction zone controlled by the breakup time can offer useful predictions of the detonation velocity.

III. LIQUID FILM DETONATIONS

1. Test Setup and Procedure

The test setup for the film detonations is similar to that of the spray detonations. However, since it was found that the shock tube initiator was insufficient to start the film detonations, a vertical 2 in. i. d. driver was used. This tube consisted of seamless 304 stainless steel with 1/4 in. walls. The performance of the driver is discussed later.

The layer of fuel was applied to the wall by running a very fine sponge, which was soaked with fuel, down the tube. The sponge was fastened to a holder so that either one wall or two opposing walls could be coated. The sponge and sponge holder were weighed before and after application of the fuel, and thickness of the fuel layer was calculated from the weight by assuming a uniform distribution of fuel. The relationship between the weight of fuel applied and the thickness of the fuel layer is plotted in Fig. 3.1 for the tube used. The equivalence ratio is also plotted as a function of the fuel weight. A stoichiometric mixture ratio is attained with about 2.5 g of fuel on the walls, and when two walls are coated this results in a fuel layer 10μ thick. When only one wall is coated, a stoichiometric mixture is achieved with a 20μ thick fuel layer assuming one atm O_2 present. The film detonation experiments were run near the above conditions. It should be mentioned that the DECH runs down the wall very slowly because the layer is so thin. The velocity and mass flow of a falling liquid film are calculated on the basis of the theoretical work of Nusselt (1960) which was verified experimentally by Portalski[14]. The mean velocity of the liquid layer is

$$u_{mean} = \frac{1}{\lambda} \int_0^\lambda u \, dy = \frac{\rho g \lambda^2}{3\mu} \qquad (3.1)$$
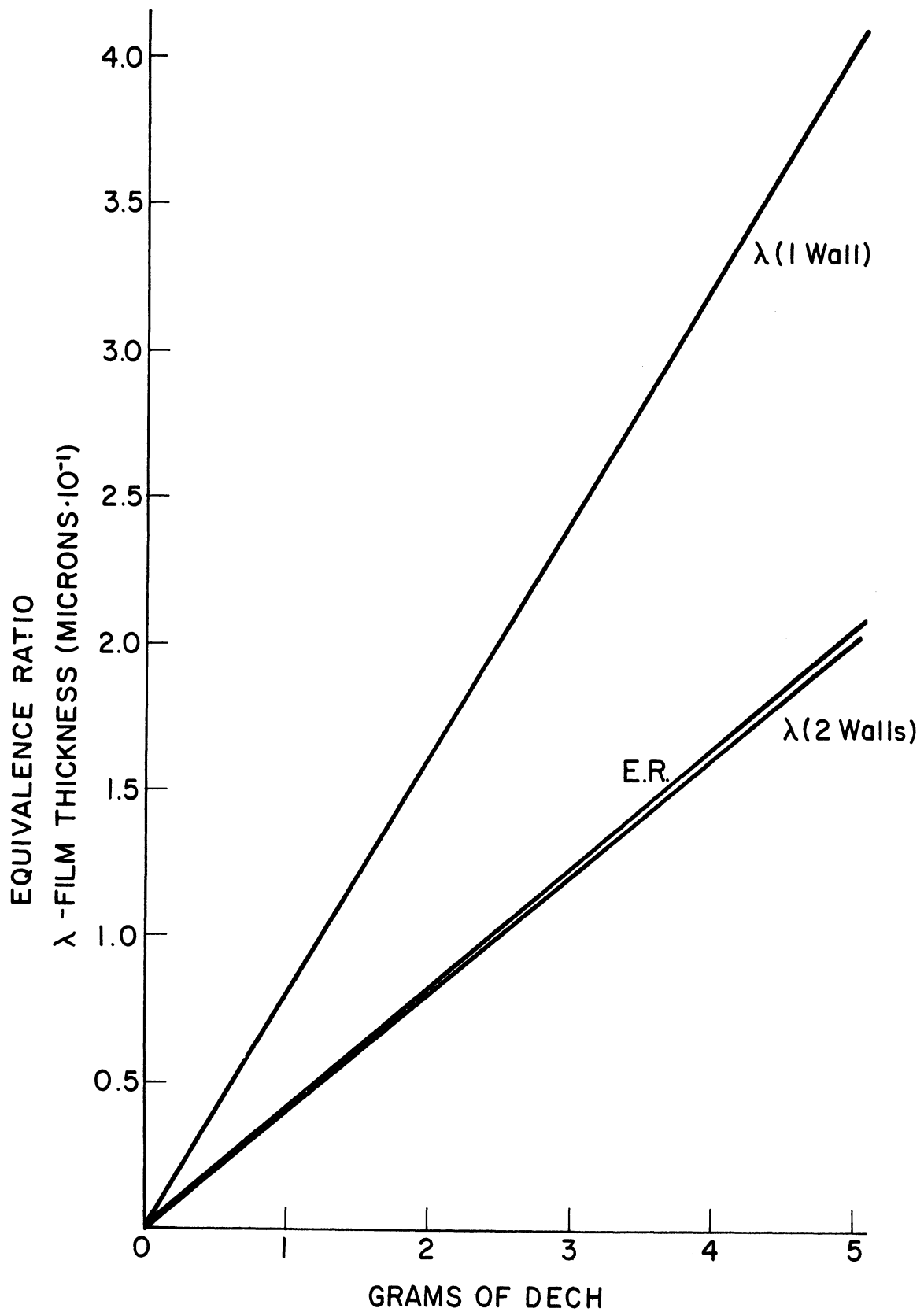
Fig. 3.1. Effective equivalence ratio and film
thickness for a given weight of fuel.

and the velocity of the outer layer of fluid is,

$$u = \frac{\rho g \lambda^2}{2\mu} = 3/2 \, u_{mean} \qquad (3.2)$$

The mass flow rate per unit width of the plate is,

$$Q = \rho \lambda \, u_{mean} = \frac{\rho^2 g \lambda^3}{3\mu} \qquad (3.3)$$

Using $\rho = 0.802$ g/cc and $\mu/\rho = 1.35$ cS, which are representative of DECH, Eq. (3.2) and (3.3) become,

$$u_\lambda = 3.63 \times 10^4 \, \lambda^2 \qquad \text{(cm/sec)} \qquad (3.4)$$

$$Q = 1.94 \times 10^4 \, \lambda^3 \qquad \text{(g/cm sec)} \qquad (3.5)$$

Equations (3.4) and (3.5) are plotted in Fig. 3.2 for values of λ from 5μ to 40μ.

For a 10μ thick film the velocity of the outer edge of the liquid is 0.036 cm/sec, while for a 20μ film the velocity is 0.145 cm/sec. Generally the tests were run not longer than 5 minutes after applying the film. In that time a $10\,\mu$ film on two walls of the tube would lose about 0.048 g out of 2.5 g while a 20μ film would lose 0.19 g out of 2.5 g. This was considered as an acceptable deviation, but it is apparent that it is not feasible to use films of DECH much thicker than 20μ with this technique.

The procedure for running a film detonation was as follows: remove the driver section, position the wetted sponge at the top of the combustion tube, cover the flange with a .001 in. Mylar diaphragm and attach driver section, purge with oxygen through the open end of the combustion tube, shut off the oxygen and draw the wetted sponge rapidly down the tube, seal the bottom of the combustion tube with a .001 Mylar diaphragm, load the driver, and fire the spark plug to detonate the driver. An oxygen purge was used, rather than
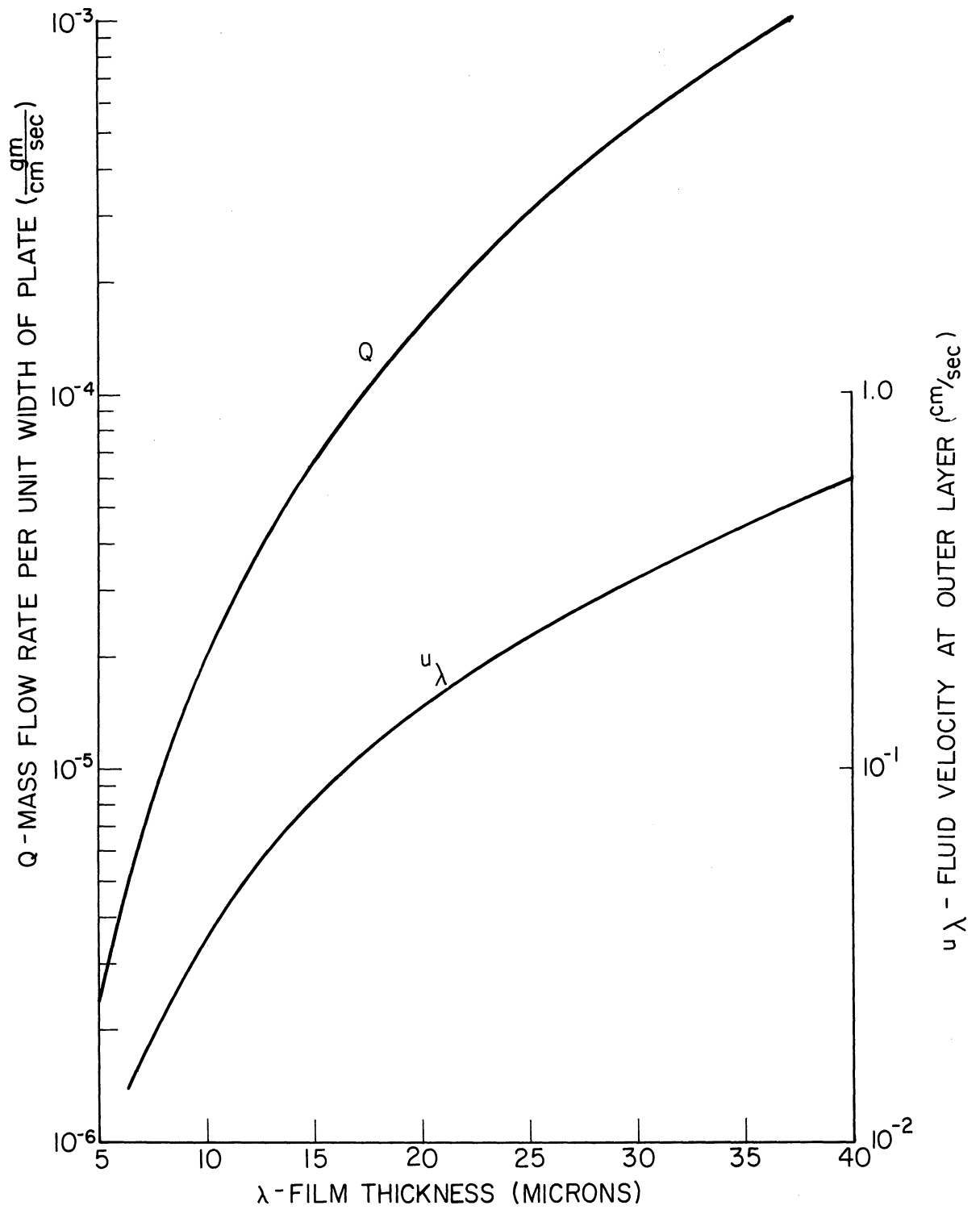
Fig. 3.2. Maximum velocity and mass flow of a falling liquid
layer vs. thickness of the layer.

evacuating the combustion tube after the fuel had been applied, because it was found that evacuation caused a fog to appear. This fog was due to two sources — water vapor in the air, and entrapped air in the DECH which caused very fine DECH droplets to be formed as the pressure was reduced.

2. Performance of the Driver

As was mentioned before, the initiator driver used for the droplet detonations was insufficient to trigger a film detonation. A 1/2 in. i. d. initiator driver mounted vertically above the center of the square combustion tube, with the diaphragm at the flange of the square section, was insufficient to consistently trigger a film detonation (when 60 in. Hg of $2H_2 + O_2$ was used in this driver, a film detonation could occasionally be generated). A 2 in. i. d. initiator driver was then used. When only one wall of the combustion tube was coated with fuel, the driver was filled with 20 in. Hg of $2H_2 + O_2$; when two walls were coated, 15 in. Hg of $2H_2 + O_2$ was used.

The use of detonation waves to create high pressure reservoir gases in the driver section of a shock tube has been considered for a number of years. The main advantage is that a shock wave can be generated with a very low initial driver pressure as compared to a conventional helium driver shock tube. Morrison[15] analyzed the collision of a detonation wave with a gaseous interface. As an example, he showed that a detonation wave passing through a stoichiometric mixture of hydrogen and oxygen at one atm transmits a Mach 4. 4 shock into a driven section containing air at one atm. Reported experimental studies concerning this type of shock tube driver are not known to be available, probably because this method has not proven to be useful when uniform conditions in the driven section are desired.

Pressure and heat transfer records of the shock which is transmitted by the 2 in. i. d. initiator are shown in Fig. 3. 3 for the detonation of 1 and 1/2 atm stoichiometric hydrogen-oxygen into one atm air. It is immediately
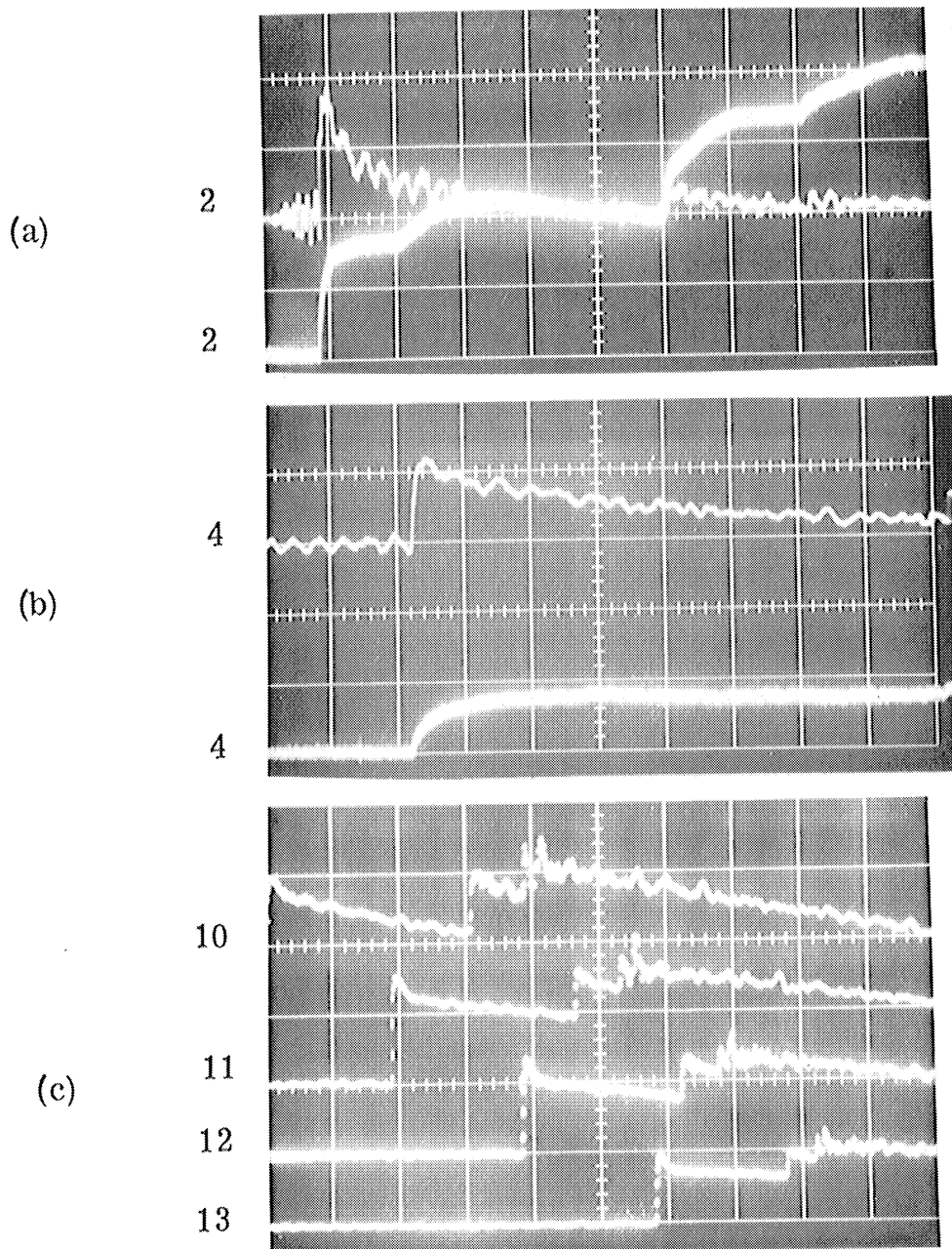
Fig. 3.3. Transmitted shock from the 2 in. i.d. initiator due to detonation of $(2H_2 + O_2)$ into 29.0 in. Hg air.
(a) 30 in. Hg of $(2H_2 + O_2)$. 200 μsec/div. Station 2: filtered Kistler model 603, 134 psi/div. Lower beam: heat transfer gauge No. 16, 15.2 ohm, 19.0 ma, 0.00714 V/div.
(b) Same as (a) but at station 4 and 100 μsec/div.
(c) 30 in. Hg of $(2H_2 + O_2)$. 200 μsec/div. Station 10x: Kistler 601A, 19.8 psi/div. Station 11x: Kistler 603, 26.8 psi/div. Station 12x: Kistler 603, 31.2 psi/div. Station 13x: Kistler 601A, 41 psi/div.
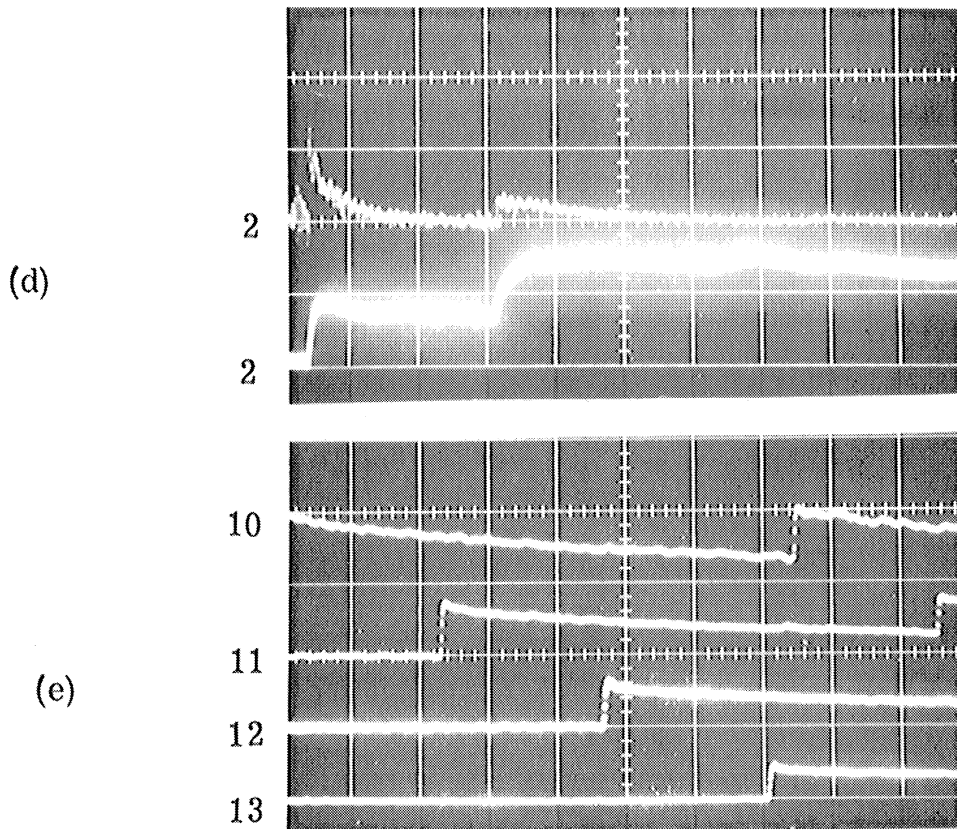
Fig. 3.3. (cont.)

(d) 15 in. Hg of $(2H_2 + O_2)$. 500 μsec/div. Station 2: Kistler 603, 134 psi/div. Lower beam: heat transfer gauge No. 16, 15.2 ohm, 19.0 ma, 0.00714 V/div.

(e) 15 in. Hg of $(2H_2 + O_2)$. 200 μsec/div. Station 10x: Kistler 601A, 19.8 psi/div. Station 11x: Kistler 603, 26.8 psi/div. Station 12x: Kistler 603, 31.2 psi/div. Station 13x: Kistler 601A, 41 psi/div.

apparent from the pressure records that the pressure is not constant behind the transmitted shock, but rather there is a trailing rarefaction similar to the trailing rarefaction behind the detonation in the driver. At stations farther from the diaphragm the pressure behind the transmitted shock decreases less rapidly.

The transmitted shock attenuates quite rapidly. The velocity of the transmitted shock as a function of distance from the diaphragm is shown in Fig. 3. 4 for initial driver pressures of 30, 20, and 15 in Hg. The velocity of the transmitted shock decreases about 50% in 10 ft. It should be pointed out that the driven section (i. e. , combustion tube) is square and has a cross sectional area 14% smaller than the driver, but the effects of the mismatch are believed to be small (the velocity of a transmitted shock in a 2 in. i. d. driven section exhibits a similar decay[1]).

When the detonation wave in the driver hits the diaphragm, a reflected shock travels up the tube, hits the end of the driver, reflects down the tube as a shock, and tends to catch up with the main shock front, as seen on the pressure traces. When 1/2 atm is used in the driver, the second shock is about twice as far behind as when 1 atm is used.

The heat transfer gauges show another important difference compared to the conventional shock tube. In Fig. 3. 3(a) at station 2 the second rise in voltage, which occurs 200 μ sec after the first rise, is interpreted as the interface between the driver and driven gases. At station 4 (Fig. 3. 3(b)) and farther distances from the diaphragm, no separation between the inter-face and the shock is observed. Also, when the initial driver pressure is reduced to 15 in. Hg of $2H_2 + O_2$, no separation is observed. Apparently the velocity of the interface does not attenuate as rapidly as the velocity of the shock, so that they converge rather than diverge as in a conventional shock tube.
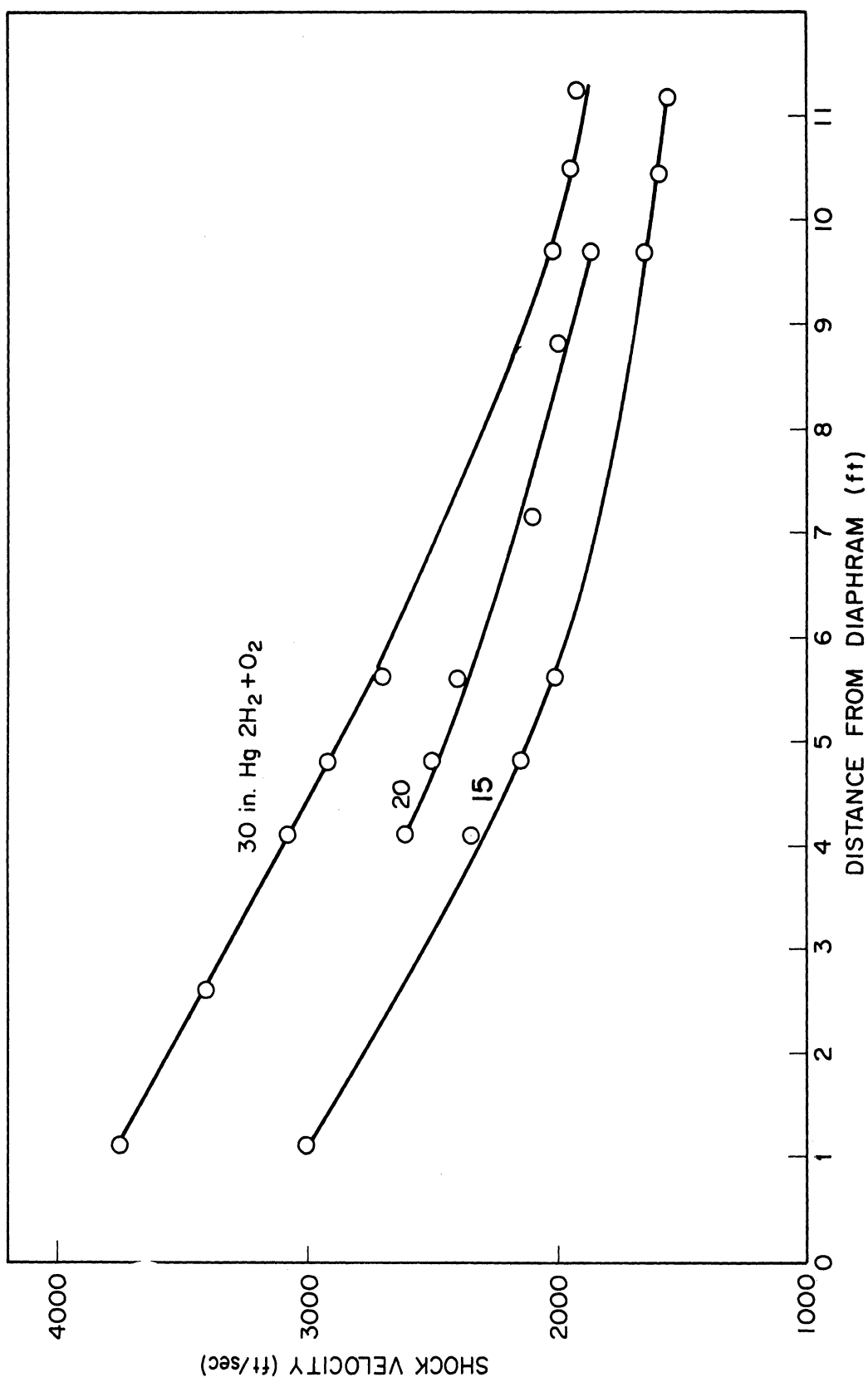
Fig. 3. 4. Velocity of the shock transmitted by the 2 in. i. d. detonation driven initiator vs. distance from the diaphragm.

Thus it is concluded that a driver which is operated in the detonation mode as described, transmits a pulse of high pressure - high temperature gas of varying and unknown properties. However, due to the rapid decay, the two phase detonation in the combustion tube rapidly out runs the gas from the driver.

3. Detonation Results

When two walls were coated with liquid, an average of 2.1 g with a standard deviation of 0.42 g was applied, which represents an 8.5μ thick film or 0.85 times stoichiometric. When one wall was coated with fuel, an average of 2.3 g with a standard deviation of 0.55 g was applied, which represents an 18.5μ thick film or 0.95 times stoichiometric. As will be shown the velocity of propagation was increasing slowly through the region of the test section and reached 3,500 to 4,500 ft/sec depending on the initial conditions.

Framing camera photographs taken with a Dynafax Camera[1] and snapshots taken with an image converter camera[2] of the self luminous light that showed that the combustion is initially confined to a narrow region along the wall. Light from the radiating gases does not fill the center of the test section until at least 500μ sec after passage of the initial shock. When only one wall is coated with fuel the velocity of propagation is nearly 1,000 ft/sec lower and correspondingly the initial luminosity is lower. In this case the outer edge of the combustion zone appears to fluctuate more, and variation of the intensity along the wall is more noticeable.

The spark schlieren photographs[1] showed the highly turbulent nature of the reaction zone. The turbulent structure immediately behind the leading shock front could be generated by perturbations in the shock front itself, as well as from pressure pulses which are sent out by the combustion zone. On the basis of the self-luminous photographs, it is felt that the turbulent structure near the centerline of the test section consists primarily of oxygen.

Streak photographs show some of the dynamics of the reaction zone. In Fig. 3.5(a), taken with fuel on two walls, the slit is located 1/16 in. from the wall. The leading shock front is perturbed only slightly over the distance observed, while the leading edge of the combustion front is perturbed quite strongly. The ignition delay time varies from a maximum of 19 μsec to a minimum of 6.5 μsec. When only one wall is coated with fuel as in Fig. 3.6(a), a similar structure is observed. The ignition delay time in this case varied from 36 μsec to 28 μsec. A regular pattern of nearly vertical (84°) lines separated by about 85 μsec is visible. These lines are possible caused by a transverse motion, although their origin is not understood.

Streak schlieren photographs of the film detonations with the slit located along the centerline of the tube are shown in Fig. 3.5(b) and 3.6(b), (c). The leading shock and several secondary shocks are clearly visible. Some of the pertinent velocities from the streak photographs are summarized in Table I. In Fig. 3.5(b) three secondary shocks are spaced about 32 μsec apart, or based on the velocity of the initial shock, the separation between secondary shocks is 1.6 in. The initial shock is travelling at 4050 ft/sec and the first and second secondary shocks are travelling downward at 8800 ft/sec. The third secondary shock is travelling slightly slower. In Fig. 3.6(b) the initial shock is travelling at 3350 ft/sec and the first secondary shock 5200 ft/sec. In both (b) and (c) the separation between secondary shocks is about 40 μsec and thus the distance between secondary shocks is again 1.6 in.

The following description of the secondary shocks is apparent from the streak photographs. The initial shock is perturbed by a secondary shock every 3 to 4 in. of travel. For the one wall case a secondary shock originates at the fuel surface at least 8 to 10 in. behind the initial shock front, and it travels along the fuel surface consuming vaporized fuel which is sufficiently mixed with oxygen. Near the origin of the secondary shock there is a relatively large
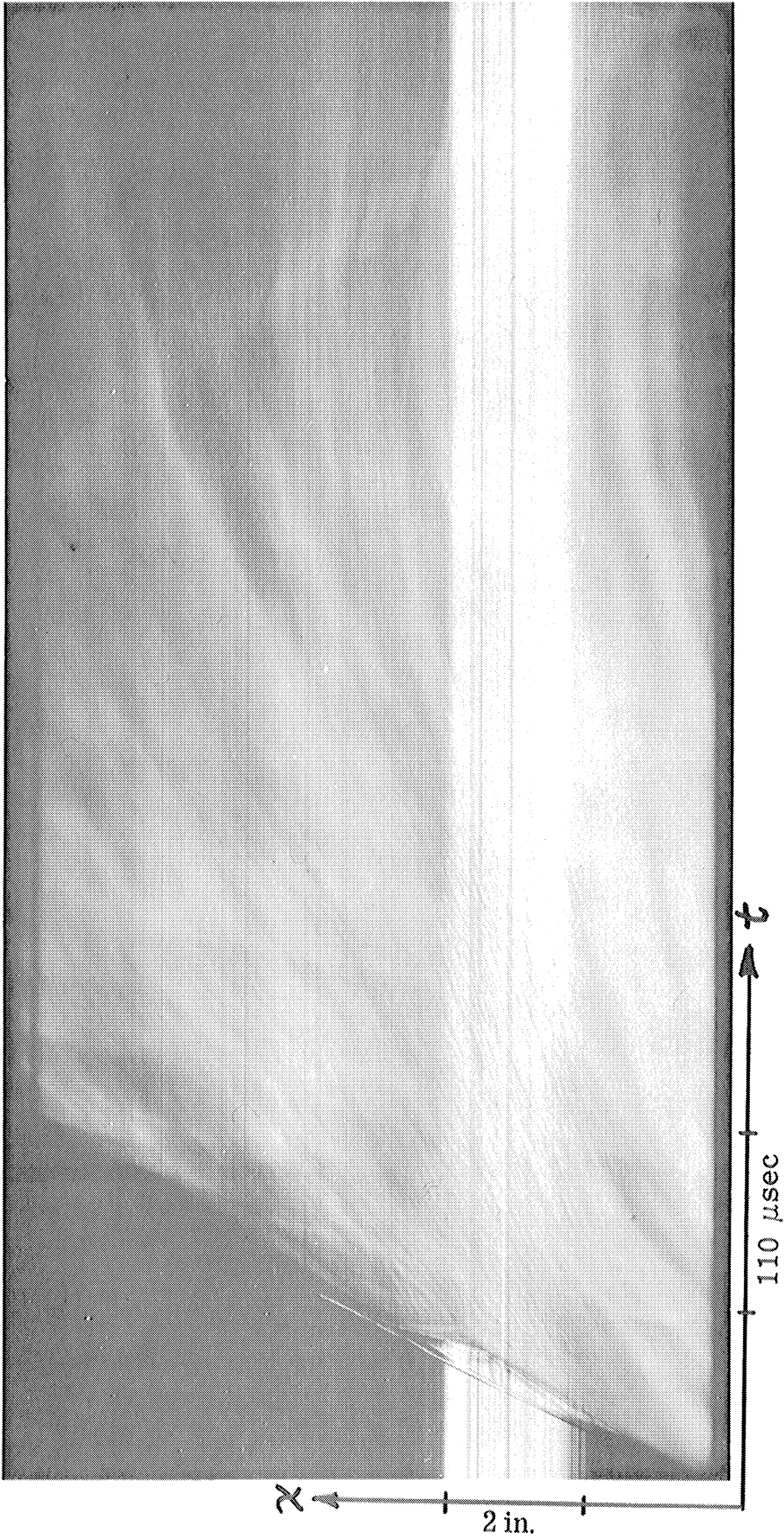
Fig. 3.5 Streak photographs of film detonations: fuel on two walls.
(a) Run 341. Self luminous light and shadowgraph with slit at the wall.

41
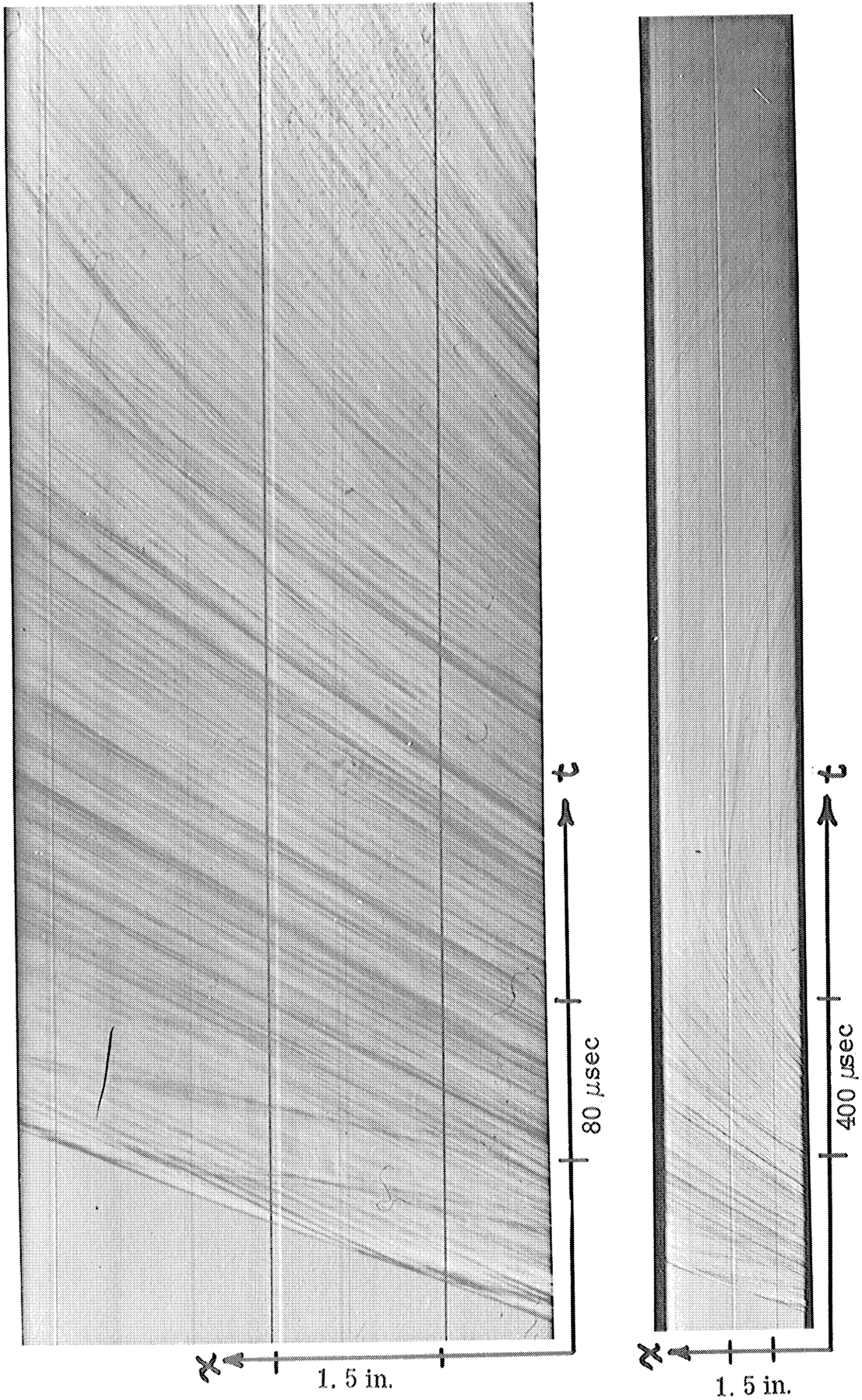
Fig. 3.5(b) Run 377. Schlieren photograph with slit at the centerline of the tube.

80 μsec

1.5 in.

400 μsec

1.5 in.

42
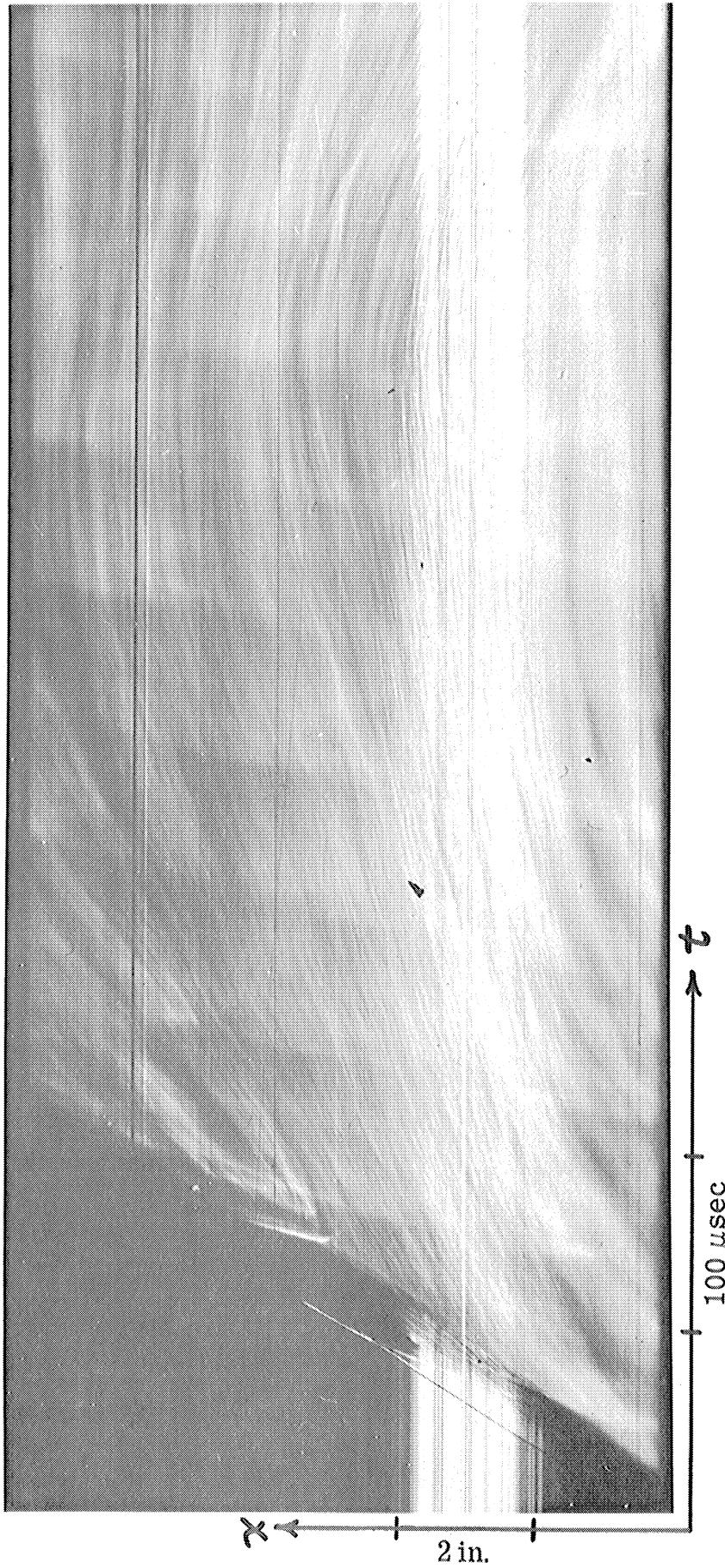
Fig. 3.6. Streak photographs of film detonations: fuel on one wall.
(a) Run 351. Self luminous light and shadowgraph with the slit at the wall.

43
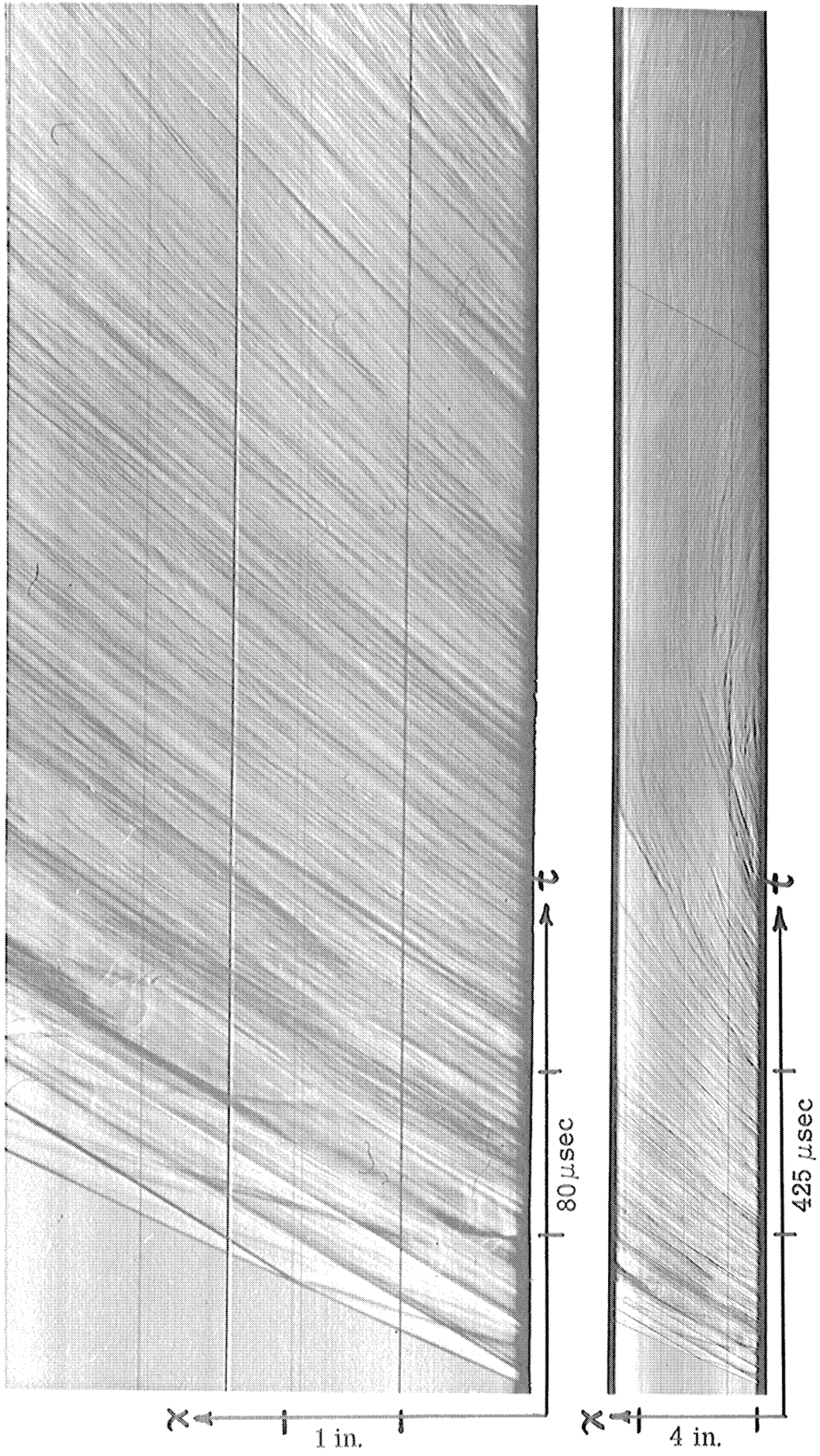
Fig. 3.6(b). Run 371. Schlieren photograph with slit at the centerline of the tube.

80 μsec

425 μsec

1 in.

4 in.
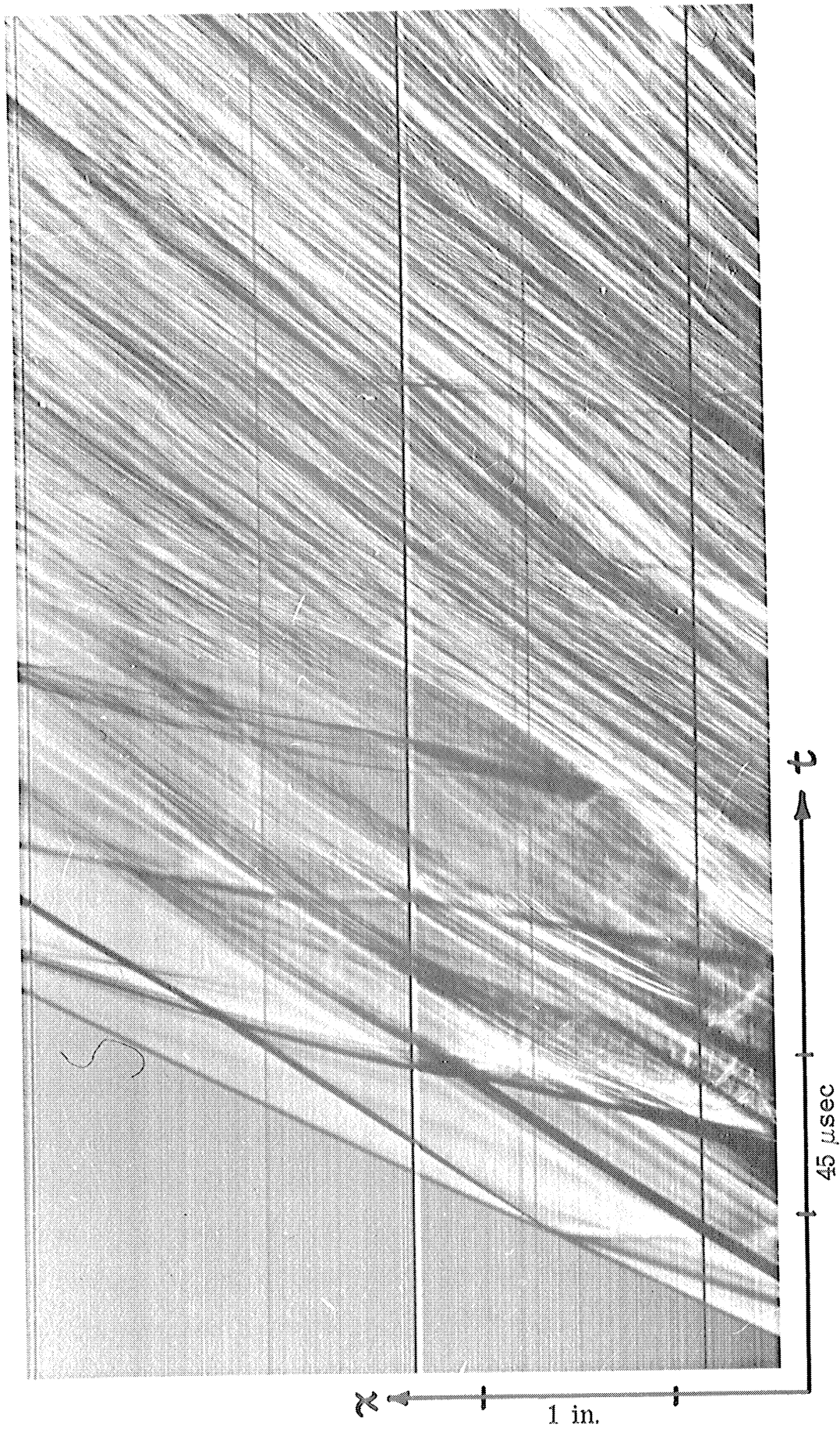
Fig. 3.6(c). Run 366. Schlieren photograph with slit at the centerline of the tube.

45

Table I. Analysis of Streak Photographs of Film Detonations

	Disturbance	α	V	M
Run 377	Initial shock	71	4050	3. 8
	First secondary shock	81	8800	2. 7
	Convective flow behind first secondary shock	66	3140	
	Convective flow after 400 μsec	53	1860	
	Flow turns after 1100 μsec	0	0	
Run 371	Initial shock	67. 5	3350	3. 1
	First secondary shock	75	5200	1. 5
	Convective flow behind first secondary shock	64	2840	
	Convective flow after 1000 μsec	32	870	
	Flow turns after 1800 μsec	0	0	

mount of mixed reactants and as the secondary shock moves down the tube progressively less vaporized fuel is available for chemical reaction. About 40 μsec after passage of this secondary shock, the layer of liquid becomes sufficiently prepared to generate another secondary shock. At the point of origin the secondary shock would move out in cylindrical fashion and head both upstream and downstream. The branch going upstream against the convective flow would soon run out of fuel and decay, while the branch moving downstream with the convective flow is driven at its base by the available reactants. Thus the forward moving secondary shocks are curved with the edge of the shock near an inert wall trailing the edge near the fuel layer.

For the case when two walls are coated with fuel, the curvature of the secondary shocks is greatly reduced and thus travel at a considerably higher velocity. Since in our experiments the thickness of the fuel layer for the two wall case was about 1/2 that for the one wall case, and since the convective flow velocity within the reaction zone is higher, the secondary shocks in Fig. 3.5(b) seem to originate only about 1/2 as far behind the initial shock as in the one wall case.

As will be discussed below the secondary shocks are also apparent in the pressure traces. Since the Dynafax photographs of the self-luminous light show a continuous combustion along the wall, it is rather puzzling why the secondary shocks would be generated at all. It is possible, however, that a local explosion is superimposed on a deflagration which is occurring continuously at the interface between the oxygen which diffuses towards the wall and the fuel which diffuses outwards. While the deflagration continues, the vaporized, and later mechanically stripped, fuel layer builds up to the point where a localized "gaseous" detonation can occur. An analogous situation was observed with the 2600 μ diam drops where the microspray in the wake of the drop builds up and then is violently consumed.

Komov and Troshin[16] were the first to study the structure of a film detonation, and it is interesting to compare their work with the above results. They used a horizontal tube 2 cm by 2 cm by 2 m long and coated the bottom and vertical walls with various fuels. For hexadecane and oxygen an average detonation velocity of 5340 ft/sec was achieved and the ignition delay oscillated from 5 to 20 μ sec. Two secondary shocks travelling at 8540 ft/sec were observed photographically, and the origin of the secondary shocks was shown to be approximately 4-5 tube diameters from the initial shock front. The secondary shocks were spaced about 55 μ sec apart. Komov and Troshin point out that film detonations are unstable in the same sense as a gaseous

detonation since there is a variation in the ignition time delay and variation in the velocity of the flame movement, and that the secondary shocks provide an important means of maintaining the initial shock front.

Records from the pressure and heat transfer gauges of the film detonations with the fuel on two walls and on one wall are shown in Fig. 3. 7 and 3. 8 respectively. Both filtered Kistler transducers and the lead metaniobate transducer with the acoustic absorbing rod were used. For the two wall case the initial pressure jump at station 12x in Fig. 3. 7 (a) is 300 psi and at station 10x in (b), 280 psi. Some variation in pressure rise and propagation velocity are observed from run to run, and no definite correlation of this variation with the amount of fuel applied to the wall could be deduced. An initial pressure jump of 280 psi in (b) corresponds to a pressure ratio of 20. 4; using normal shock relations this yields u_s = 4500 ft/sec, which agrees quite well with the average velocity between stations 9x and 10x as obtained from the time scale of Fig. 3. 7 (b). The pressure decreases after the initial rise as heat is added to the flow and later due to the trailing rarefaction.

The propagation velocity of the detonation as a function of distance from the driver was obtained from records such as Fig. 3. 7(e) by measuring the time for the wave to travel a known distance. In this figure the average propagation velocity between stations 9x-10x-11x-12x-13x remains nearly constant at 4640 ± 60 ft/sec. The propagation velocity is plotted versus distance from the driver diaphragm in Fig. 3.9 for several different runs. Each of the lower two curves represent 7 different runs although measurements were not necessarily made at each station for each run.

The top curve represents two runs which were made with 1/2 atm of oxygen in the combustion tube. This was the most convenient way to vary the mixture ratio. While it is not the purpose of this study to investigate the effect of mixture ratio on the propagation, it is worth noting that increasing the mixture ratio from 0. 9 to 1. 8 times stoichiometric increases the velocity by a factor of 1. 2.

Fig. 3. 7. Pressure and Heat Transfer Records of Liquid Film
Detonations--Fuel on Two Walls.

(a) Run 342, 2. 3 g DECH, 29. 5 in. Hg O_2. Station 8: Kistler Mod.
603 pressure transducer (in the fuel), 312 psi/div and 50 μsec/div,
triggered at station 7. Station 12x: Kistler 601A (90° out of tne fuel),
198 psi/div and 200 μsec/div triggered at station 11x. Lower trace :
Heat transfer gauge No. 16 at station 12x (90° out of the fuel), 16. 8
ohm, . 02 V/div and 200 μsec/div triggered at station 11x.

(b) Run 362, 2. 6 g DECH, 29. 2 in. Hg O_2. 200 μsec/div. Station 8:
Kistler 603 (in the fuel), 156 psi/div triggered at station 7. Station
10x: Mod 6. 7 pressure transducer (90° out of the fuel), 195 psi/div
triggered at station 9x. Lower trace: Heat transfer gauge No. 34 at
station 10x (90° out of the fuel), 12. 7 ohm, . 02 V/div triggered at
station 9x.
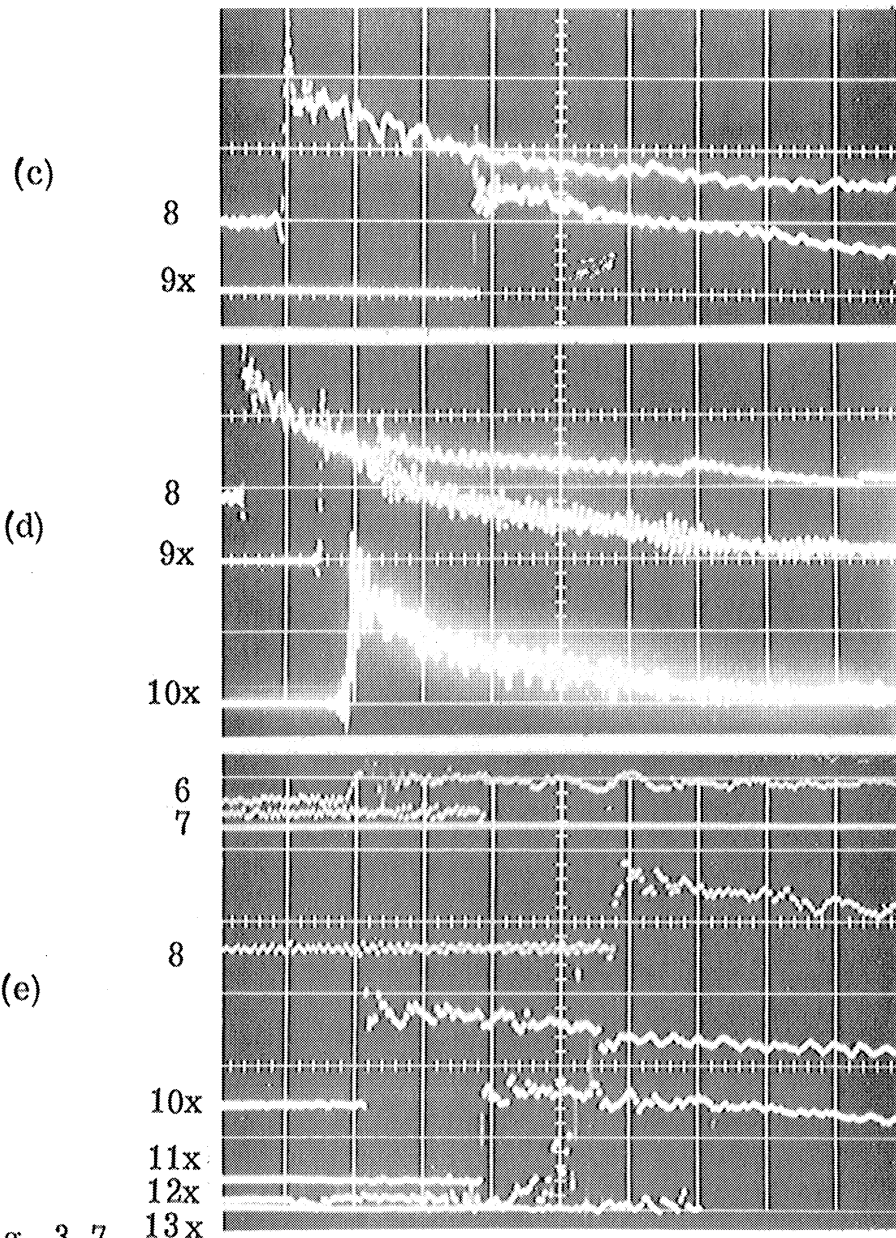
Fig. 3. 7.

(c) Run 353, 2. 6 g DECH, 29. 5 in. Hg O_2. 200 μsec/div triggered at station 7. Station 8: Kistler 603 (in the fuel), 156 psi/div. Station 9x: Mod 6. 6 pressure transducer, 195 psi/div.

(d) Run 354, 2 g DECH, 29. 5 in O_2. 500 μsec/div triggered at station 7. Station 8: Kistler Mod 603 pressure transducer (in the fuel), 156 psi/div. Station 9x: Kistler 601A (in the fuel) 164 psi/div. Station 10x: Kistler 601A (in the fuel) 198 psi/div.

(e) Run 379, 1. 9 g DECH, 29. 4 in. Hg O_2. 100 μsec/div. Station 8: Kistler Mod 603 pressure transducer (in the fuel) triggered at station 5, 312 psi/div. Station 10x: Mod 6. 6 pressure transducer (in the fuel), triggered at station 9x, 195 psi/div. Station 11x: Mod 6. 7 pressure transducer (in the fuel) triggered at station 9x, 195 psi/div.
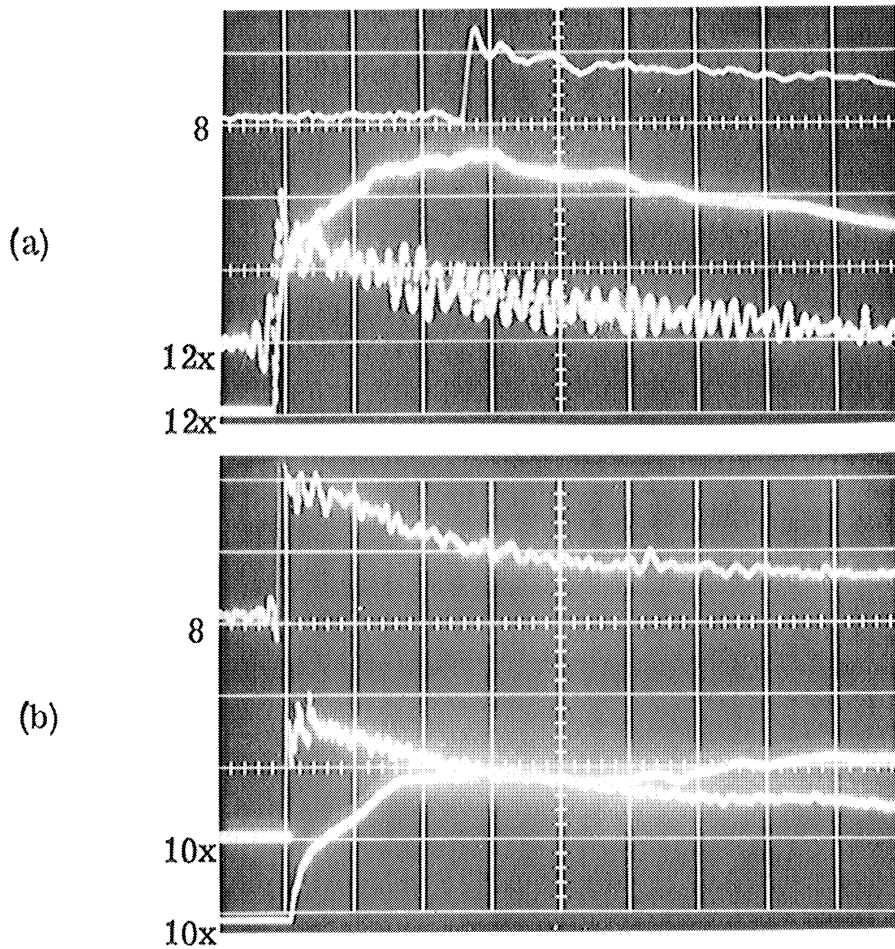
50
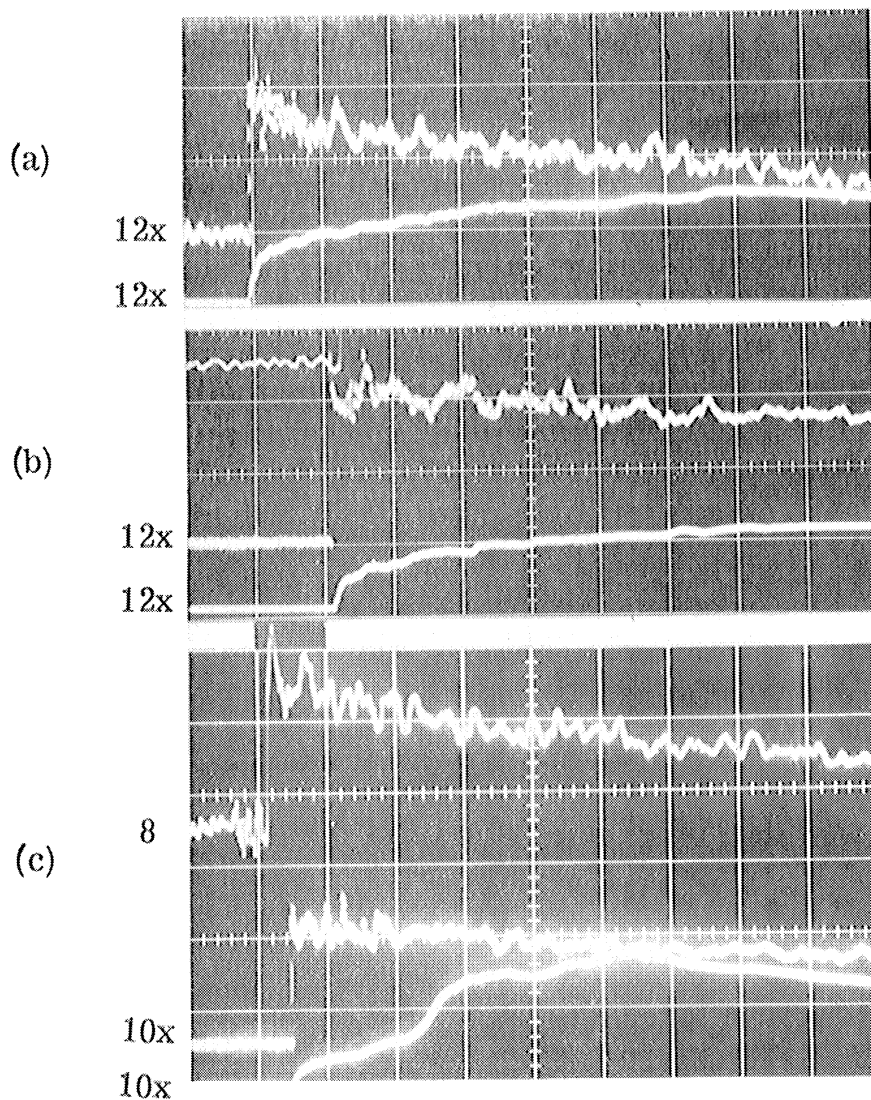
Fig. 3.8. Pressure and Heat Transfer Records of Liquid Film
Detonations—Fuel on One Wall.

(a) Run 348, 2.5 g DECH, 29.4 in. Hg O_2. 200 μsec/div. Station 12x:
Kistler 601A (in the fuel), 99 psi/div, and (lower beam) heat transfer
gauge No. 16 (180° out of the fuel), .02 V/div.

(b) Run 351, 2 g DECH, 29.3 in. Hg O_2. 100 μsec/div. Station 12x:
Mod 6.7 pressure transducer (in the fuel), 78 psi/div, and (lower trace)
heat transfer gauge No. 16 at station 12x (180° out of the fuel), .02 V/div.

(c) Run 361, 1.6 g DECH, 29.2 in. Hg O_2. 200 μsec/div. Station 8:
Kistler 603 (in the fuel), 62 psi/div, triggered at station 7. Station 10x:
Mod 6.7 pressure transducer (90° out of the fuel), 78 psi/div, triggered
at station 9x. Lower trace: Heat transfer gauge No. 34 at station 10x
(90° out of the fuel), .02 V/div.
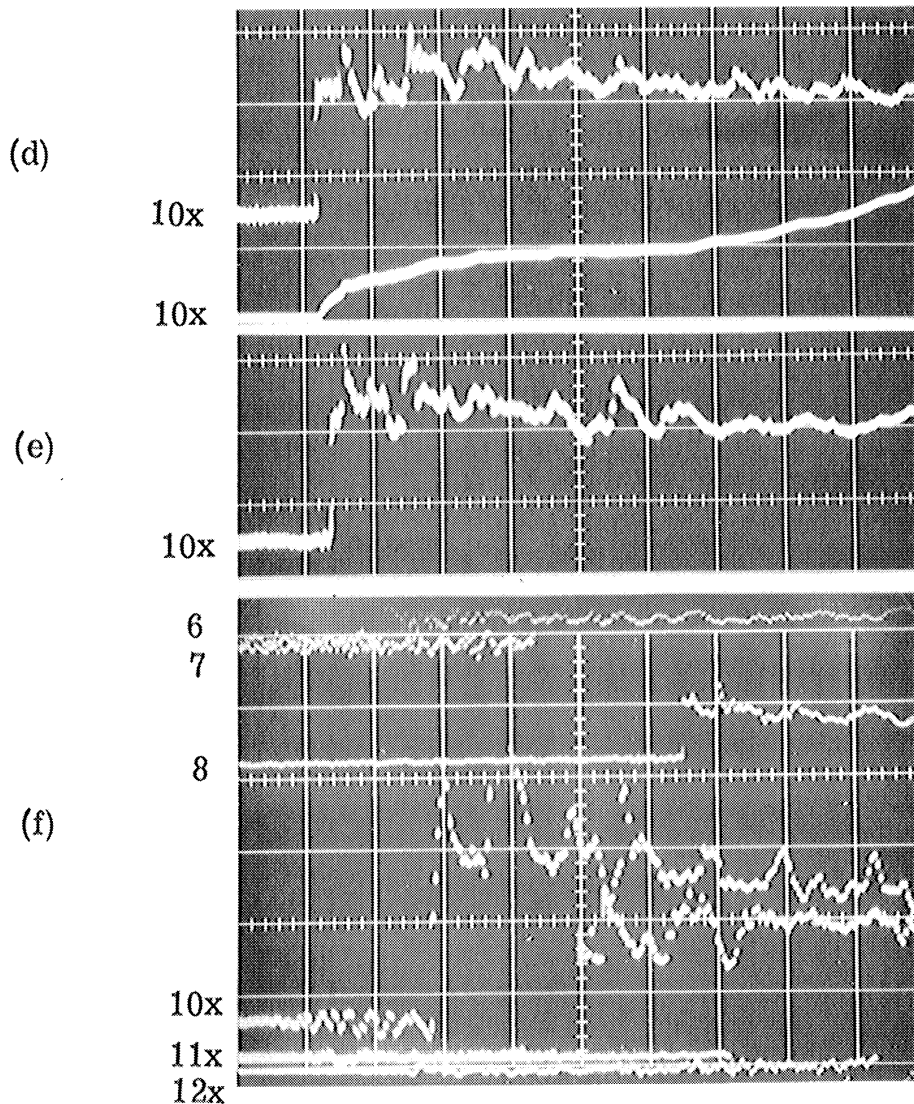
Fig. 3.8.

(d) Run 365, 2.7 g DECH, 29.2 in. Hg O_2. 50 μsec/div. Upper trace: Mod 6.7 pressure transducer at station 10x (90° out of the fuel), 78 psi/div. Lower trace: Heat transfer gauge No. 16 at station 10x (90° out of the fuel), .02 V/div.

(e) Run 364, 2 g DECH, 29.2 in. Hg O_2. 50 μsec/div. Mod 6.6 pressure transducer at station 10x (90° out of the fuel), 78 psi/div.

(f) Run 374, 2.4 g DECH, 29.5 in. Hg O_2. 100 μsec/div. Station 8: Mod 6.6 pressure transducer (in the fuel), triggered at station 5, 195 psi/div. Station 10x: Kistler 603 (180° out of the fuel), triggered at station 9, 62 psi/div. Station 11x: Mod 6.7 pressure transducer (180° out of the fuel), 78 psi/div.
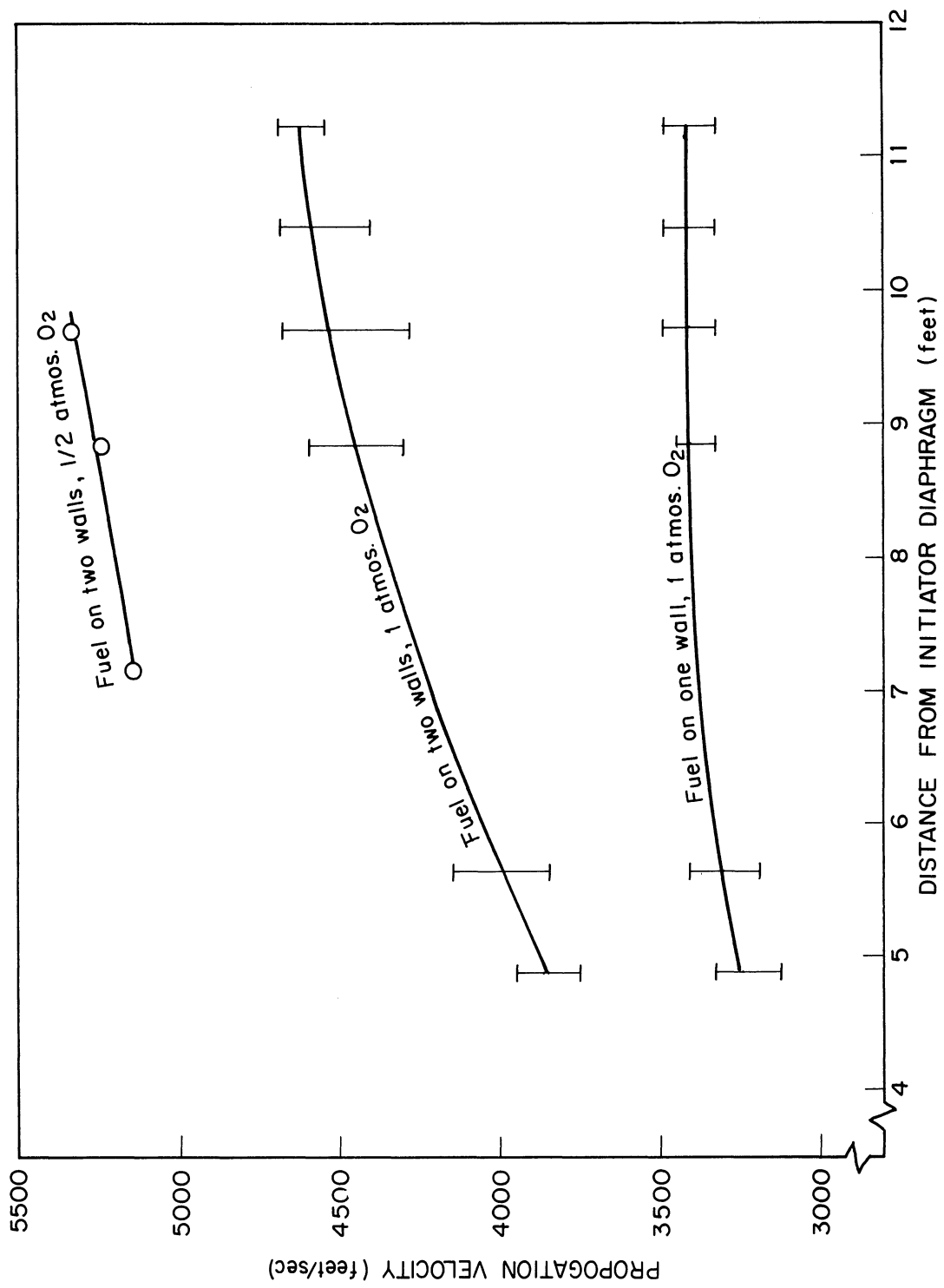
Fig. 3.9. Propagation velocity vs. distance from the initiator diaphragm for film detonations.

53

For the case when one wall is coated with fuel the initial pressure jump at station 12x is 160 psi for runs 348 and 351 (Fig. 3. 8(a), (b)) and 128 psi for run 361, which corresponds to pressure ratios of 12. 1 and 9. 8 psi respectively. In run 361 the velocity of propagation, as obtained from the time between stations, is lower and the amount of fuel placed on the walls was somewhat less. The pressure records again indicate that normal shock relations can be used across the initial shock front. Similarly to the other two phase detonations, the pressure behind the initial shock decreases but not as rapidly as when two walls were coated with fuel.

The secondary shocks are quite apparent during the first 200-400 μ sec in the records taken with the lead metaniobate transducer when one wall is coated with fuel. In Fig. 3. 8(d) the first secondary shock occurs 30 μ sec after the initial shock and has a pressure jump of 40 psi and a pressure ratio of 1. 25 which would be representative of a normal shock travelling at Mach 1. 1. The streak photographs indicated that the first secondary shock (for a different run) travels at Mach 1. 23 at the centerline of the tube. Considering the apparent curvature of the secondary shocks the agreement is surprising. The secondary shocks do not appear as a series of normal shocks but rather as a series of pressure spikes superimposed on the initial pressure jump and spaced roughly 40 μ sec apart (in agreement with the streak photographs). Figure 3. 8(e) was made with a different transducer but of identical design and shows similar results.

Figure 3. 8(f) shows the type of data from which the propagation velocity at various positions along the tube was obtained for the one wall case. The results for 7 different runs are shown in the bottom curve of Fig. 3. 9; a velocity of 3400 ft/sec was reached on the average.

Representative wall temperature data is shown in Fig. 3. 7(a), (b) and 3. 8(a)-(d). In each case the heat transfer gauge is flush mounted in a dry wall. It was not possible to obtain meaningful data with gauge coated with fuel.

In general the wall temperature increases during the first 460 μsec for the two wall case and during the first 1000 μsec for the one wall case, and then levels out or decreases. The wall temperature data was converted to heat transfer rate according to the procedure outlined in Ref. (3). The results of the two wall case for 4 runs (including Fig. 3.7(a) and (b)) are shown in Fig. 3.10. The heat transfer rate is greater than 1000 Btu/ft^2-sec during the first 460 μsec. For the one wall case (Fig. 3.11) the heat transfer rate is lower initially and increases with large fluctuations which reflect a more unsteady combustion process. After 1000 μsec a sharp drop in heat transfer is noted. More detailed treatment of the film detonation results is presented by Ragland[9].

4. Dynamics of the Liquid Film

Borisov et al[17, 18, 19] studied the dynamics of 8 mm - 0.1 mm thick layers of various liquids and industrial vaselines after passage of gaseous detonation waves. Apparently no combustion of the liquid layer occurs in their experiments. A micro-mist ($\sim.5\mu$) was observed along the wall after a certain time delay after passage of the shock front, and they propose that this mist is formed because of the pattern of reflected shock waves which develop in the liquid (due to the shock in the gas). However, the extent to which the reflected shock waves in the liquid actually contribute to the formation of the mocro-mist is not at all clear. Furthermore, it is felt that for liquid layers 10-20μ thick these waves would rapidly attenuate.

Borisov distinguishes between three distinct phases of the break-up process: 1) the period after passage of the shock during which the liquid surface remains flat, 2) disturbance or bulging of the surface, and 3) tearing free of a mist from the surface. For a layer of glycerin of the order of 5 mm thick that is processed by a 1 atm $2H_2 + O_2$ detonation wave, the duration of the stages was
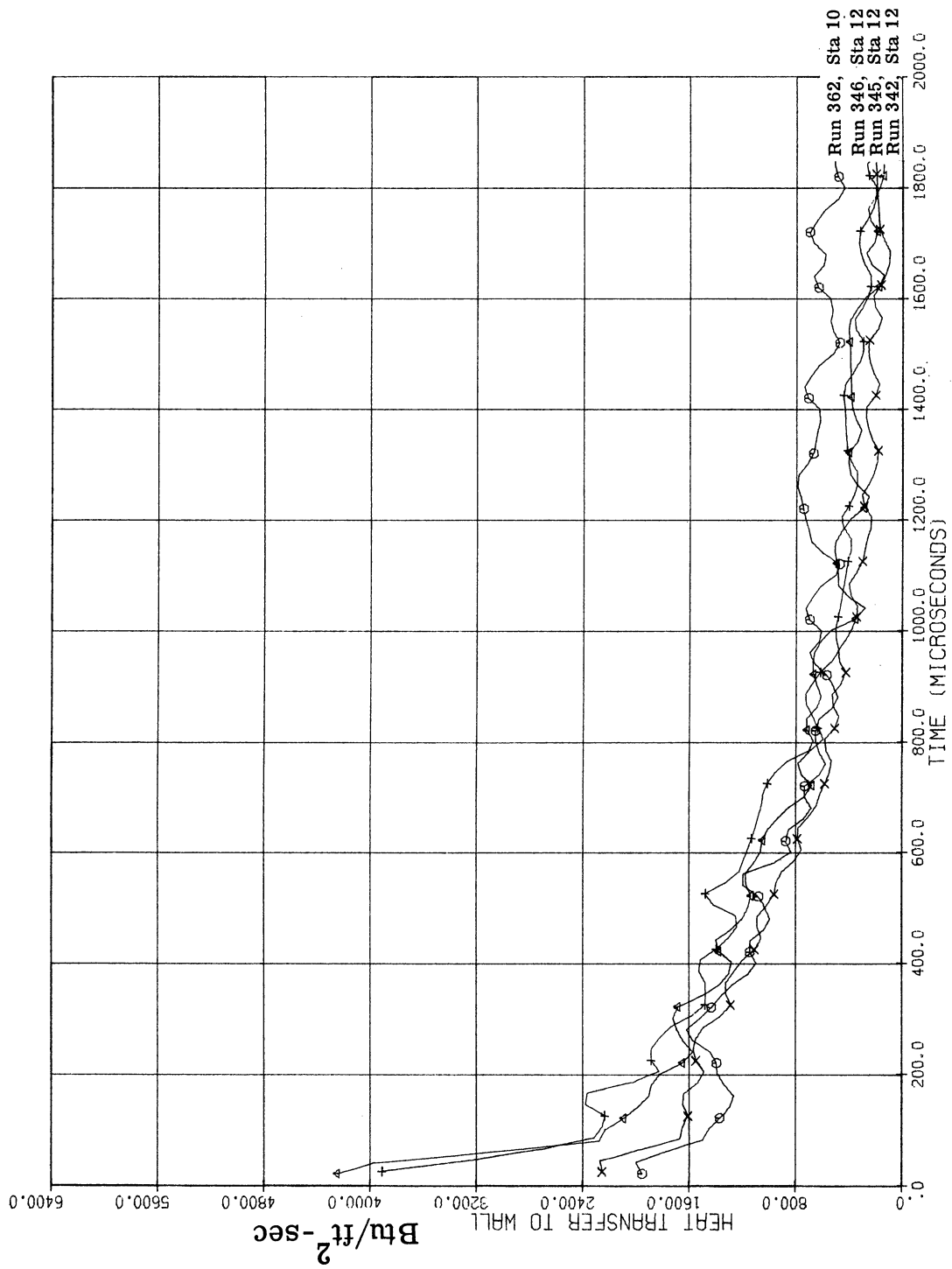
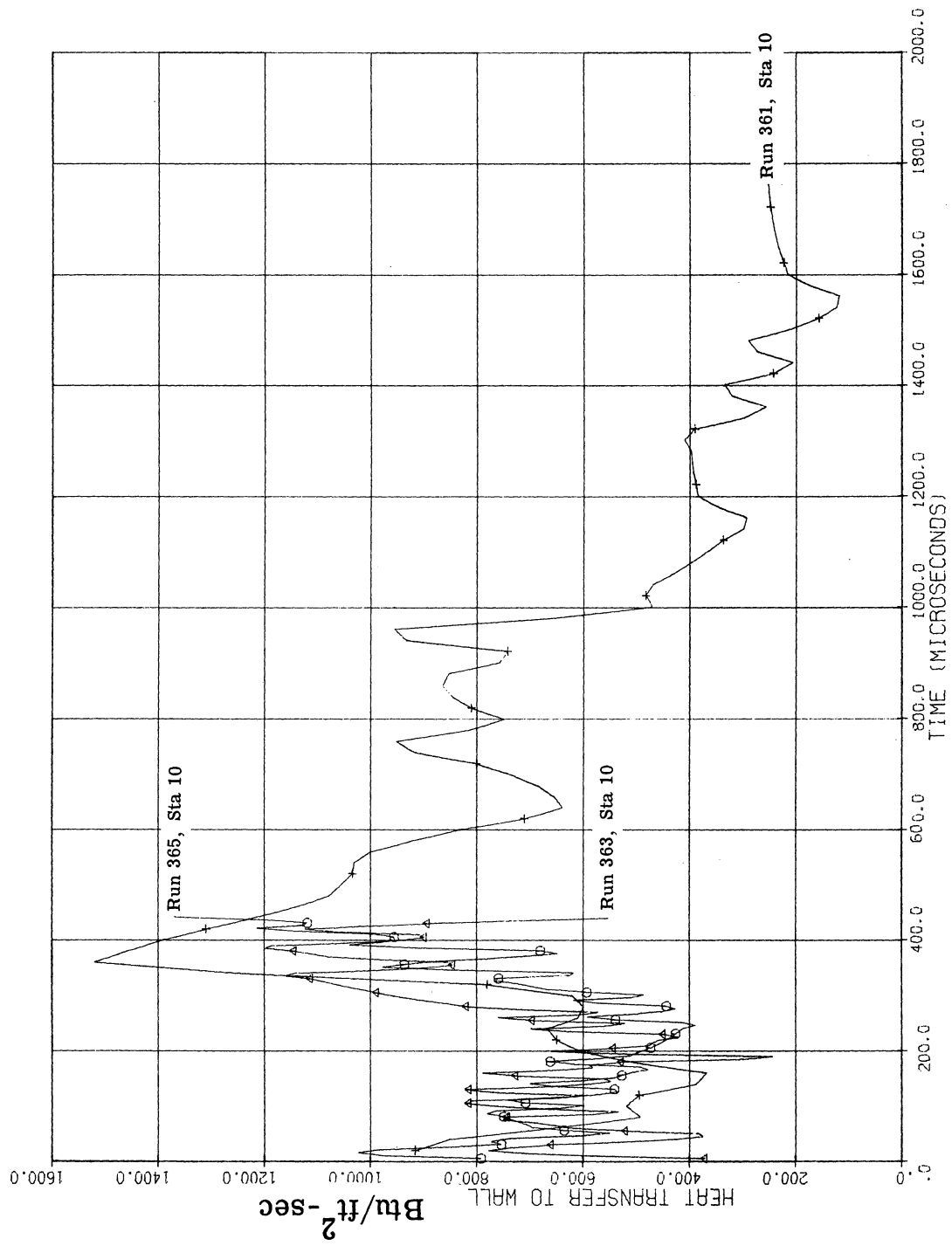Fig. 3.10. Heat transfer to the wall for the film detonations: fuel on two walls.

Fig. 3.11. Heat transfer to the wall for the film detonations: fuel on one wall.

1) 300 μsec, 2) 500 μsec, and 3) 400 μsec. For a layer of industrial vase-
line 100μ thick processed by a one atm $CH_4 + O_2$ detonation, it appears that
approximately 300 μsec is again required before the surface of the vaseline
distorts. The effect of varying the thickness of the layer and the type of
liquid on the duration of the above stages has apparently not been systemat-
ically investigated.

An exploratory experiment on the behavior of a thin layer of DECH in
a shock tube was reported in Ref. (2). A layer of DECH, estimated to be
5 to 50μ thick, was painted on a flat plate that was mounted in a 1.5 x 2.5 in.
shock tube. At the time of the tests the fastest shock which could be obtained
was Mach 2.2 in 1 atm air. The plate was back-lit with collimated light and
a sequence of photographs were taken with the image converter camera.
The apparent thickness of the liquid layer increased gradually after passage
of the shock wave and the edge of the layer was distinctly ragged. The thick-
ness of the layer increased to about 0.05 in. after 140 μsec and retained this
thickness for an additional 40-60 μsec.

It is not clear for thin films whether the micro-spray is formed by an
internal pressure wave process as suggested by Borisov et al, or by the
shearing action of the convective flow. The formation of the micro-spray
in the wake of a drop, under the conditions of interest for two-phase deto-
nations, is believed to be a shearing process (after deformation of the drop)[3]
rather than a shattering of the drop due to build up of internal pressure due to
reflected shock waves inside the drop. Thus it is possible that the shear
stress at the wall within the boundary layer could be the major force tending
to form the micro-spray along the wall.

If the shear stresses form the micro-spray, then it follows that the
micro-spray would be produced more slowly in a burning layer of liquid,
since burning greatly reduces the shear stress.[3] On the other hand, burning
increases the vaporization rate. Thus it is felt that the most important pro-
cess by which the fuel enters the reaction zone of the detonation is through
vaporization.

Although the flow within the reaction zone is certainly turbulent, it is interesting to calculate how much fuel would be vaporized by a diffusion limited, chemically reacting, laminar, boundary layer. The solution of this type of boundary layer is given by Ragland[20]. Application of the theoretical solution to conditions representative of the flow conditions for the film detonation with two walls coated with DECH showed that 25% of the fuel would be vaporized after 460 μsec. Thus it seems reasonable that vaporization from a turbulent boundary layer could account for nearly all the mass addition.

On the basis of the foregoing experiments and reasoning the following explanation of a film detonation is offered. The initial shock front compresses, preheats, and sets into motion the gaseous oxidizer. Heat is transferred from the oxidizer to the layer of fuel and, because of the relatively low thermal diffusivity of the liquid, little heat is lost to the wall and the surface of the liquid is maintained at its equilibrium boiling point. The evaporated fuel diffuses towards the center of the tube and the oxygen diffuses towards the wall. After a time delay of 6 to 36 μsec ignition occurs within the boundary layer which increases the evaporation rate due to the increased temperature and increased turbulence level of the boundary layer. The combustion process within the boundary layer is not completely steady as evidenced by the formation of secondary shocks. The heat release due to combustion drives the initial shock front by the expansion of the hot gases within the reaction zone and by the secondary shocks which collide with the initial shock.

IV. SHATTERING OF LIQUID DROPS

The spray detonation studies, published earlier and also presented in the early portion of this report, established the importance of the aerodynamic shattering of the liquid drops. It has been shown that the drop breakup time is the major determinant of reaction zone length. This phase of the study has continued and the progress made during the past year is reported herein. Some repetition of earlier reports is included for the sake of continuity. It should be noted that all of the studies are at high Weber numbers ($\gg 10$) so that the bag type of break-up is not of concern here.

In the following sections further results of a shock tube investigation are presented followed by an analytical treatment of boundary layer stripping from the drop. The experimental and theoretical results are then combined to examine the validity of the model.

1. Experimental Apparatus

The experimental arrangement used in this study is shown schematically in Fig. 4.1. A stream of extremely stable, uniform size, equally spaced drops is obtained by vibrating a small jet of water at the Rayleigh instability frequency. These drops fall vertically through the test section of a helium driven shock tube by means of an opening in the top and bottom. Since the test section is open to the atmosphere, the initial pressure in the driven section is $P_1 = 1$ atmosphere. A collimated beam of high intensity light is used to back-light the drops, and both image converter and rotating drum type cameras are employed to photograph the interaction phenomena. A more detailed description of the experimental equipment is given elsewhere[2, 3].

The experimental procedure consists of obtaining a time history of the deformation, disintegration, and displacement of a drop by taking a series of individual shadow photographs at different time intervals after the shock wave intercepts the drop and by taking streak photographs.
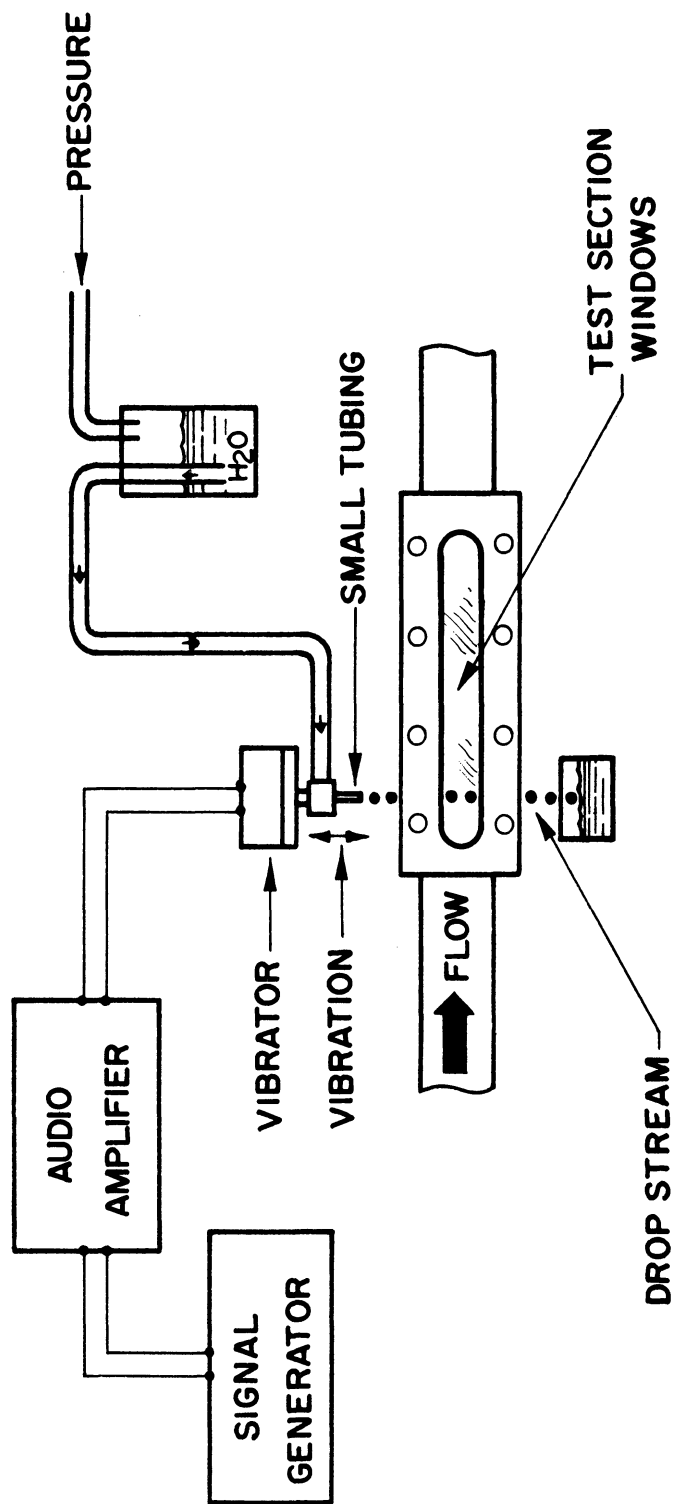
Fig. 4.1. Schematic drawing of test section.

61

A modified Beckman and Whitley Dynafax camera was employed to obtain the streak pictures. The arrangement, using a 0.125 in. wide slit, is shown in Fig. 4.2. The individual photographs, which are 0.1 μsec exposures, were taken with a Beckman and Whitley Model 501A image converter camera. This camera is triggered by a thyratron circuit which is fired by a signal produced from a pressure switch located in the wall of the shock tube just upstream of the test section, as shown schematically in Fig. 4.3. A time delay unit is used to control the time that elapses between the moment that the shock passes this switch and the instant that the picture is taken. A measurement of the transit time between two pressure sensors was utilized to determine the shock speed. Extreme care was taken to insure that the testing time available was greater than the anticipated breakup time and that the drop separation distance was sufficient to rule out proximity effects.

2. Results and Discussion

The results discussed here are for experiments that cover the shock Mach number range of $M_S = 1.5 - 3.5$ in air with water drops having diameters in the range $D_O = 750 - 4400\mu$. Image converter and streak photographs of typical shock wave-water drop interactions are shown and the resultant data shown in terms of drop deformation, displacement, and breakup time.

Figure 4.4 (a repeat from earlier work[3]) shows the sequence of events leading to the shattering of 750μ drops by a $M_S = 2.0$ shock wave where initially the convective flow velocity relative to the motionless (in the stream direction) drop is approximately sonic and equal to 1415 ft/sec. The highlight which appears in the undisturbed drops is an image of the spark light source and it remains very bright and distinct until the growth of surface disturbances destroys the drop's ability to act as a focusing lens. In this sequence, the highlight disappears between 7.4 μsec and 8.8 μsec, and the planar incident shock wave that is visible in several of the pictures moves
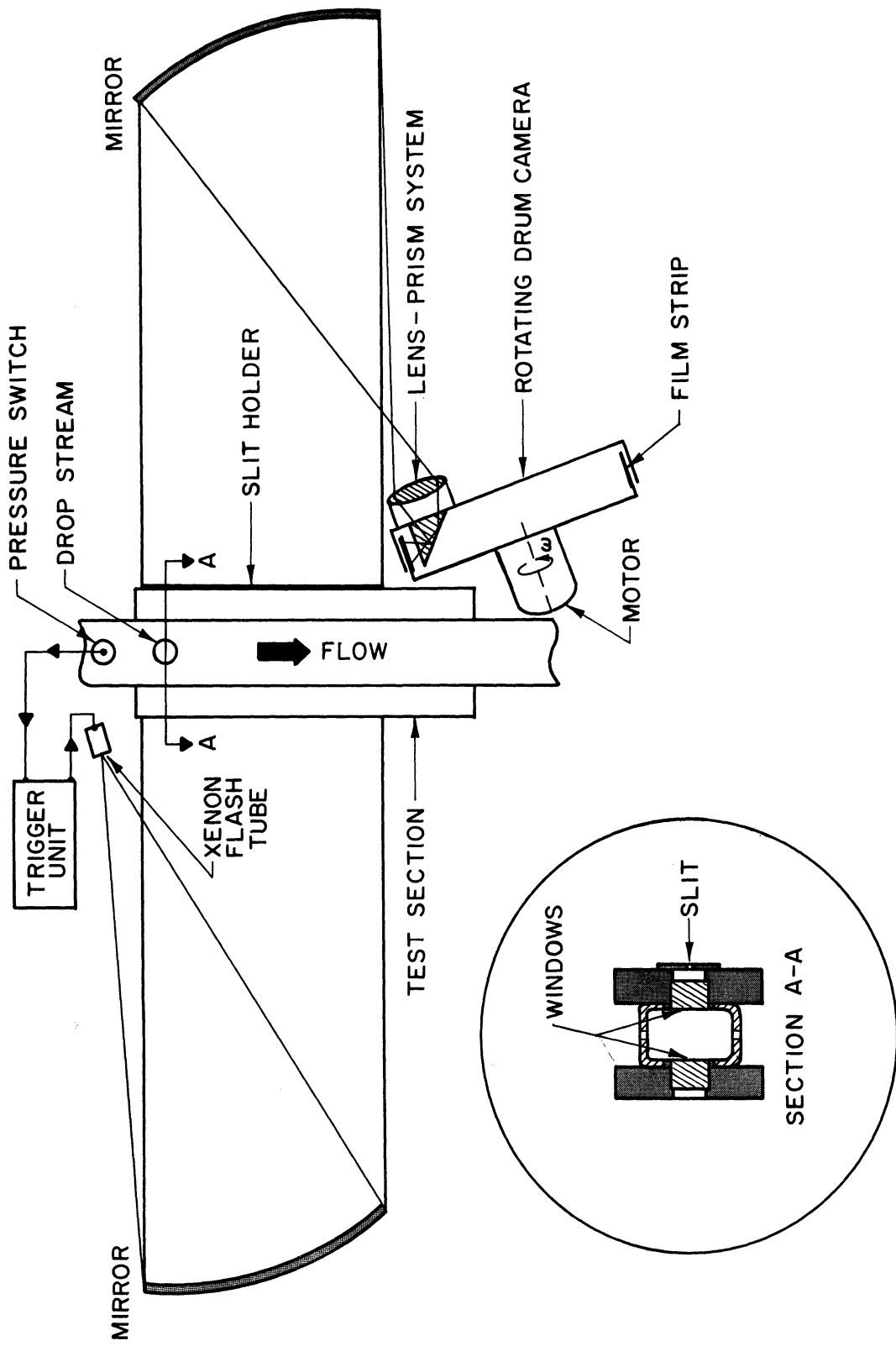
Fig. 4.2. Diagram of streak photography system.

63

PRESSURE SWITCH

DROP STREAM

TIME
DELAY

A

A

FLOW

TEST SECTION

OPTICAL BENCH
TRANSLATION

COLLIMATED LIGHT
BEAM

SPARK
LIGHT
SOURCE

WINDOWS

SECTION A-A

OPTICAL BENCH

IMAGE
CONVERTER
CAMERA

Fig. 4.3. Image converter camera arrangement.

t = 7.4 μ Sec

Undisturbed

t = 5.6 μ Sec
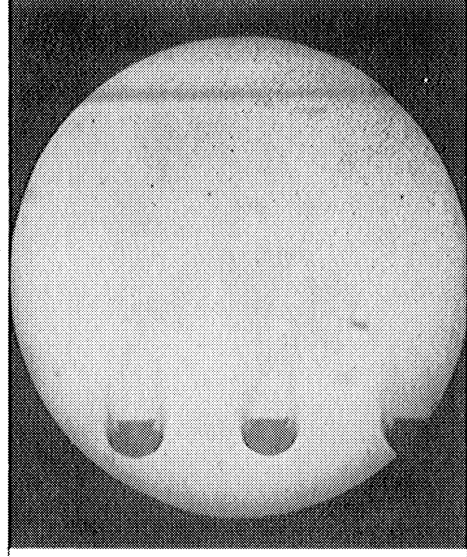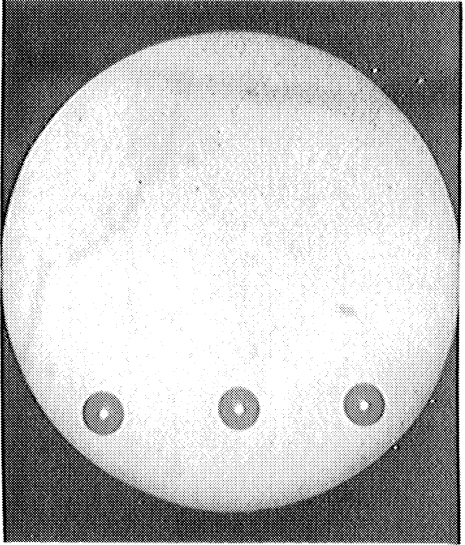
t = 8.8 μ Sec

Fig. 4.4. Shadow photographs of 750μ droplets.

t = 15.8 μ Sec

t = 26 μ Sec

t = 10.8 μ Sec

t = 20.8 μ Sec

Fig. 4.4. (cont.)

66
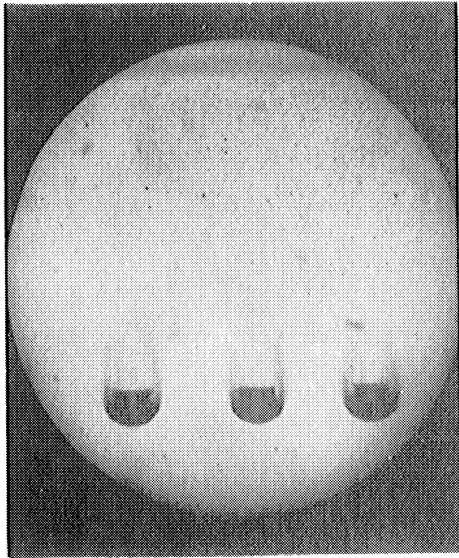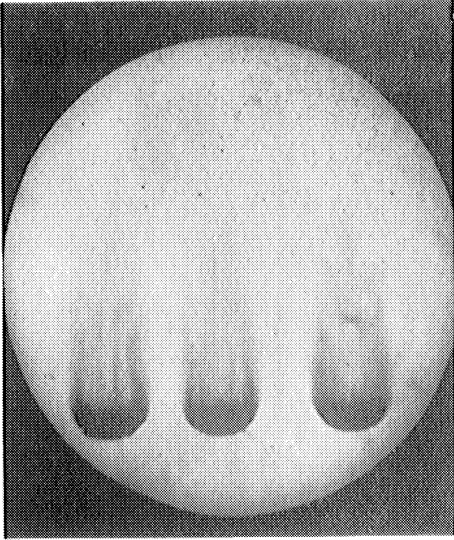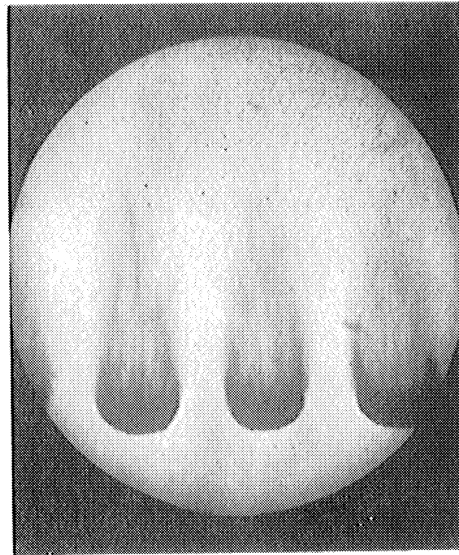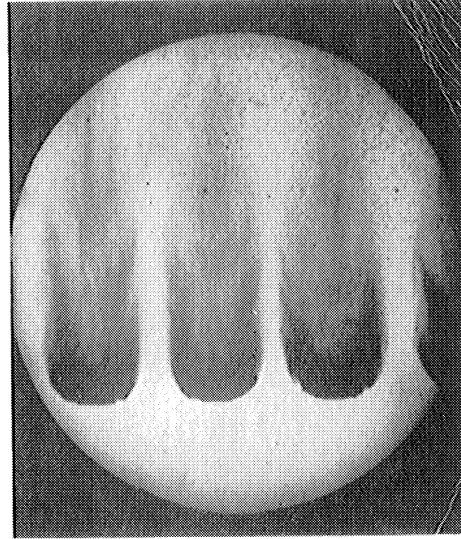
from left to right across the drops. The observed breakup can be temporally divided into two rather distinct stages. The first one, or dynamic stage, is the period during which the drops are flattened as a result of the external pressure distributions. The second stage is characterized by a surface stripping process which is produced by the shearing action of the convective flow and which rapidly reduces the drops to clouds of micro-mist. At $t = 26$ μsec after the shock made initial contact with the drop, this latter stage is well developed.

Measurements from these and other photographs establish for the first time that the deformed drops are planetary ellipsoids. An example of this is shown in Fig. 4.5 where the experimental conditions were $M_s = 3.5$, $D_o = 2700 \mu$, $P_1 = 1$ atm, and the picture was taken at 14 μsec. The convective flow is supersonic so that a bow shock is formed and is readily visible. Figure 4.6 is a tracing of the photograph in Fig. 4.5 showing the elliptical shape which the drop assumes. The shaded area in the figure represents the volume occupied by the original mass of the drop assuming that its shape is a planetary ellipsoid. The eccentricity of the elliptical profile changes rapidly with time as shown in Fig. 4.7 where again the elliptical shapes have been traced directly from enlarged photographs, and the shaded areas correspond to the volume occupied by the original droplet mass.

For the higher shock Mach number cases as in Fig. 4.5, the deformation and disintegration of a drop no longer appear as distinct and separate stages of the breakup but occur almost simultaneously. Also the fact that the liquid material being continuously stripped from the surface of the drop is able to follow the streamline pattern of the wake indicates that this liquid must be in the form of a fine micro-mist. Further comments relative to this will be brought out in connection with the streak photographs.

Fig. 4.5. Shadow Photograph of 2700μ drop.
$M_s = 3.5$, $P_1 = 1$ atm, $t = 14\ \mu$sec after shock
passage.

BOW SHOCK

WAKE

$$\text{ELLIPSE:} \quad \frac{X^2}{16} + \frac{Y^2}{29} = 1$$
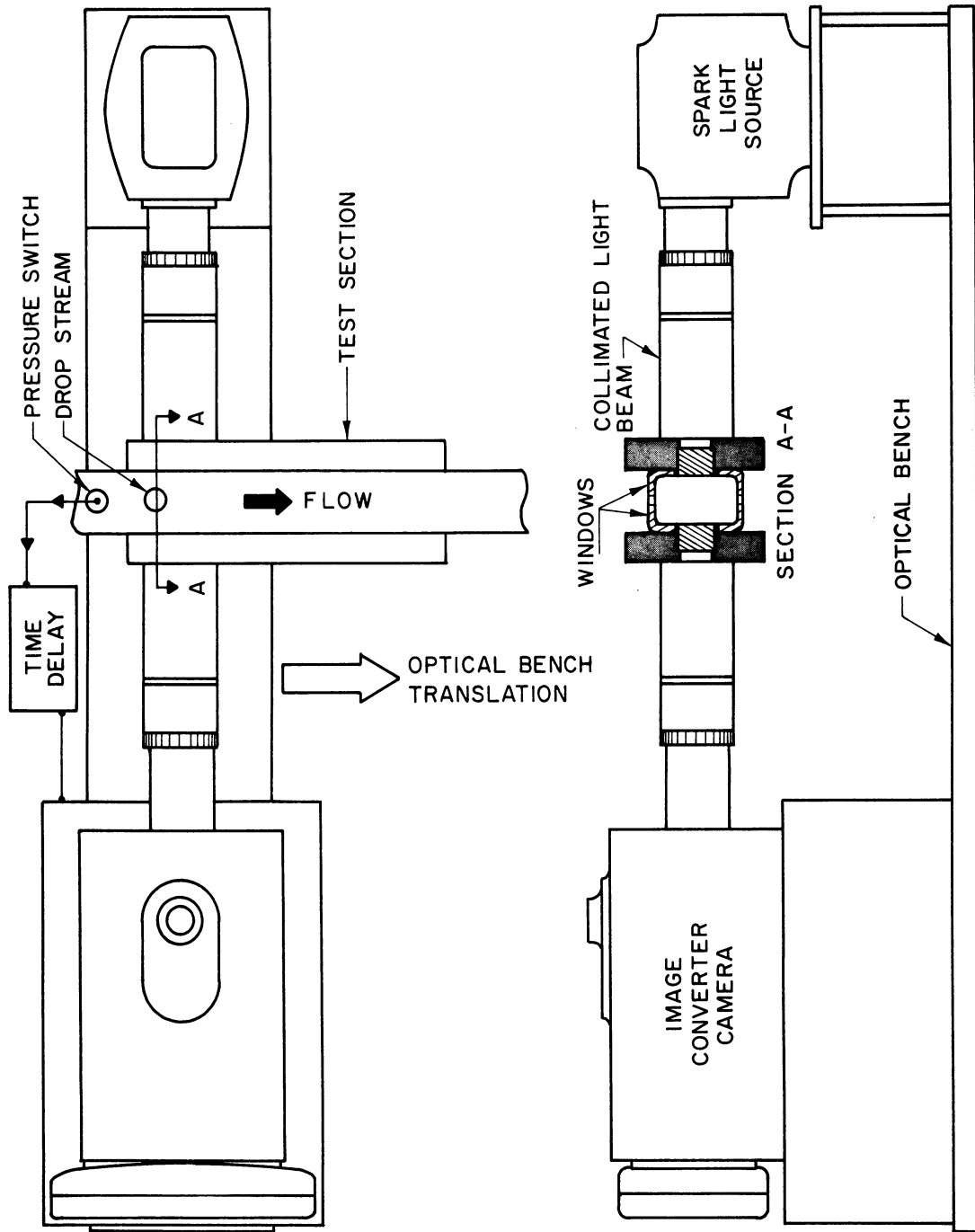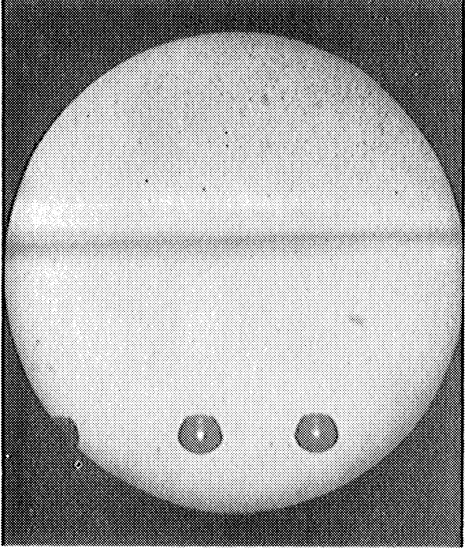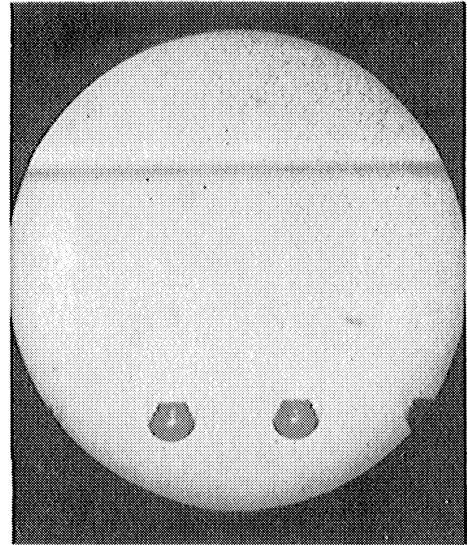
Fig. 4.6. Diagram of photograph in Fig. 4.5.

CROSS SECTION

PROFILE

59 μ-sec
14 μ-sec
0 μ-sec
26 μ-sec

U_2
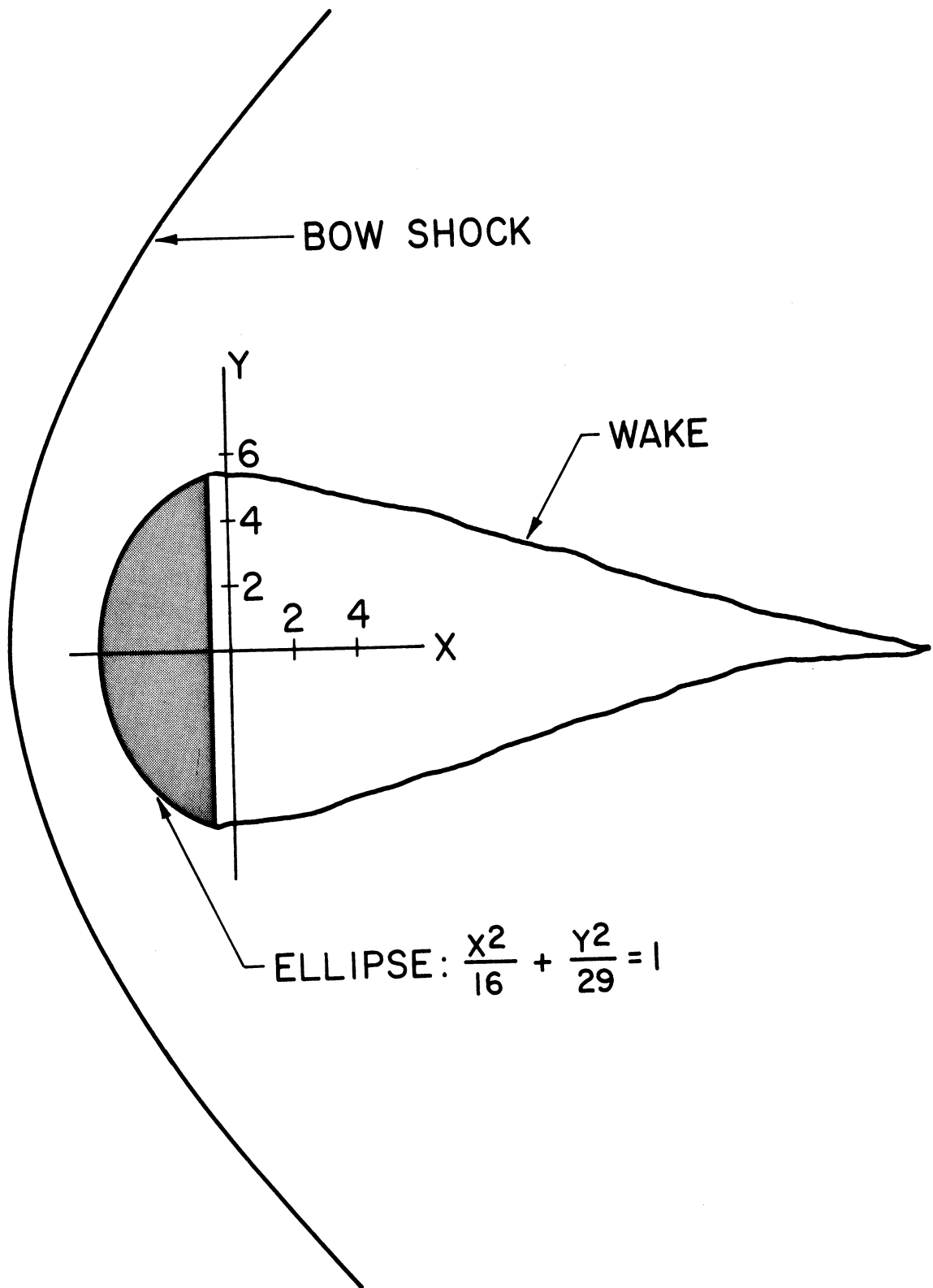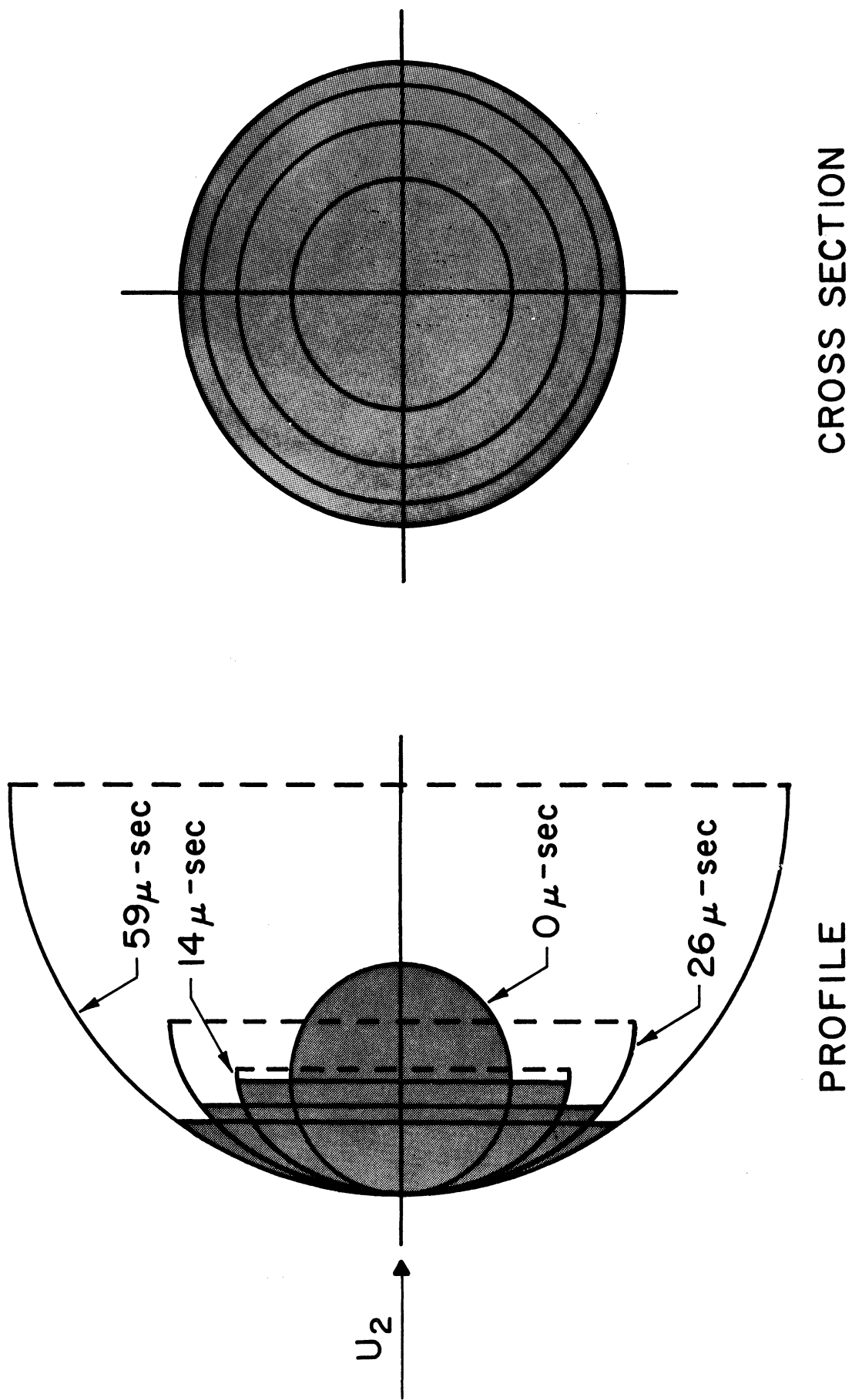
Fig. 4.7. Deformation of drop shown in Fig. 4.5.

70

The effect of shock Mach number on the rate of breakup and on the acceleration can be vividly seen in the streak photographs of Fig. 4.8 and 4.10. These two figures show the continuous displacement of an 1100μ drop as a function of time when the incident shock strength is, respectively, $M_s = 1.6$ and 2.5. Figures 4.9 and 4.11 are tracings of these photographs showing the displacement (x) and time (t) scales, the particle path, the drop trajectory, and the point (χ, τ) at which the local slope of the displacement curve is equal to 95% of the convective flow velocity, U_2, behind the shock front. Disintegration is seen to begin within several microseconds after the Mach 2.5 shock intercepts the drop whereas approximately 50 μsec elapse before stripping is apparent at the lower Mach number. It is inter-esting to note that in both cases the material which is initially removed from the drop surface is accelerated almost instantaneously to the particle ve-locity behind the wave front thus giving additional evidence of the small size of these particles. Since the convective flow is supersonic relative to the drop, one also notes the presence of a stand-off bow shock and several wake shocks when $M_s = 2.5$. Figure 4.12 gives a clear picture of the bow shock and the change in the stand-off distance with time as the drop is accelerated by the flow.

The variation of drop diameter and drop position as a function of time, as determined from the image converter photographs for a variety of experi-mental conditions, were shown in Ref. (3). The results indicated that the time required to reach an equivalent state of deformation decreases and the maximum diameter attained increases as the incident shock Mach number varied from $M_s = 1.3 - 3.5$ (other conditions the same).

The displacement data indicated fairly good agreement with a parabolic relation between distance and time during the initial phases of the breakup, but a departure from this relation in the latter phases. This indicated that initially the drop acceleration is reasonably con-stant but it does not remain so during the advanced portion of the

TIME

DISTANCE

DROP TRAJECTORY
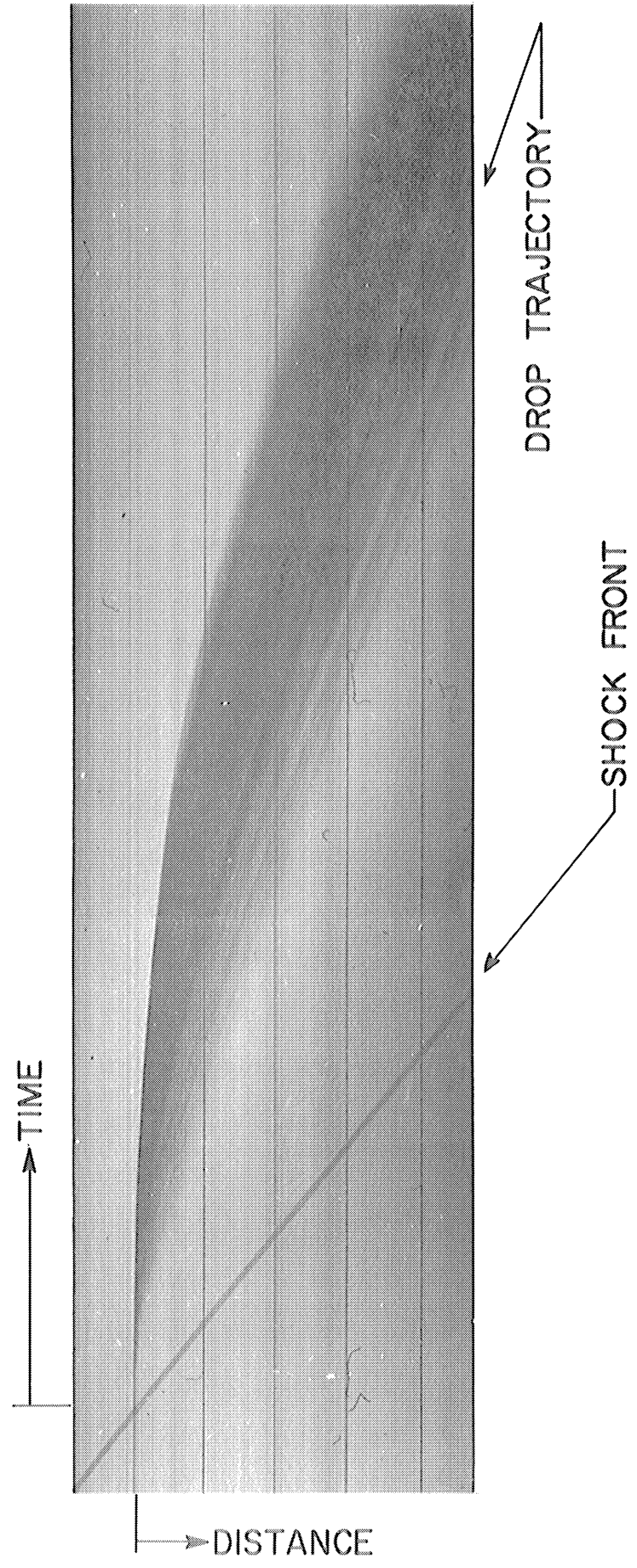
SHOCK FRONT

Fig. 4.8. Streak photograph of 1100μ drop, $M_s = 1.6$, $P_1 = 1$ atm.
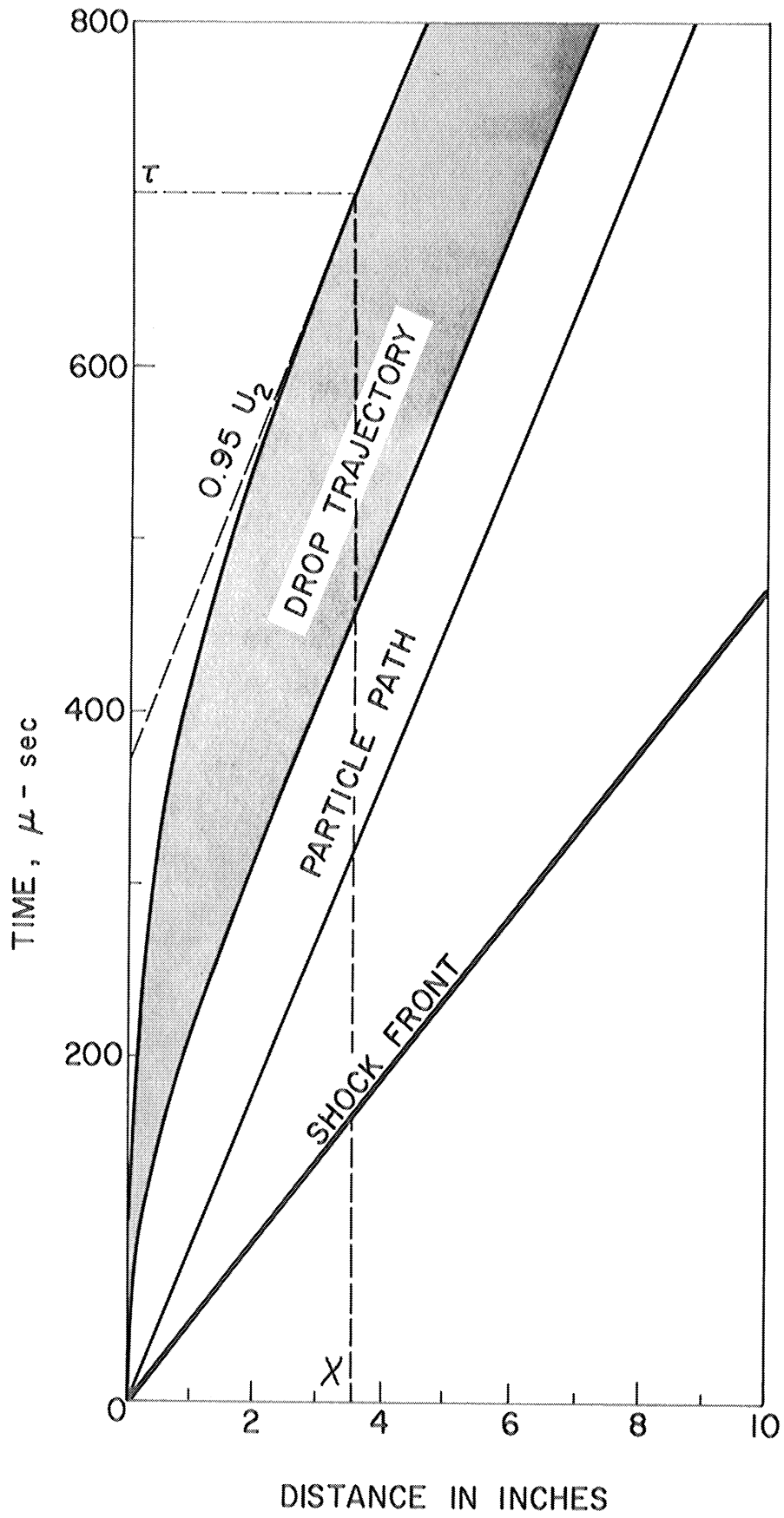
Fig. 4.9. Diagram of photograph in Fig. 4.8.

DROP TRAJECTORY

SHOCK FRONT

TIME

DISTANCE
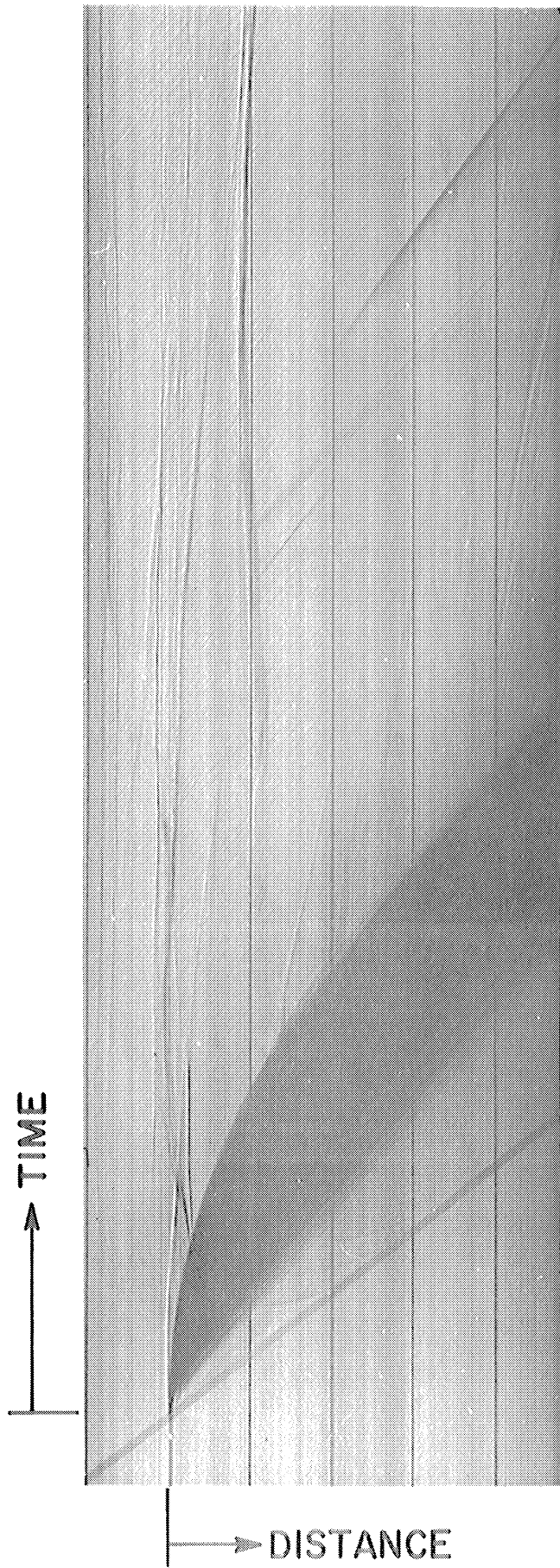
Fig. 4.10. Streak photograph of 1100μ drop, $M_s = 2.5$ $P_1 = 1$ atm.
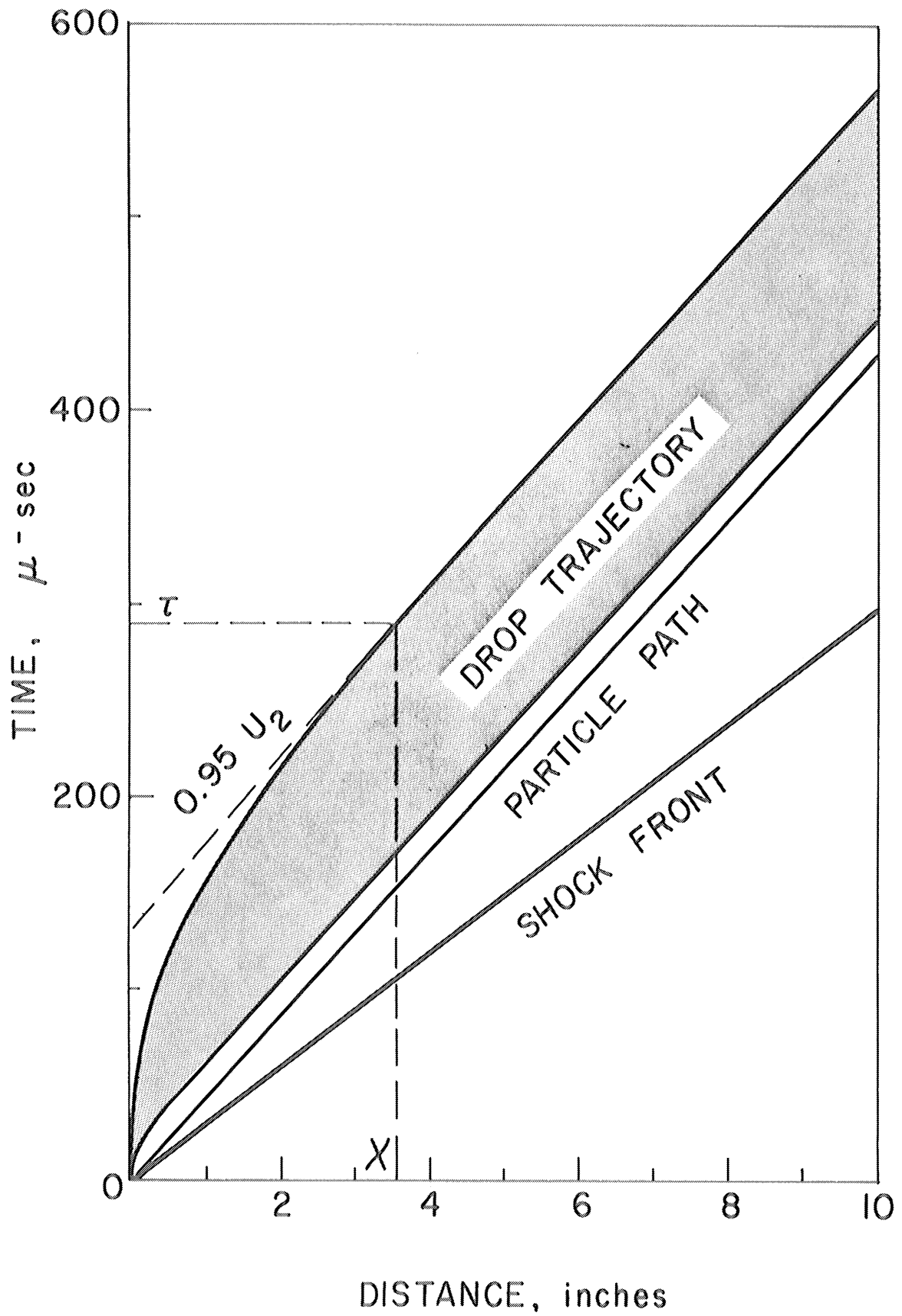
Fig. 4.11. Diagram of photograph in Fig. 4.10.
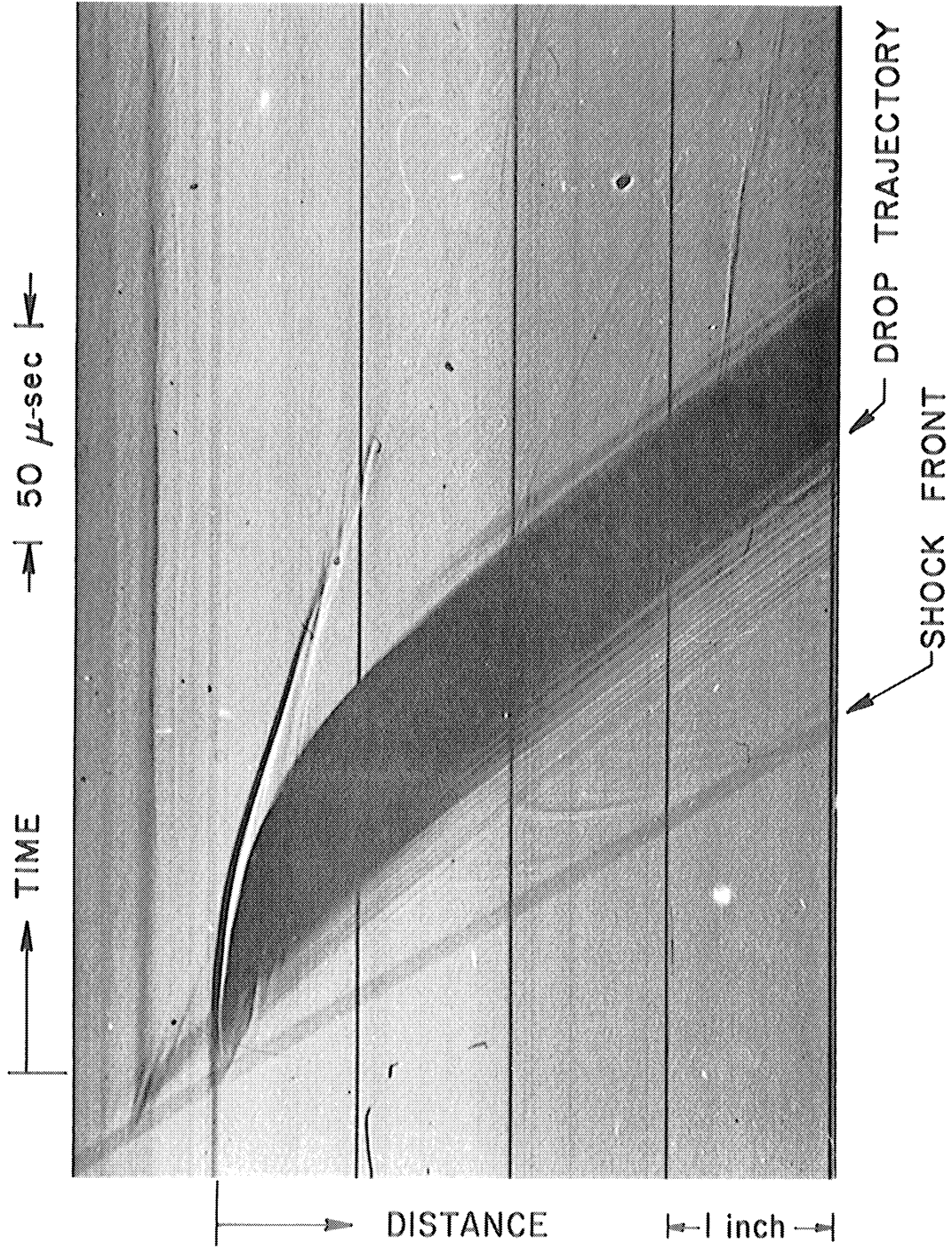
Fig. 4.12. Streak photograph of 1400μ drop, $M_s = 3.34$, $P_1 = 1$ atm.

breakup. Physically, this means that approximately midway through the breakup period the mass of a drop is decreasing at a rate faster than the drag forces are diminishing and the net effect is an increase in the drop acceleration.

In spite of the last qualification, it is interesting to consider the drop as a spherical particle of constant mass and then write the momentum equation, i.e.,

$$C_D \frac{1}{2} \rho_g U_r^2 S = ma$$

or,

$$a = \frac{3}{4} \frac{C_D}{D} \frac{\rho_g}{\rho_\ell} U_r^2 \qquad (4.1)$$

Now, assuming constant acceleration

$$x = \frac{1}{2} a t^2 = \frac{3}{8} \frac{C_D}{D} \frac{\rho_g}{\rho_\ell} U_r^2 t^2$$

or in dimensionless terms with C_D, D, and U_r evaluated at t = 0 (ρ_g and ρ_ℓ are invariant with t), we get

$$\overline{X} = \frac{3}{8} C_D \overline{T}^2 \qquad (4.2)$$

where $\overline{X} = x/D_o$ and $\overline{T} = \sqrt{\rho_g/\rho_\ell}\, U_2/D_o\, t = U_2\, t/D_o\, \beta^{-1/2}$.

The displacement data for a variety of drop sizes and shock strengths (including some data from Engel[10] and Nicholson[11]) are plotted against the non-dimensional variables with the result shown in Fig. 4.13. It is seen that all of the data collapses into the single parabola $\overline{X} = 1.1\,\overline{T}^2$, except for the data of Nicholson which better fits $\overline{X} = 0.714\,\overline{T}^2$. The constant of 1.1 implies a $C_D = 3$.
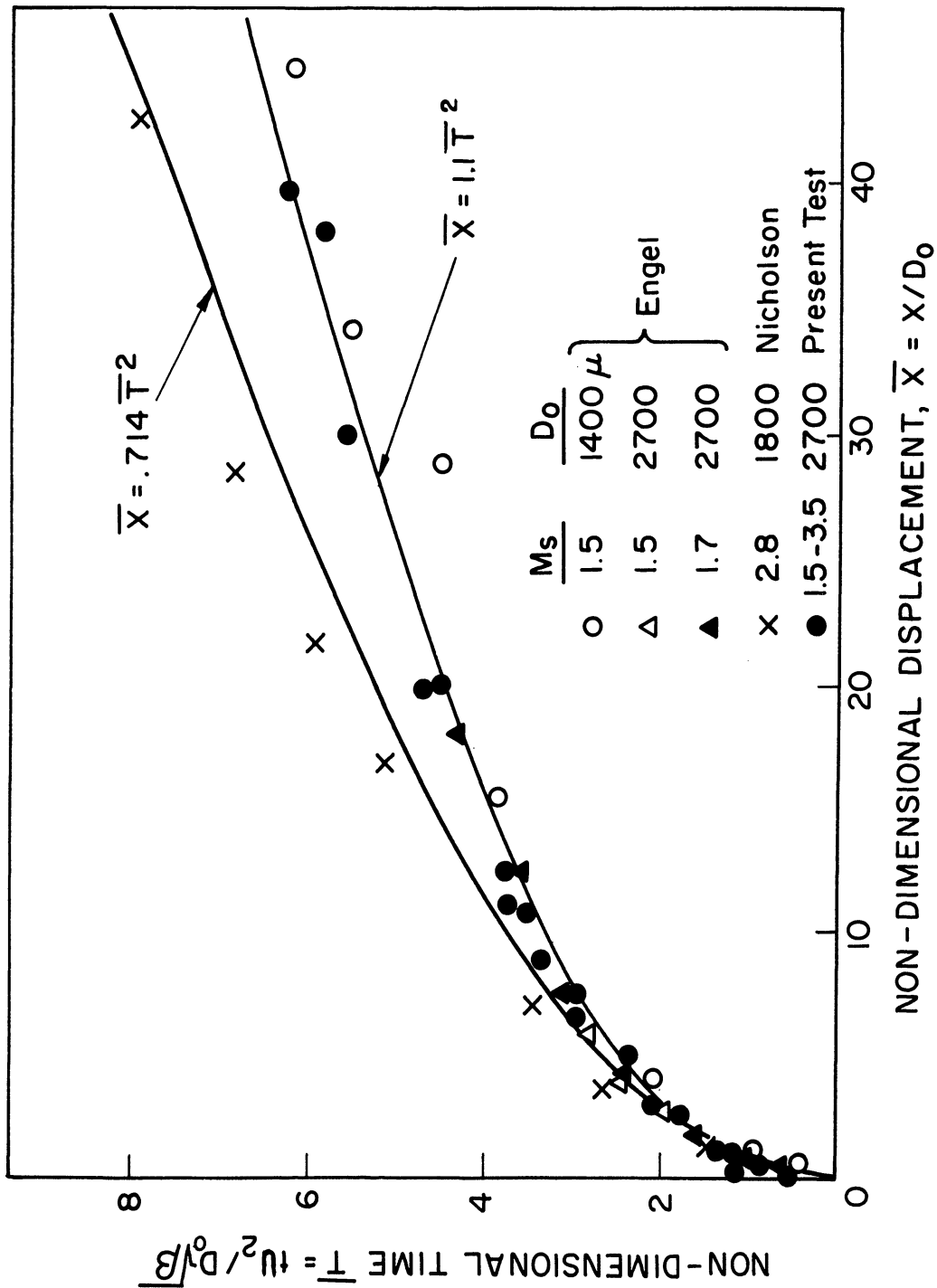
Fig. 4.13. Non-dimensional displacement vs. non-dimensional time.

In view of Eq. (4.2) it is interesting to examine some of the dynamics of drop shattering in terms of the dimensionless coordinates. Accordingly, the drop deformation data for a wide range of experimental conditions are shown in Fig. 4.14 as a function of $\overline{T}$. Although some scatter is evident, it is apparent that the deformation approximately obeys a two part linear variation wherein the maximum diameter is realized at about 30% of the breakup time.

The effect of incident shock strength on the time required to break up a drop of a given diameter for certain initial conditions was determined from image converter photographs. These results were presented earlier[3] along with similar results of other investigators. Other things being equal, the higher shock Mach numbers lead to much lower breakup times; for example, less than 100 μsec are required to completely disintegrate a 900μ drop at M_s = 3.5 whereas 360 μsec are required at M_s = 1.5 (P_1 = 1 atm). Of course, the real variable of importance is the dynamic pressure behind the shock. This influence has been pointed out by others and is certainly true of this work. In fact for most of the experimental conditions of this work it turns out that $t_b \propto q_2^{-1/2}$, approximately. This particular relationship can also be seen from the $\overline{X}$ - $\overline{T}$ correlation and the definition of $\overline{T}$. If the dimensionless breakup time, $\overline{T}_b$, is evaluated from the data it is found that, approximately, $\overline{T}_b$ = 5 (see Fig. 4.14). However, there is a M_s effect in that $\overline{T}_b$ varies from about 5 - 6 as M_s goes from 1.5 - 3.5. Using the value of 5, then $\overline{X}_b \cong 28$; that is to say, the drop displacement distance for breakup is about 28 diameters. A comparison between dimensionless breakup times can be made by rewriting Clark's[12] expression in terms of $\overline{T}$ to get $\overline{T}_b = \sqrt{\epsilon_b}$. Using a value of ϵ_b = 15, corresponding to complete breakup, one finds a $\overline{T}_b \simeq 4$ which is in reasonable agreement with the value evaluated from the present study.
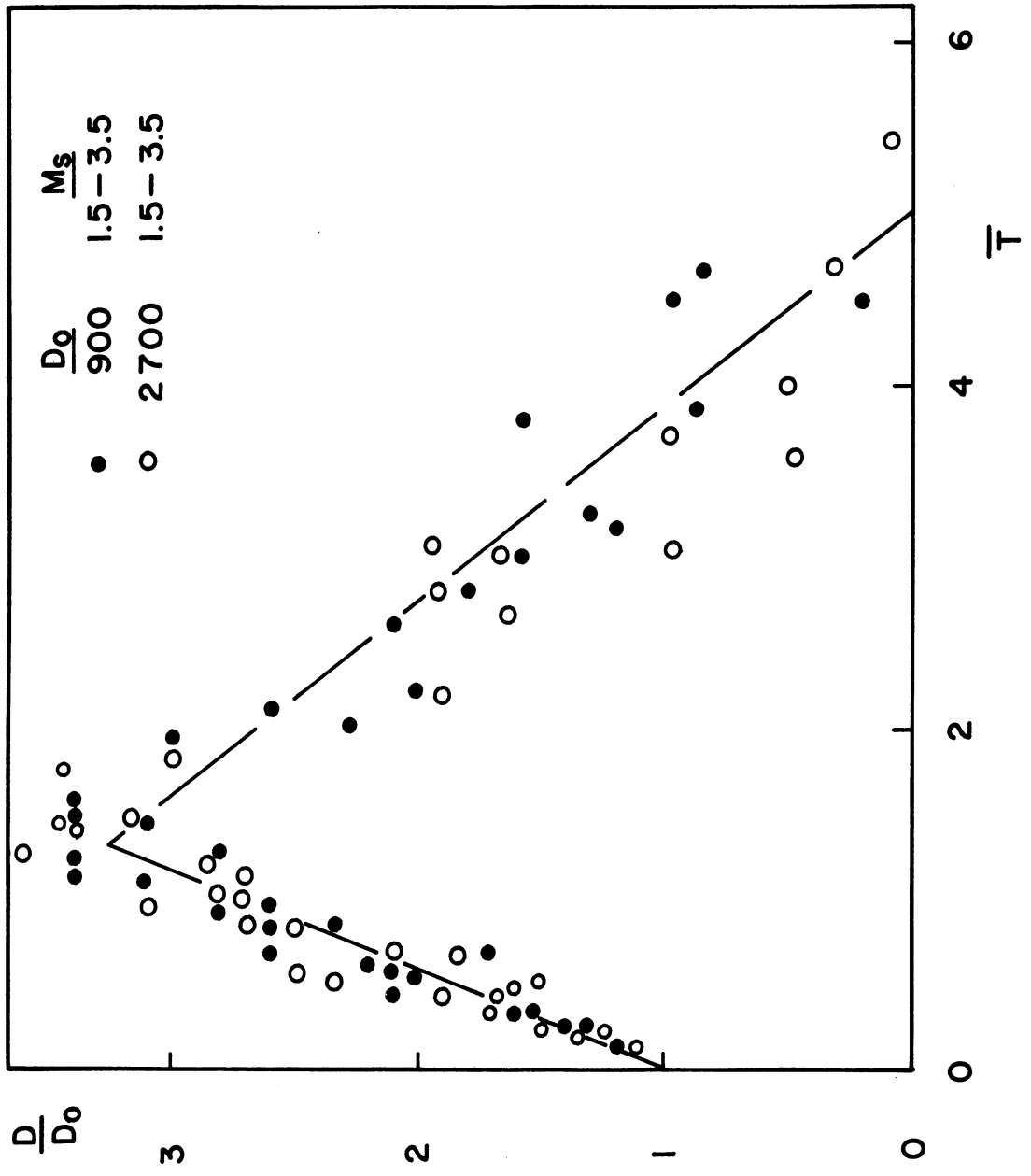
Fig. 4.14. Non-dimensional deformation vs. non-dimensional time.

Using, for the displacement, the relation $\overline{X} = 1.1\,\overline{T}^2$, the relative velocity between an accelerating drop and the convective flow behind the shock front can be computed. These computations are plotted versus $\overline{T}$ in Fig. 4.15 with the shock Mach number as a parameter. The computations are independent of D_o and assume air at $P_1 = 1$ atm. The results indicate that at breakup, when $\overline{T} \simeq 5$, the relative velocity diminishes to approximately 50% and 20% of its initial value when $M_s = 1.3$ and 3.5, respectively.

Figures 4.16-4.21 give results of the streak photography for drop sizes 1000-4000μ in diameter over a Mach number range $M_s = 1.52 - 3.34$. Figures 4.16, 4.18, and 4.20 are families of displacement curves taken from streak photographs of the breakup whereas Fig. 4.17, 4.19, and 4.21 show, respectively, these same displacements plotted in the non-dimensional coordinates $\overline{X}$ and $\overline{T}$. The remarkable feature of these dimensionless curves is their similarity and the influence on them of the convective flow Mach number, M_2. It is interesting to note that, up to the time when $\overline{T} \simeq 2$, no parametric dependence on Mach number is apparent, however, for $\overline{T} > 2$, a consistent effect is observed which is independent of the initial droplet size.

Figures 4.17, 4.19, and 4.21 show that, as the convective flow Mach number is increased from about $M_2 \simeq .6$ to $M_2 \simeq 1.0$, the dimensionless time required, for a drop to move a dimensionless distance $\overline{X} > 10$, increases significantly. For example, in Fig. 4.19 where $D_o = 1400\mu$, one notes that when $\overline{X} = 30$ and $M_2 = .62$ and .94 then $\overline{T} = 5.1$ and 5.9, respectively. It is also apparent that, instead of becoming more pronounced when M_2 exceeds Mach one, the effect of Mach number on the dimensionless droplet displacement history is decidedly less than it is near the sonic condition. For example, referring again to Fig. 4.19, we see that when $\overline{X} = 30$ and $M_2 = 1.44$ then $\overline{T} = 5.3$ whereas $\overline{T} = 5.9$ at $M_2 = 0.94$. This effect is clearly independent of initial drop size because it is preserved in the data presented in Fig. 4.17 and 4.21 for drop diameters ranging from 1000-4000μ.

When $\bar{X} = 1.1\,\bar{T}^2$, $P_1 = 1$ atm.

$M_s = 1.3$

$M_s = 2.0$

$M_s = 3.5$

$\left(1 - \dfrac{W}{U_2}\right)$
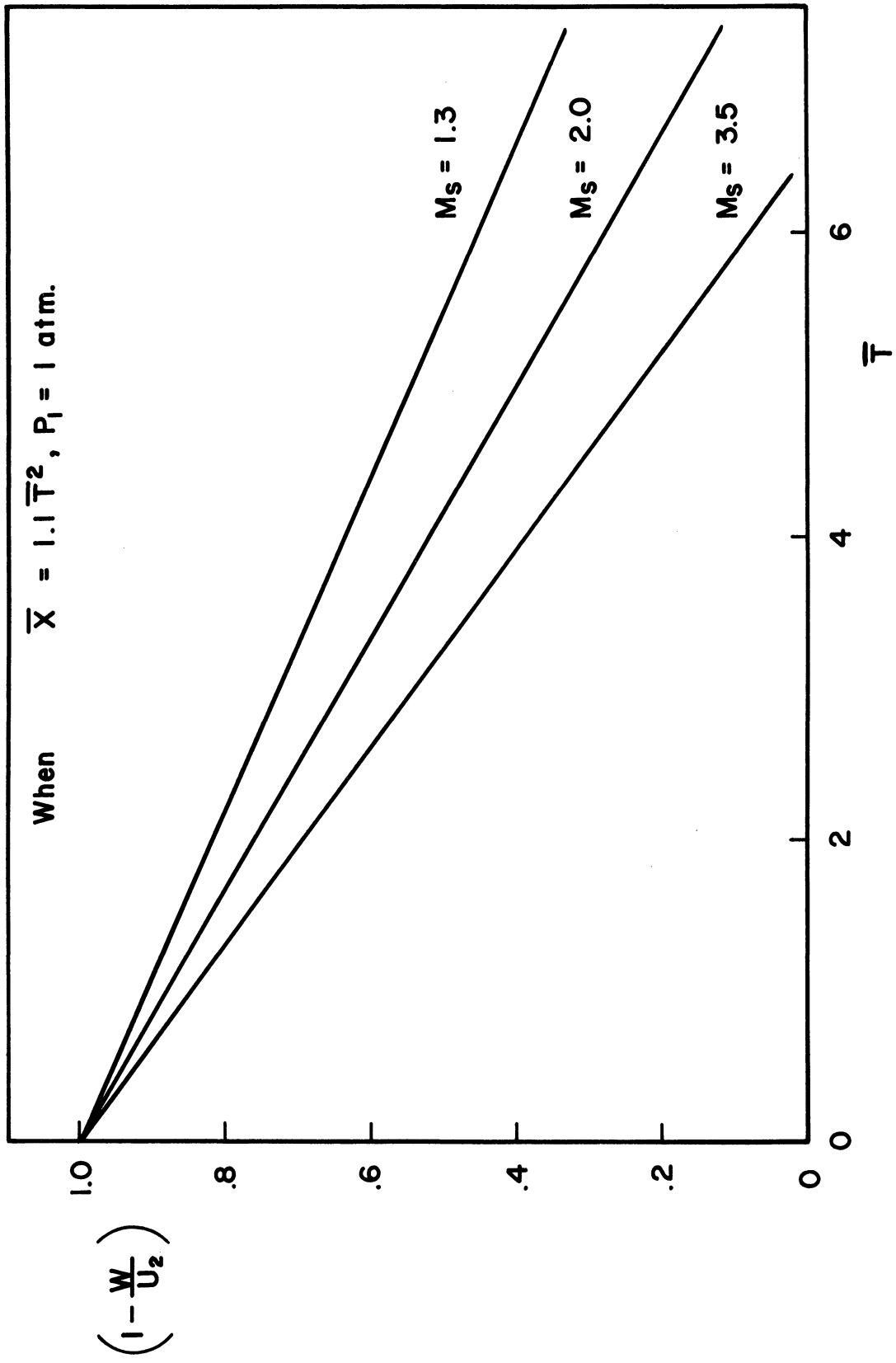
Fig. 4.15. Relative velocity vs. non-dimensional time.

Fig. 4.16. Displacement data obtained from streak films when $P_1 = 1$ atm.
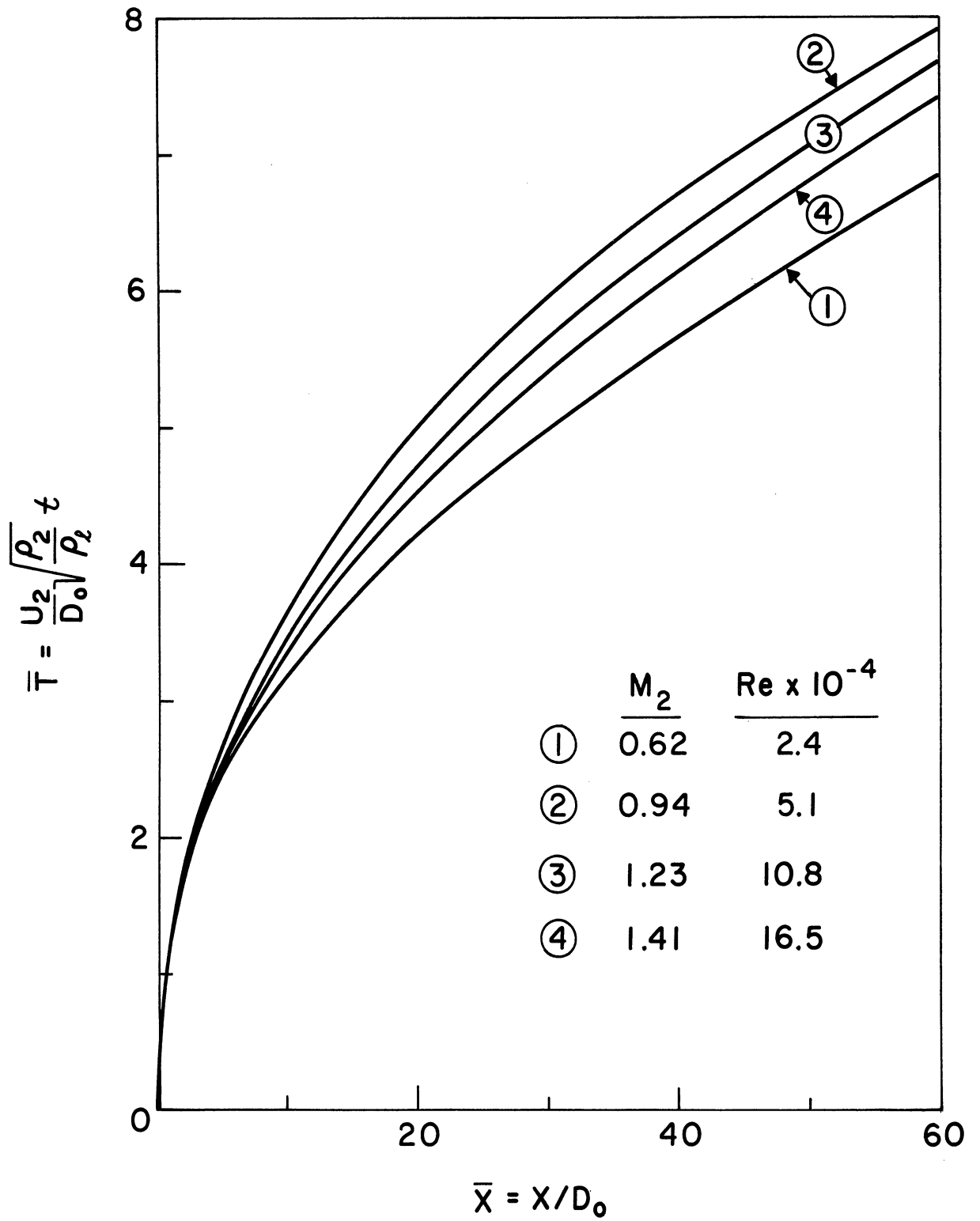
Fig. 4.17. Dimensionless plot of data contained in Fig. 4.16.
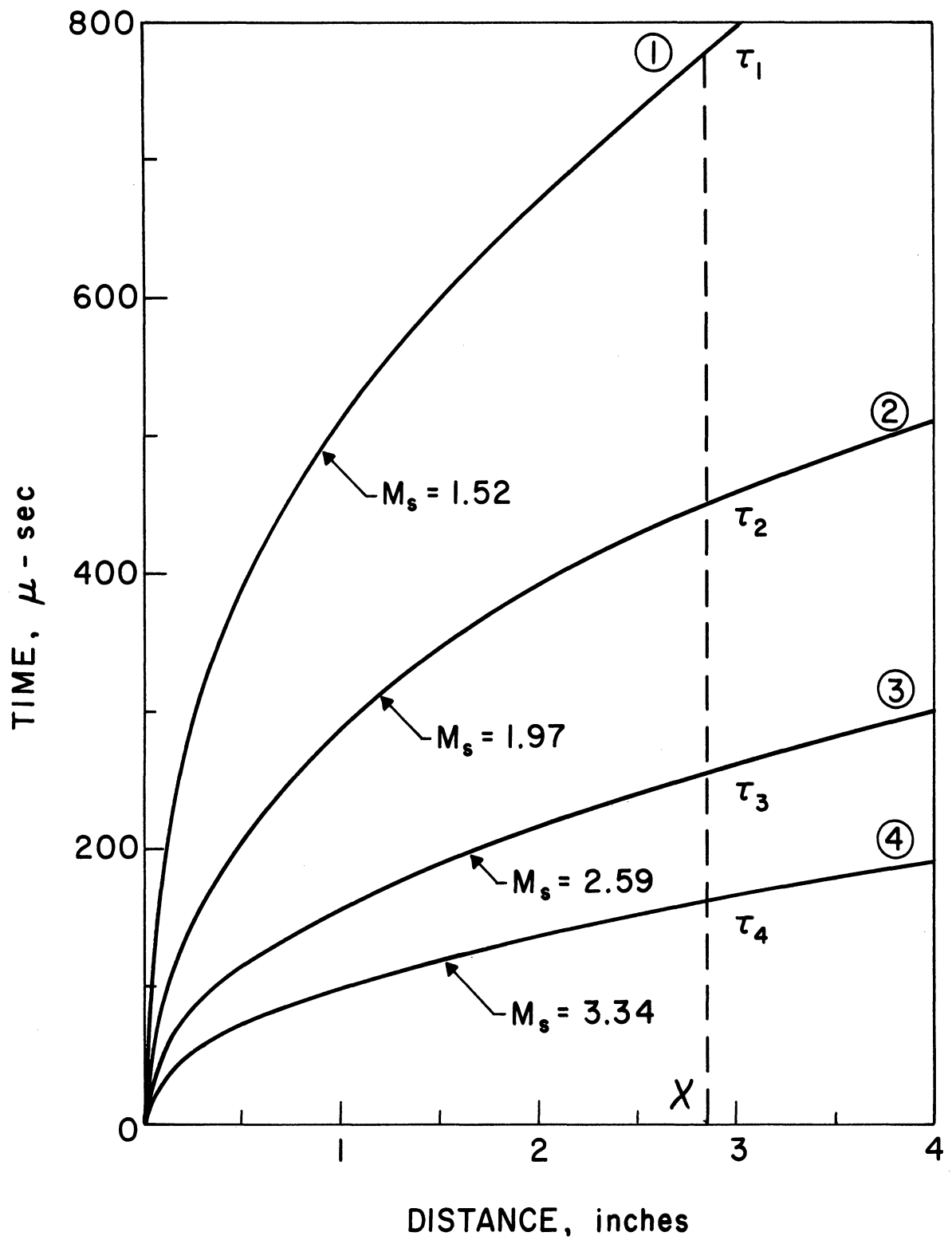
Fig. 4.18. Displacement data obtained from streak films of
1400μ drops when P_1 = 1 atm.
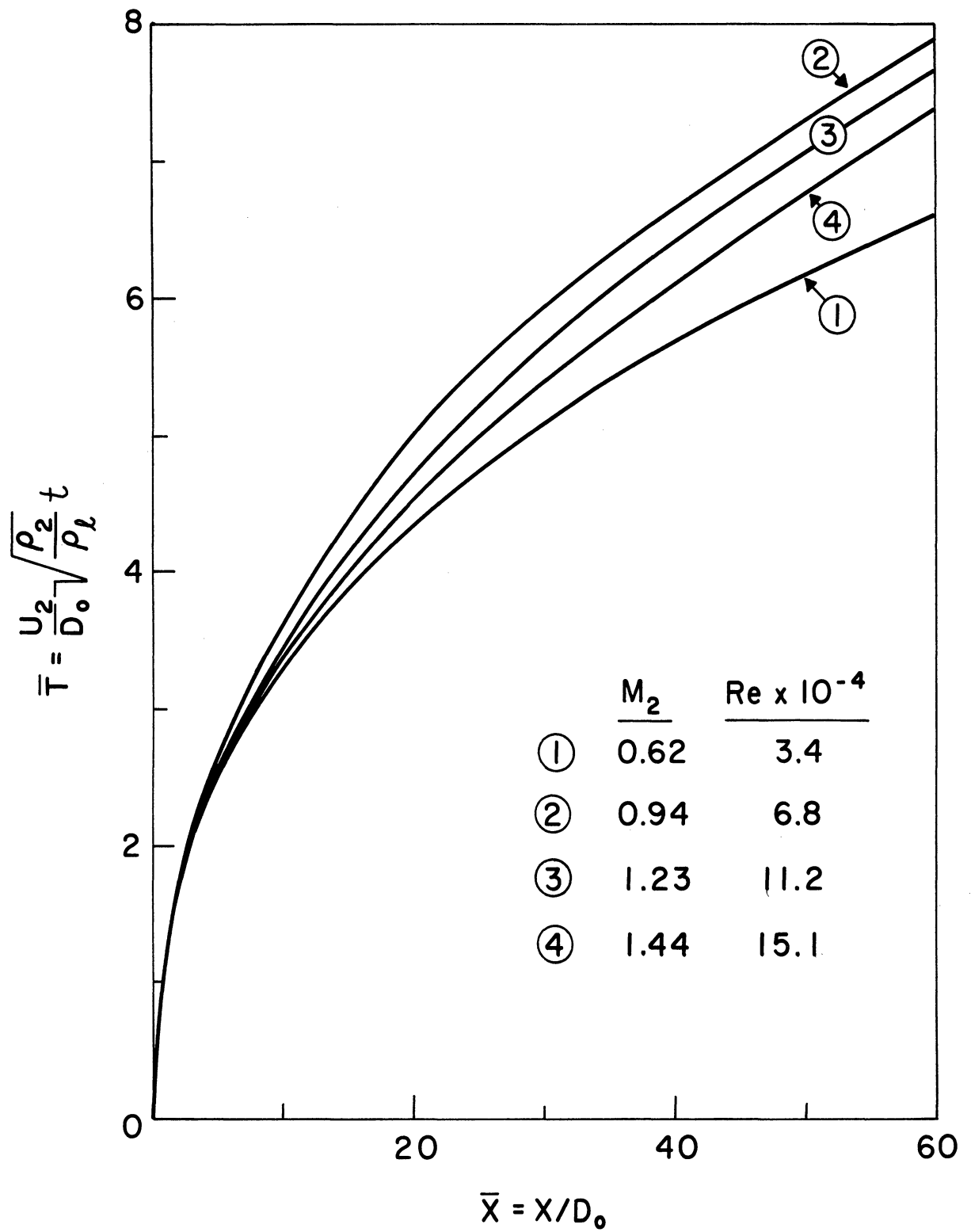
Fig. 4.19. Dimensionless plot of data contained in Fig. 4.18.
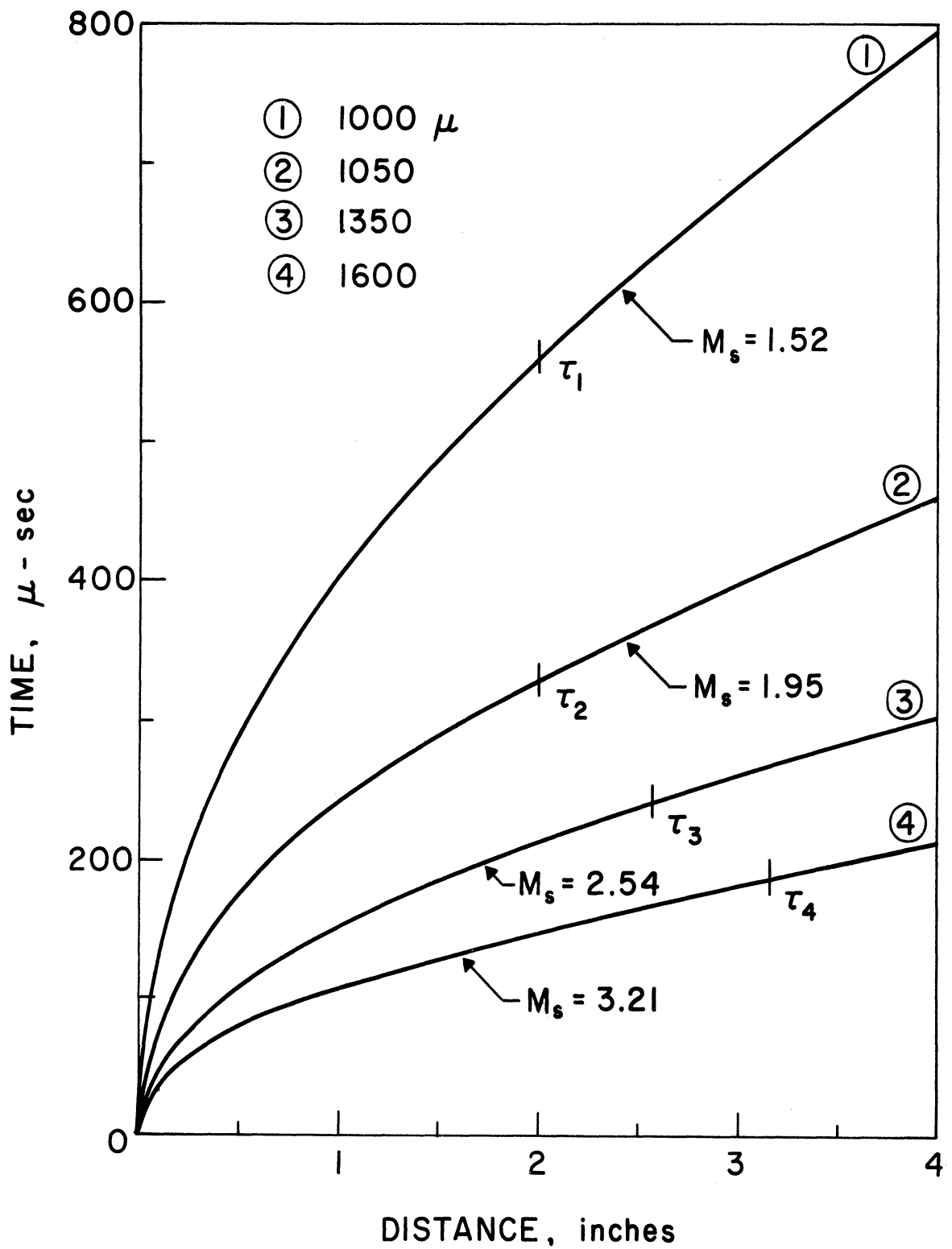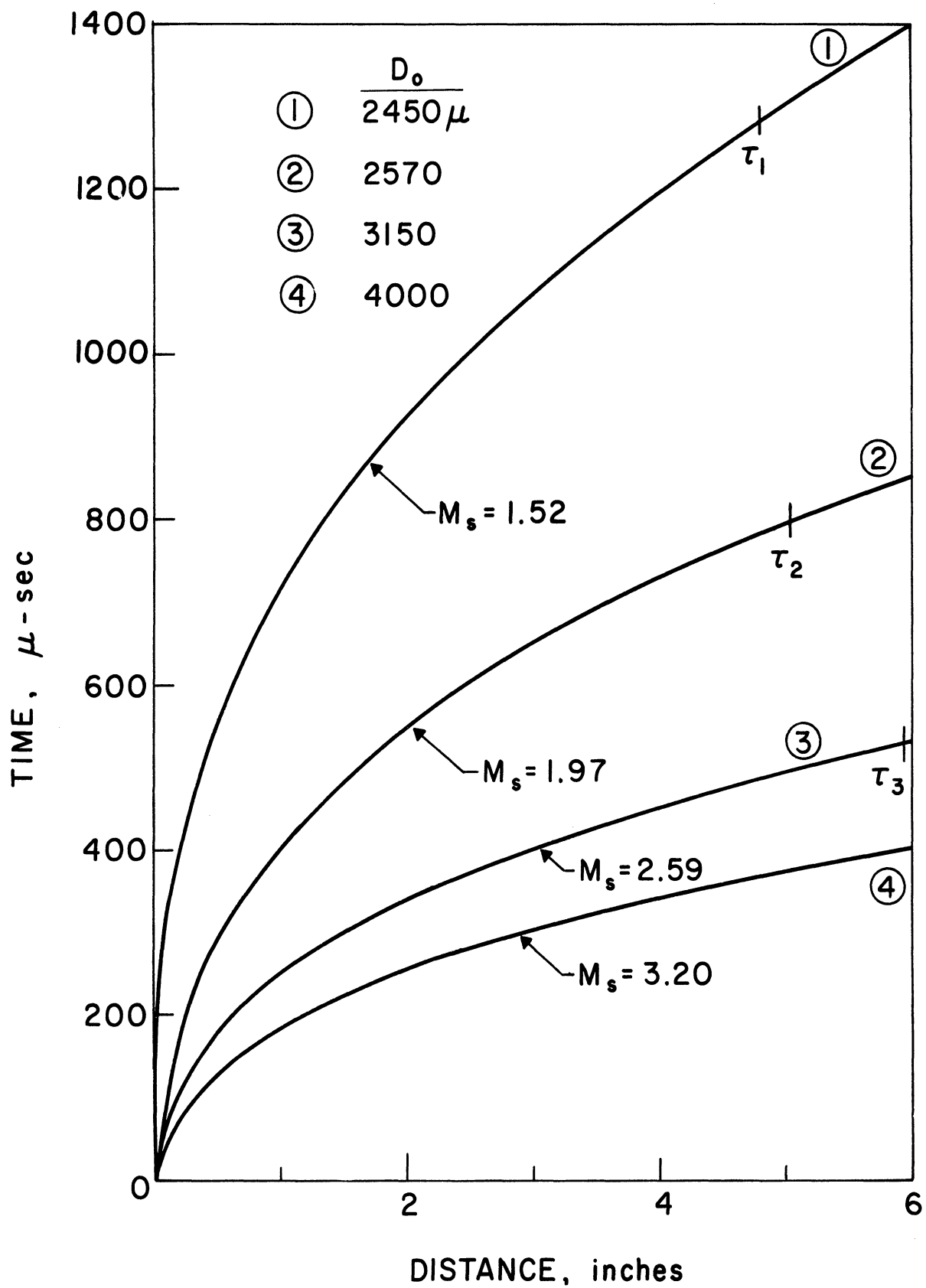
Fig. 4.20. Displacement data obtained from streak films when $P_1 = 1$ atm.

87
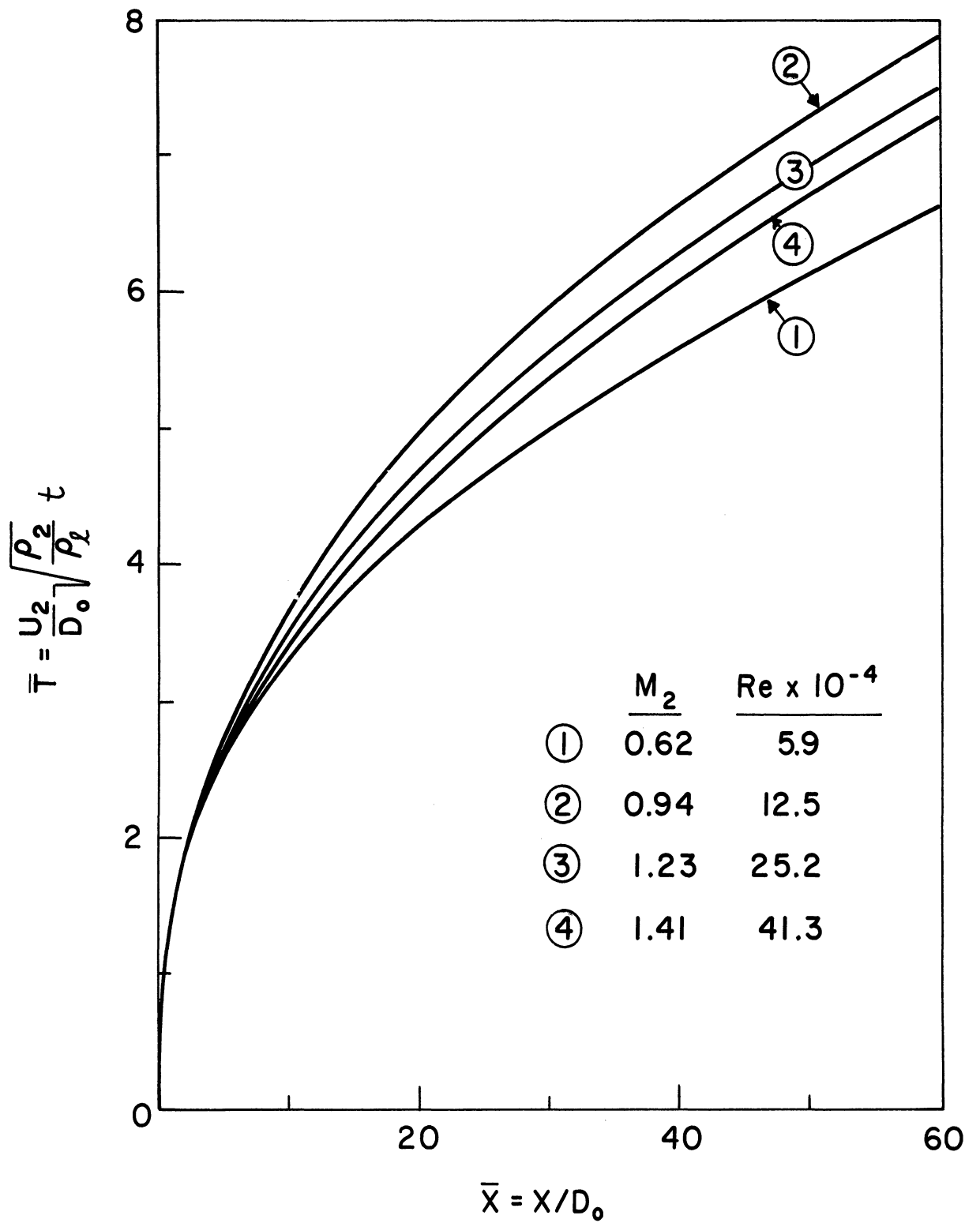
Fig. 4.21. Dimensionless plot of data contained in Fig. 4.20.

An adequate physical explanation, for the effect of Mach number on the dimensionless displacement of a droplet, is complicated by the complex nature of the shattering phenomenon. Not only is the drop shape changing rapidly with time, thus altering the external pressure field around it, but the surface is being simultaneously stripped away, consequently reducing its mass. Therefore, the coupled effects of a changing drag and a diminishing mass are manifest in the non-dimensional displacement history, and any hope of being able to separate the two, for the purpose of giving a satisfactory rational explanation to the Mach number effect, is very slight indeed.

The points at which the local slopes of the displacement curves are equal to 95% of the convective flow velocities behind the shock front are designated as (χ, τ) in Fig. 4.16, 4.18, and 4.20. Referring to Fig. 4.18, where $D_o = 1400\mu$, one sees that the time required, τ, to accelerate to this velocity, $.95 \ U_2$, decreases sharply from t = 770 μsec to t = 150 μsec as the shock strength is increased from $M_s = 1.52$ to $M_s = 3.34$, but that the distance, χ, at which this velocity is achieved is a constant and equal to $\chi = 2.8$ in. For larger drops this distance is greater than 2.8 in. and likewise, it is less for smaller ones as seen, respectively, in Fig. 4.20 and 4.16. The interesting element is that, although these distances depend on initial droplet size, the dimensionless distances, $\overline{\chi}$, are constant, independent of the initial diameter, and equal to $\overline{\chi} \cong 50$. The corresponding non-dimensional times, $\overline{\tau}$, vary somewhat depending on the magnitude of the convective flow Mach number. For example, in Fig. 4.17, when $M_2 = .62$ then $\overline{\tau} = 6.3$, however, with $M_2 = 1.41$, then $\overline{\tau} = 7.3$.

A comparison between the breakup times and distances determined from the individual image converter photographs and the distances (χ) and times (τ) obtained from the streak photographs is given in Table II.

Table II. Comparison of Displacement and Breakup Time Data

D_o μ	M_s	M_2	Image Converter t_b μsec	x_b in.	$\bar{\tau}$	$\bar{X}$	Streak Films τ μsec	X in.	$Re \times 10^{-4}$	$We \times 10^{-4}$	q_2 psia
1400	1.52	.62	704	1.96	6.22	51.3	777	2.84	3.4	0.12	9
	1.97	.94			7.38		450		6.8	0.66	48
	2.59	1.23			7.14		255		11.2	1.65	119
	3.34	1.44			6.83		162		15.1	3.78	274
1000	1.52	.62	357	1.8	6.3	50.7	557	2.00	2.4	0.09	9
	1.95	.94	219	1.3	7.38		326		5.1	0.47	48
1350	2.54	1.23			7.08	50.0	240	2.56	10.8	1.59	119
1600	3.21	1.41	115	1.64	6.8	50.0	185	3.17	16.5	3.97	252
2450	1.52	.62			6.14	50.0	1280	4.80	5.9	0.22	9
2570	1.97	.94	553	4.56	7.28	50.0	800	5.05	12.5	1.22	48
3150	2.59	1.23			6.91	50.0	528	5.94	25.2	3.70	119
4000	3.20	1.41			6.79	50.0	480	7.88	41.3	9.94	252

It shows, among other things, that the times and distances evaluated using the previously defined criterion defining χ and τ are in all cases longer than the breakup distances and times that were qualitatively determined from the individual pictures. In view of the fact that a drop is completely shattered by the time it is accelerated to $.95\ U_2$, this quantitative breakup criterion is adopted to replace the previously used qualitative one.

Several comparisons between the displacement data collected in the present study and the displacement histories reported by Nicholson and Engel are given, respectively, in Fig. 4.22 and 4.23. The generally good agreement between Nicholson's data and the streak data, displayed in Fig. 4.22, further substantiates the universality of the dimensionless displacement curves in Fig. 4.17, 4.19, and 4.21 because Nicholson's experiments, in contrast to those reported here, were conducted with various initial pressures in the driven section ranging from $1 \leq P_1 \leq 6$ psia. His data also reflect the same influence of Mach number on dimensionless displacement with the exception of when $M_2 = 1.32$. Instead of the effect being less pronounced at $M_2 = 1.32$, in accord with what has been found in this study, it is accentuated. This apparent deviation can be explained by the fact that Nicholson's data is reduced according to his assumed drop size rather than to a direct measurement of the diameter which, unfortunately, is unavailable.

Figure 4.23 makes two comparisons: one, between the displacement histories of Engel and the present study pieced together from a number of individual photographs; and two, between these pieced together histories and the streak photographs. The solid and dashed curves represent the streak data. From the figure, it is apparent that both sets of data compare favorably with one another, thus indicating that, in spite of the numerous inherent difficulties of collecting data points one at a time, it was accomplished with reasonable accuracy.
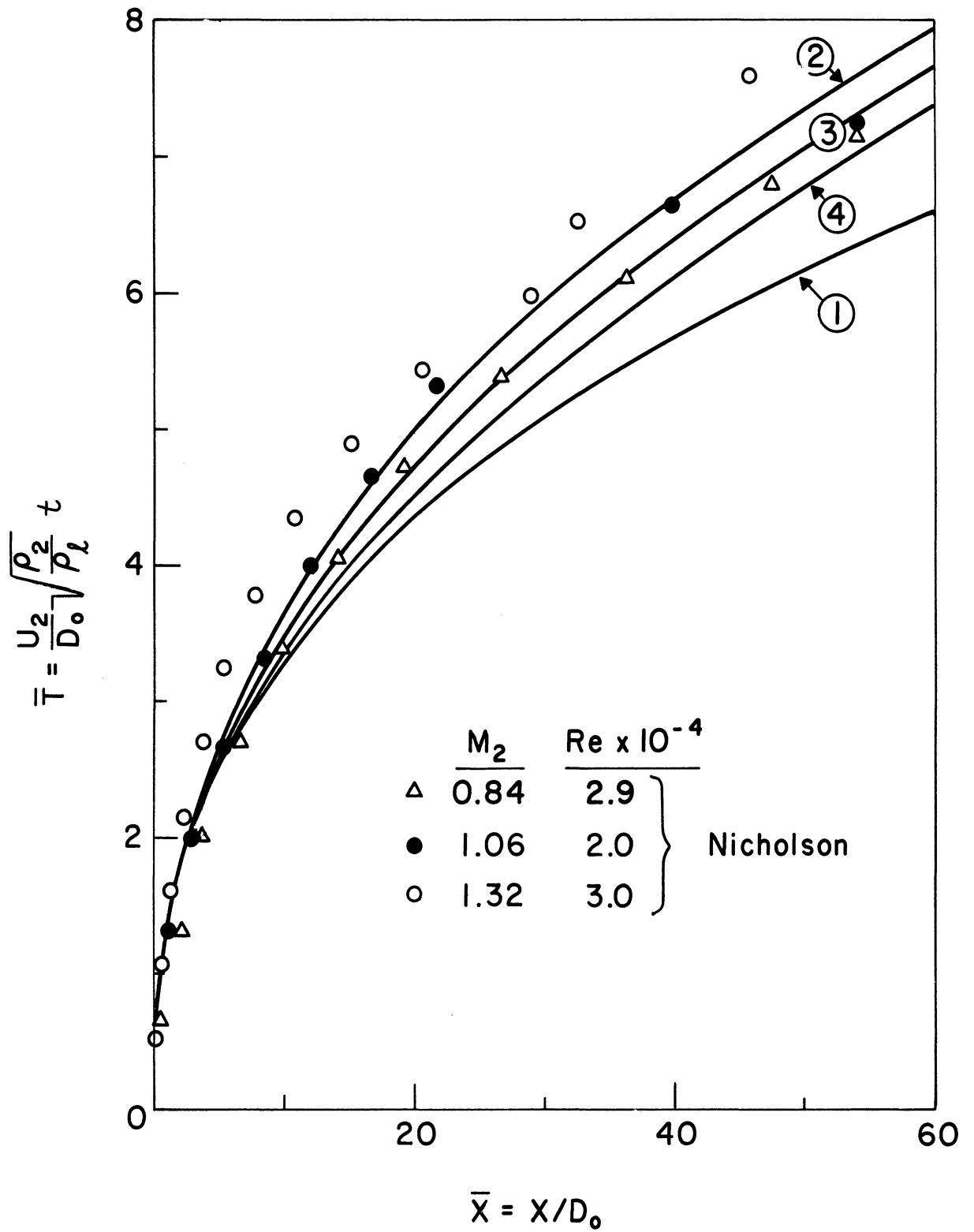
Fig. 4.22. A comparison between the streak data contained in Fig. 4.19 and the displacement data of Nicholson.
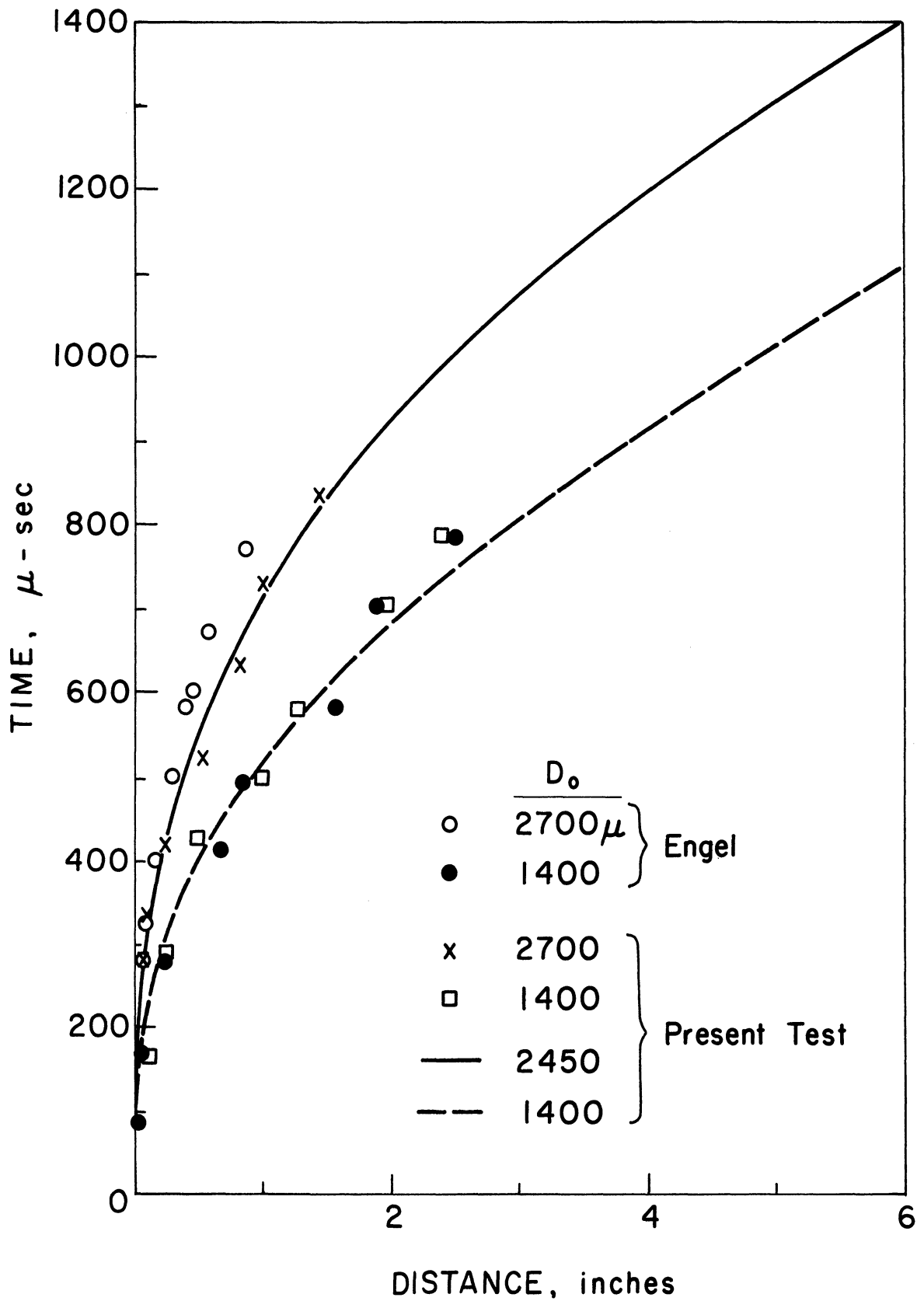
Fig. 4.23. A comparison between the displacement data of
Engel and the displacement data of the present tests for
$M_s = 1.5$, $P_1 = 1$ atm.

93

All of the data reported here is for a stream of liquid droplets where the center-to-center separation distance between adjacent ones is no less than four diameters. In order to establish whether or not the displacement of a single drop in the stream is affected by its neighbors, two sets of displacement tests were run. The separation distance was varied from four to ten diameters for both subsonic and supersonic convective flow conditions, and the results plotted in Fig. 4-24. The good agreement between the two sets of data indicates by comparison that even when the separation distance is four diameters the proximity effects are negligible. This is not a surprising result because, applying perfect fluid theory to the problem, one can show from calculations that the perturbation to the pressure distribution over the surface of a sphere is negligibly small when the center of a neighboring sphere is at least four diameters distant,

3. Boundary Layer Stripping Analysis

It is apparent from the photographs that the collision between the incident shock and the drop has little if any effect on the shattering phenomenon and thus breakup occurs as a result of the interaction between a drop and the convective flow field established by the shock. Therefore in formulating a model for shock wave-drop interaction, one can neglect the shock altogether and treat the problem simply as a droplet in a high speed flow. The shearing action exerted by the high speed gas stream on the drop periphery causes the formation of a boundary layer in the surface of the liquid. Calculations indicate that this layer can be established very rapidly after a drop is intercepted by a shock and the photographs show it being stripped away from the equator.

On the basis of these experimental observations, an approximate model is formulated for the breakup phenomenon by considering that disintegration results from a boundary layer stripping mechanism. The rate of disintegration is found by integrating over the thickness of the liquid boundary layer
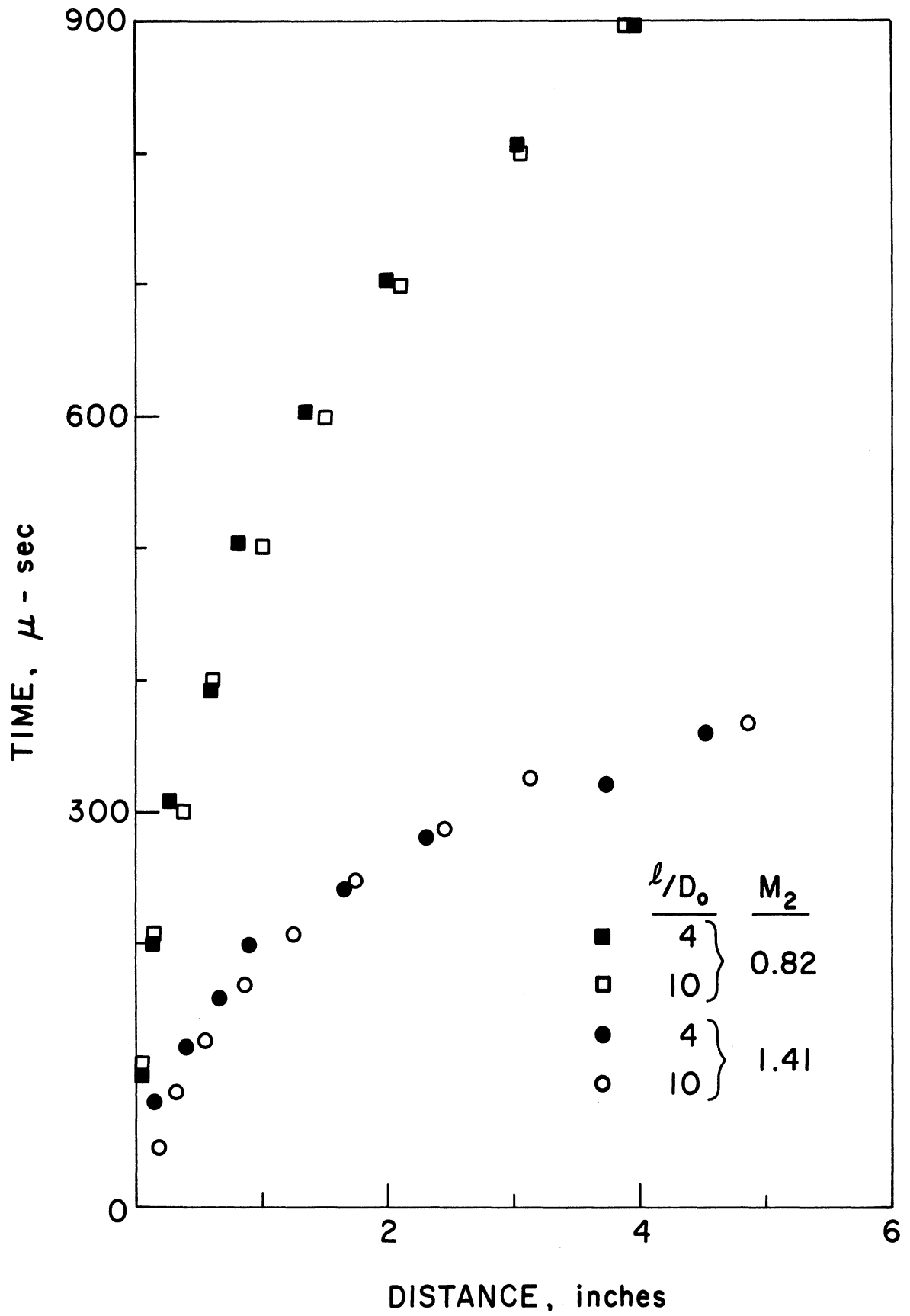
Fig. 4.24. The displacement of 3000μ drops when $P_1 = 1$ atm.

to determine the mass flux in the layer and by assuming that this flux leaves the surface of the drop at its equator. In order to evaluate the mass flux, we utilize a form of analysis attributable to G. I. Taylor[21] and similar to that used by Morrell[22] in his study of jet breakup.

Consider, therefore, the sudden exposure of a liquid drop to a high speed gas stream. Boundary layers will form in each as shown in Fig. 4. 25 where x is the curvilinear coordinate along the interface separating the two fluids, y is the coordinate perpendicular to it and r is the perpendicular distance from the axis of symmetry to the origin of the coordinate system. To calculate the exact form of these boundary layers, it would be necessary to go through a form of analysis similar to but more complicated than that of Blasius and therefore an approximate solution is sought. A reasonably accurate approximate solution to the two-boundary-layer problem can be obtained by assuming arbitrary simple velocity distributions containing a few parameters and then using the momentum integral relations to determine those parameters.

If we assume that the flow is axisymmetric, steady, and incompressible, then the boundary layer momentum integral equation is

$$\frac{\partial}{\partial x} \int_0^\infty u\,(U - u)\,dy + \frac{dU}{dx} \int_0^\infty (U - u)\,dy + \frac{1}{r}\frac{dr}{dx} \int_0^\infty u\,(U - u)\,dy = \frac{\tau_o}{\rho} \quad (4.3)$$

where

$$\tau_o = \mu \frac{\partial u}{\partial y}\Big|_{y=0}$$

From Eq. (4. 3), we have for the gas boundary layer

$$\frac{\partial}{\partial x} \int_0^\infty u_g\,(U - u_g)\,dy + \frac{dU}{dx} \int_0^\infty (U - u_g)\,dy + \frac{1}{r}\frac{dr}{dx} \int_0^\infty u_g\,(U - u_g)\,dy = \nu_g\left(\frac{\partial u_g}{\partial y}\right)_{y=0}$$

$$(4.4)$$

BOUNDARY LAYER STRIPPING ANALYSIS

$$\frac{u_g}{U} = 1 - (1-A)\exp\left\{\frac{-y}{\alpha_g \sqrt{x}}\right\}$$

$$\frac{u_\ell}{U} = A\exp\left\{\frac{-y}{\alpha_\ell \sqrt{x}}\right\}$$
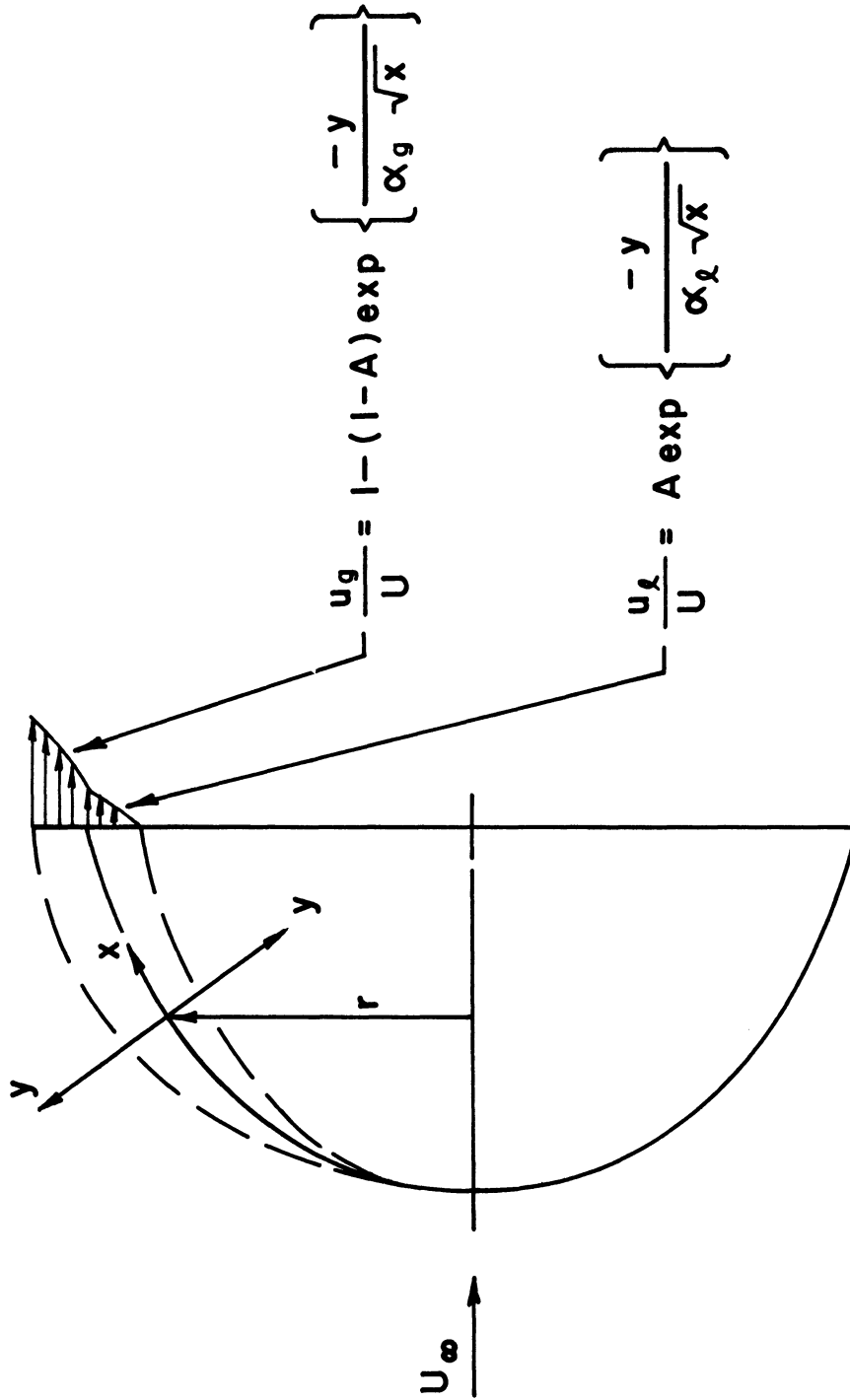
Fig. 4.25. Curvilinear coordinate system for boundary layer stripping analysis.

97

and for the liquid

$$\frac{\partial}{\partial x} \int_0^\infty u_\ell^{\,2} \, dy + \frac{1}{r} \frac{dr}{dx} \int_0^\infty u_\ell^{\,2} \, dy = - \nu_\ell \left(\frac{\partial u_\ell}{\partial y} \right)_{y=0} - \frac{1}{\rho_\ell} \frac{dp}{dx} \delta_\ell \qquad (4.5)$$

where the pressure gradient in the liquid layer is given by dp/dx

= - ρ_g U (dU/dx). Equating the shear stress in the gas layer to that in the liquid layer at the interface yields a third equation

$$- \rho_\ell \, \nu_\ell \left(\frac{\partial u_\ell}{\partial y} \right)_{y=0} = \rho_g \, \nu_g \left(\frac{\partial u_g}{\partial y} \right)_{y=0} \qquad (4.6)$$

To obtain approximate results, it is sufficient to assume arbitrary forms for u_g and u_ℓ and to assume that the drop shape, which is actually ellipsoidal, can be approximated by a sphere. Therefore, we have

$$U(x) = \frac{3}{2} U_\infty \sin \, (x/R) \qquad (4.7)$$

which is the ideal potential velocity distribution over the surface of a sphere, and

$$r(x) = R \sin \, (x/R) \qquad (4.8)$$

The velocity distributions in the liquid and gas layers are given respectively by the simplified but convenient expressions from Taylor; i.e.

$$\frac{u_\ell}{U} = A \, \exp \left(\frac{-y}{\alpha_\ell \sqrt{x}} \right)$$

$$\qquad (4.9)$$

$$\frac{u_g}{U} = 1 - (1 - A) \, \exp \left(\frac{-y}{\alpha_g \sqrt{x}} \right)$$

where A is the dimensionless velocity at the interface. These distributions satisfy the limiting boundary conditions that

$$\lim_{\substack{y \to \infty \\ x = \text{const}}} u_\ell = 0 \qquad\qquad \lim_{\substack{y \to \infty \\ x = \text{const}}} u_g = U(x)$$

$$\lim_{\substack{y \to 0 \\ x = \text{const}}} u_\ell = AU(x) \qquad\qquad \lim_{\substack{y \to 0 \\ x = \text{const}}} u_g = AU(x)$$

Applying Eq. (4.7 - 4.9) to (4.4-4.6), we obtain the three simultaneous equations

$$\frac{3}{8}(1 + A)\left[\sin(x/R) + 6\left(\frac{x}{R}\right)\cos(x/R)\right] + \frac{3}{2}\frac{x}{R}\cos(x/R) = \frac{\nu_g}{\alpha_g^2 U_\infty} \qquad (4.10)$$

$$\frac{3}{8}A\left[\sin(x/R) + 6\left(\frac{x}{R}\right)\cos(x/R)\right] = \frac{\nu_\ell}{\alpha_\ell^2 U_\infty} + \frac{3}{2}\left(\frac{\rho_g}{\rho_\ell}\right)\frac{\delta_\ell}{\alpha_\ell A \sqrt{x}}\left(\frac{x}{R}\right)\cos(x/R) \qquad (4.11)$$

$$\rho_\ell \nu_\ell \frac{A}{\alpha_\ell} = \rho_g \nu_g \frac{(1 - A)}{\alpha_g} \qquad (4.12)$$

which simplify respectively to,

$$\frac{3}{8} U_\infty (1 + A) \alpha_g = \frac{\nu_g}{\alpha_g} \qquad (4.13)$$

$$\frac{3}{8} U_\infty A \alpha_\ell = \frac{\nu_\ell}{\alpha_\ell} \qquad (4.14)$$

$$\rho_\ell \nu_\ell \frac{A}{\alpha_\ell} = \rho_g \nu_g \frac{(1 - A)}{\alpha_g} \qquad (4.15)$$

at the equator of a sphere; i.e., at $(x/R) = \pi/2$. From Eq.(4.14) we find

$$\alpha_\ell = \left[\frac{8}{3}\frac{\nu_\ell}{A U_\infty}\right]^{1/2} \tag{4.16}$$

and from Eq. (4.15)

$$\alpha_g = \alpha_\ell \frac{\rho_g}{\rho_\ell}\frac{\nu_g}{\nu_\ell}\frac{(1-A)}{A} \tag{4.17}$$

which when substituted into Eq. (4.13) gives

$$\left[1 - \left(\frac{\rho_\ell}{\rho_g}\right)^2\left(\frac{\nu_\ell}{\nu_g}\right)\right]A^3 - A^2 - A + 1 = 0 \tag{4.18}$$

Since A must be small compared to unity, one observes from Eq. (4.18) that A^3 must be of the order $(\rho_g/\rho_\ell)^2 (\nu_g/\nu_\ell)$. Therefore we put

$$A = \left(\frac{\rho_g}{\rho_\ell}\right)^{2/3}\left(\frac{\nu_g}{\nu_\ell}\right)^{1/3} \tag{4.19}$$

The mass of fluid in the circumferential liquid layer being swept along by the gas stream at a distance $x = \pi D/4$ from the stagnation point is

$$\frac{dm}{dt} = \pi D \rho_\ell \int_0^\infty u_\ell \, dy = \frac{3}{4}(\pi D)^{3/2} \rho_\ell A \alpha_\ell U_\infty \tag{4.20}$$

Substituting for A and α_ℓ and replacing U_∞ by the relative velocity, Eq. (4.20) becomes

$$\frac{dm}{dt} = \sqrt{\frac{3}{2}\pi^3}\left(\frac{\rho_g}{\rho_\ell}\right)^{1/3}\left(\frac{\nu_g}{\nu_\ell}\right)^{1/6}\left(\rho_\ell \nu_\ell^{1/2} U_2^{1/2} D_o^{3/2}\right)\left(\frac{D}{D_o}\right)^{3/2}\left(1 - \frac{W}{U_2}\right)^{1/2} \tag{4.21}$$

Therefore, the total mass stripped away during a period equal to $\overline{T}$ is found by integrating Eq. (4.21) with respect to time to obtain

$$\frac{m}{m_o} = 3\sqrt{6\pi} \left(\frac{\rho_g}{\rho_\ell}\right)^{1/6} \left(\frac{\mu_\ell}{\mu_g}\right)^{1/3} Re^{-1/2} \int_0^{\overline{T}} \left(\frac{D}{D_o}\right)^{3/2} \left(1 - \frac{W}{U_2}\right)^{1/2} d\overline{T} \qquad (4.22)$$

where m_o is the initial mass of the drop. For complete breakup the left hand side will be unity and the integration will extend to $\overline{T}_b$. In the absence of an analytical solution for the detailed dynamics of the drop, the integrand cannot be evaluated. Now for different drop sizes and flow conditions and noting that $(\rho_g/\rho_\ell)^{1/6} (\mu_\ell/\mu_g)^{1/3}$ is a weak function, we see that the integral must be a function of Re.

A preliminary check on the validity of the boundary layer stripping model may be obtained by borrowing from the experimental data. Thus, setting $\overline{T}_b = 5$ and using the distributions for D/D_o and $1 - W/U_2$ shown in Fig. 4.14 and 4.15, one can calculate the total amount of mass removed. For the case $D_o = 900\mu$ and $M_s = 1.5$ one gets $m/m_o = 1.1$. For the case $D_o = 2700\mu$ and $M_s = 2.1$ one gets $m/m_o = 0.64$. In view of the approximate nature of the analysis, the use of approximate relations for the experimental data, and the fact that one of the cases tested represents compressible flow whereas the analysis is strictly restricted to incompressible flow, it is concluded that the agreement is quite encouraging. Further checks and consideration of the results are planned.

V. SUMMARY OF RESULTS

1. The experimental investigation of spray detonations indicates that the time required for the development of the detonation wave increases as the spray drop size increases.

2. The difference between the experimental detonation velocity and the ideal C-J velocity at a corresponding equivalence ratio is found to be a function of the drop size. The larger the drop size, the higher the difference.

3. The velocity difference can be explained by taking into account heat transfer and shear losses to the tube wall within the reaction length, which is reasoned to be controlled by the breakup time of the fuel drops. There is some evidence that the coefficient of heat transfer reaches a peak at a distance behind the wave corresponding to the breakup time of the drops.

4. More details of the reaction zone have been obtained from "snapshot" schlieren photographs of the detonation in a single stream of 2600μ drops. The convective supersonic flow behind the main front produces a bow shock ahead of the drop and trailing shocks in its wake. Combustion in the wake results in explosion waves which apparently catch up with the main front. Pressure peaks corresponding to these waves have been observed.

5. No basic difference was found between the detonation of a low volatility fuel (DECH) and that of a high volatility fuel (benzene).

6. Detonations of a fuel film along one and two walls of the square tube were also investigated. The detonation velocity in the one wall case was lower (3500 ft/sec) than in the two walls case (4500 ft/sec) even though the equivalence ratios were .95 and .85 respectively.

7. Streak schlieren and direct light photographs with the slit near the wall showed ignition delays of 28-36 μsec for the one wall case and 7-19 μsec for the two wall case. The schlieren photographs showed evidence of periodic secondary shocks which catch up with the main front.

8. The shattering of inert drops by the convective flow behind controlled shock waves have been further studied by the use of streak photography. It was possible to define a quantitative breakup time based on the time the front of the drop reaches 95% of the convective flow. This time seems to correlate well with the previously rather subjective method based on examination of the shape of the shattered drop.

9. The action of the convective flow results in deforming the drops into a planetary ellipsoid with its major axis perpendicular to the direction of the flow.

10. An analysis of the breakup of the drop based on a boundary layer stripping model is completed and compared with experimental results.

APPENDIX

1. ELECTROMAGNETIC SHUTTER

Some photographs of the detonation phenomenon were taken with a schlieren spark source which has a duration of 0.2 μsec. The spark source can essentially act as its own shutter if the phenomenon to be photographed is not self luminous. In the case of two phase detonation considerable luminosity is present after the passage of the shock front. Direct radiation to the photographic plate can be reduced by a suitable stopper at the focal point of the second schlieren lens. The stopper would allow the schlieren light to pass through but would considerably restrict the direct light.

It was found that such a stopper was not adequate and therefore an electromagnetic shutter was used to reduce the exposure time of the direct radiation. The shutter was built in accordance with the design description of Pirroni and Stevens[6], and is shown in Fig. A-1. It consists of a stator, an armature and a slider mounted on a phenolic plate. The stator and armature are adjacent to each other so that when a current from a power supply is passed through them, the armature is repelled and thus provides a force to move the slider. The shutter time depends on the diameter of the holes in the slider and the plate and the speed of the slider. The slider speed during the time the two holes overlap, depends somewhat on the original position of the slider hole with respect to the fixed hole. A micrometric adjustment is provided to preset the slider at a desired position. This provides a mechanical time delay adjustment (a change of .025 in. = 100 μsec delay change).

The power supply and the triggering circuits are shown in Fig. A-2. The spark coil is energized by a pressure switch[3] actuated by the detonation. The spark source for the schlieren photograph is
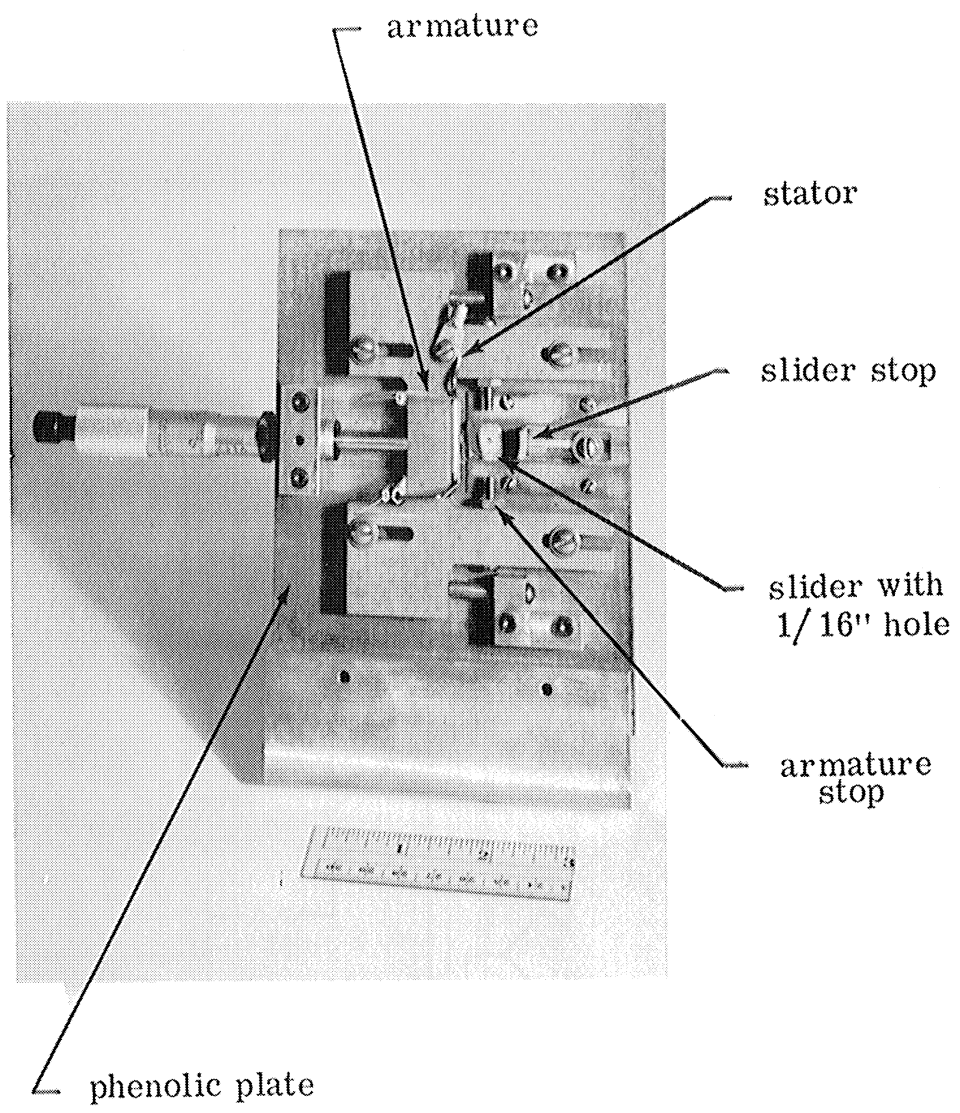
104

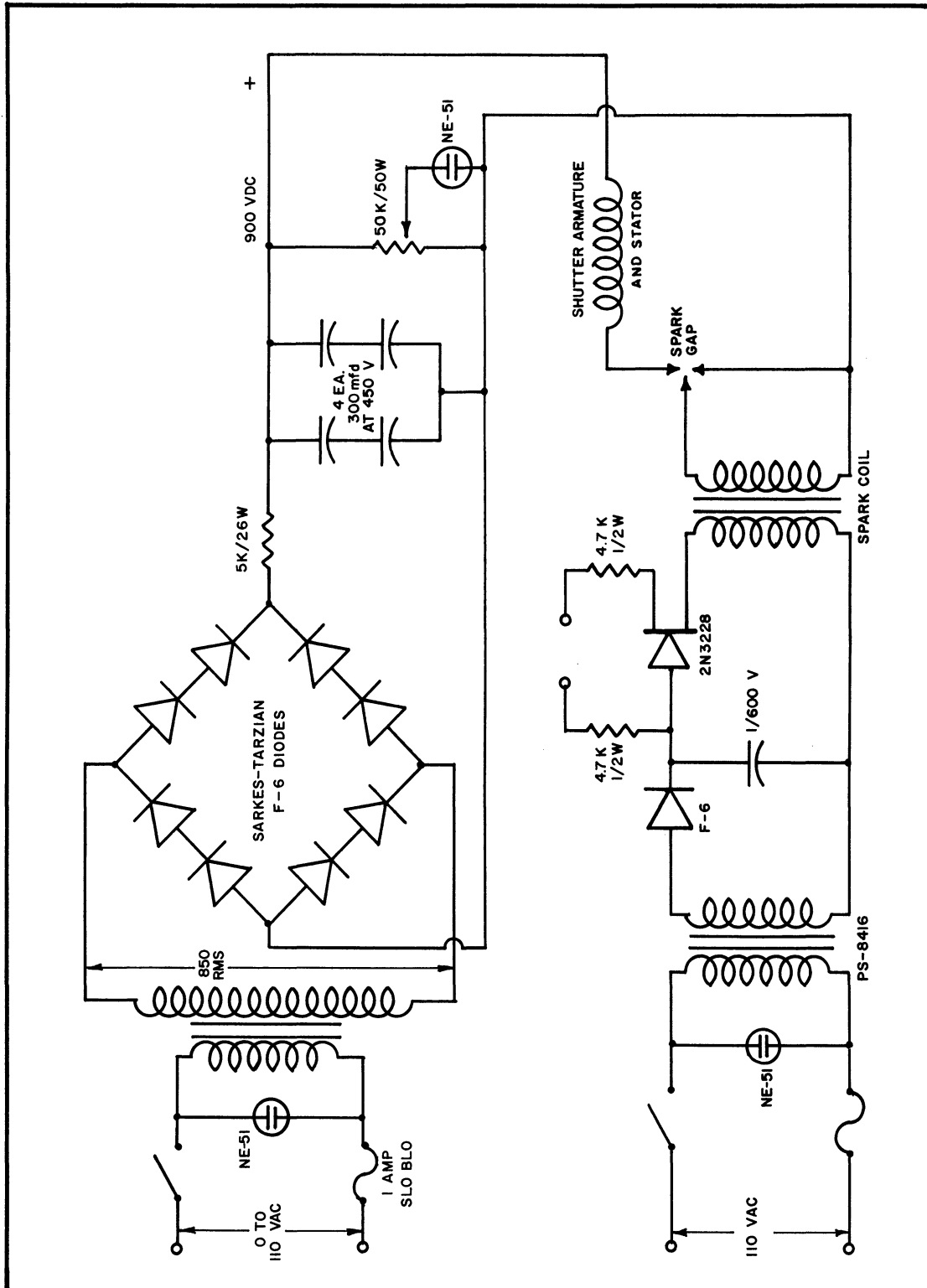Fig. A-1. Electromagnetic shutter picture.

Fig. A-2. Shutter power supply and triggering circuit.

106

timed so that it is discharged when the shutter is open. It was shown by Perroni and Stevens that the delay and the opening times for the shutter are repeatable. This was true of the shutter used in this work as shown by the oscillograph records in Fig. A-3a. Here the output of a photo diode subjected to a CW gas laser beam through the shutter is recorded. The half width time of the shutter opening (diameter = 1/16 in.) is about 250 μsec. Figure A-3b shows that the time before the shutter opens can be changed by the micrometer adjustment. The shutter proved very useful in obtaining schlieren photographs which are relatively free of direct radiation (see Fig. 2.5-2.6).

2. HEAT TRANSFER GAUGE AND CALIBRATION CIRCUIT

The heat transfer gauge that was used before[3] was adequate for waves travelling at M = 3-4, but could not withstand the pressure of higher Mach number waves. A more rugged version was therefore designed and built. This design is shown in Fig. A-4. The backing material is a 2 in. long quartz rod, 1/4 in. in diameter. The sensitive element is platinum which is bonded to the face of the rod along its diameter. Liquid platinum (Hanovia No. 05-X, Englehard Industries, Inc.) was used. On each side of the platinum strip, all along the rod length, a heavier coating of platinum alloy was painted on and baked (Hanovia No. 130-A). Then fine copper wires were soldered to each side strip thus providing the leads to the sensitive element. The rod is then covered by an insulating tube and housed in a modified Conax fitting and the wires were soldered to a BNC connector. An adaptor made of Teflon or Nylon was screwed to the pipe thread end of the Conax fitting and provided a means for flush mounting the gauge to the detonation tube.
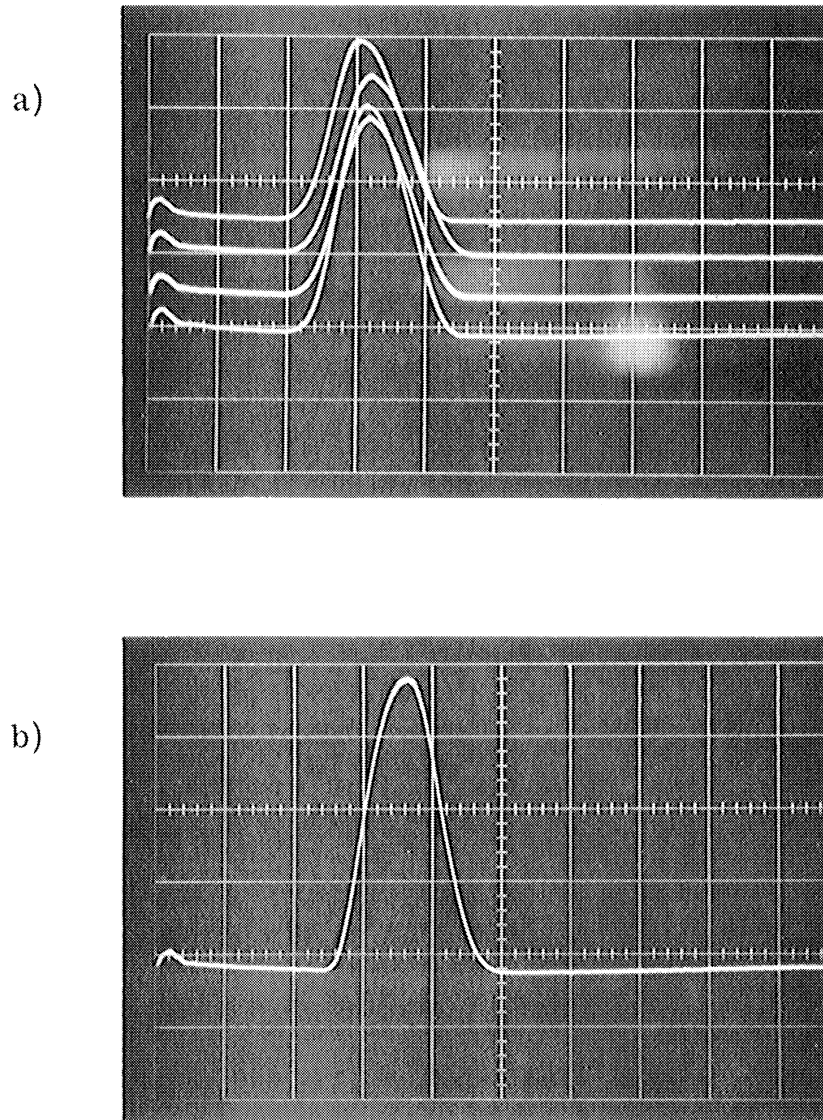
a)

b)

Fig. A-3. Shutter opening time, 200 μsec/div.
(a) Shows repeatability of opening time.
(b) Shows delay time can be changed by the
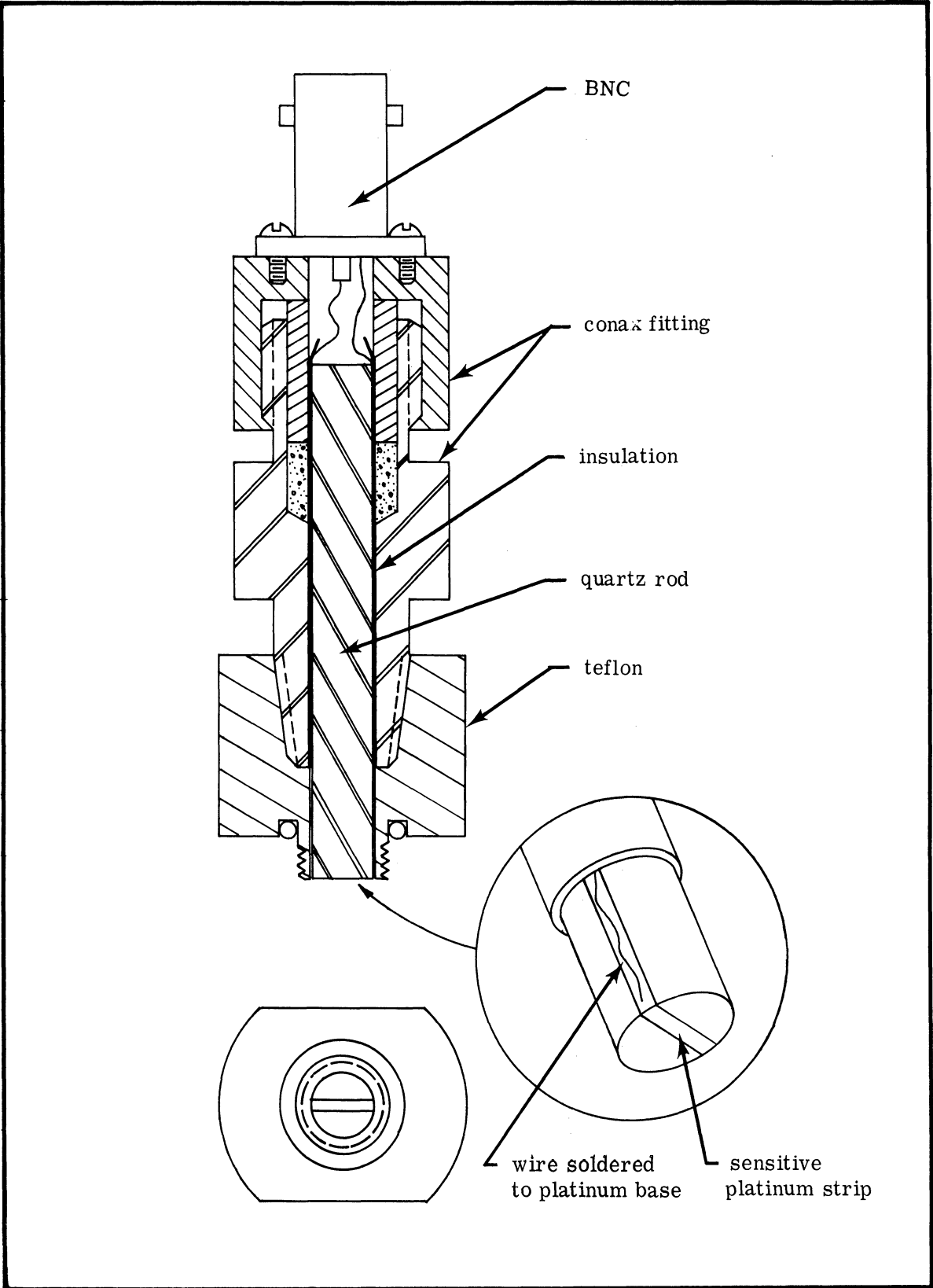micrometer adjustment.

Fig. A-4. Heat transfer gauge.

The proper use of the heat transfer gauge entails calibration of the specific resistivity, α, of the platinum film and a thermal property parameter, (ρck), of the backing material. The calibration of α can be made by simply noting the resistance change of the film with the temperature of water in which the gauge can be immersed. The calibration of (ρck) can be done as discussed by Skinner[23] when the gauge is subjected to a constant step heat flux, once when the gauge is in the free atmosphere and another time when the gauge is in water. Skinner shows that the (ρck) of the material can be inferred from the temperature response of the gauge under these two conditions assuming that the (ρck) of water is known.

An electric circuit for providing a constant heat flux was built after those of A. J. Laderman et al[24] and Scagnetti and Crabol[25]. This circuit is shown in Fig. A-5. The right part of the circuit, indicated by the dotted line, is used to balance the gauge in the bridge (this part is used also for α calibration) and the left hand part provides a relatively constant voltage input to the gauge as the time constant of the RC circuit is much greater than the calibration time.

The temperature response of the gauge to a constant heat flux is parabolic and this can be seen in the typical oscillograph record of Fig. A-6 which shows a repeatable response. The (ρck) calibration of quartz was not significantly different from the manufacturer's values.
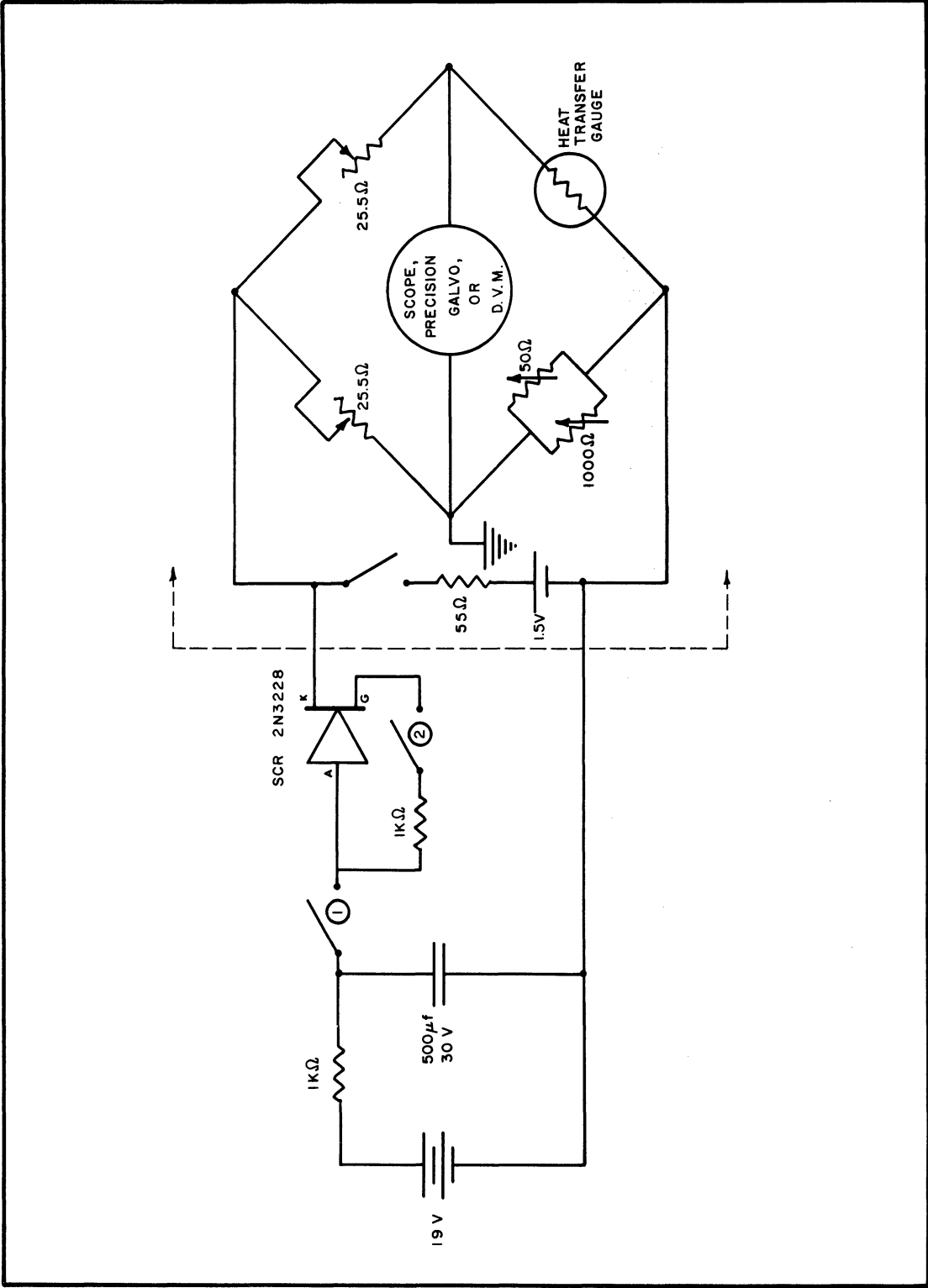
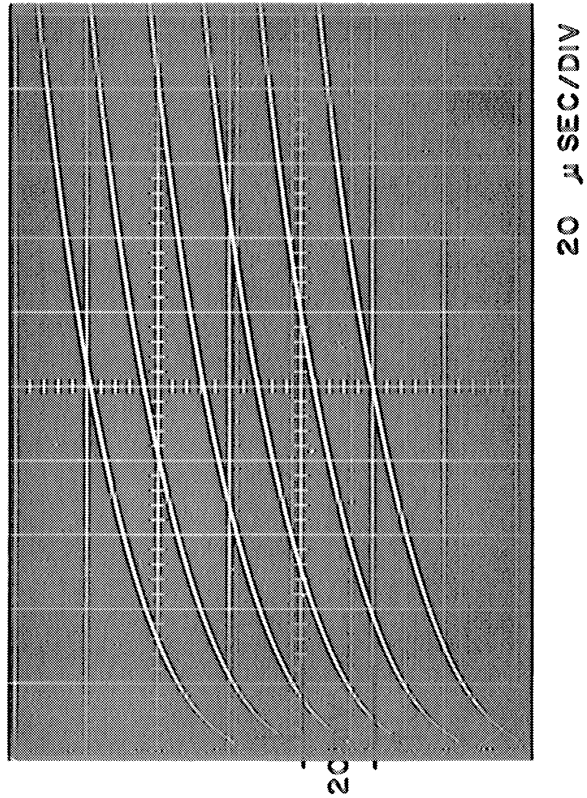Fig. A-5. Calibration circuit for heat transfer gauge.

Fig. A-6. Response of heat transfer gauge to step heat input.

REFERENCES

1. Nicholls, J.A., Dabora, E.K., and Ragland, K.W., "A Study of Two Phase Detonation as it Relates to Rocket Motor Combustion Instability," NASA CR-272, Aug. 1965.

2. Dabora, E.K., Ragland, K.W., Ranger, A.A., and Nicholls, J.A., "Two Phase Detonations and Drop Shattering Studies," University of Michigan, 06324-2-T, April 1966.

3. Dabora, E.K., Ragland, K.W., Ranger, A.A., and Nicholls, J.A.,"Two Phase Detonations and Drop Shattering Studies," NASA CR 72225, 1967.

4. Dabora, E.K., "Production of Monodisperse Sprays," Rev. Sci. Instr., 38, 502 (1967).

5. Ragland, K.W. and Cullen, R.E., "Piezoelectric Pressure Transducer with Acoustic Absorbing Rod," Rev. Sci. Instr., 38, 740-742 (June 1967).

6. Pirroni, J.S. and Stevens, R.R., "High Speed Electromagnetic Shutter," Rev. Sci. Instr., 38, 382 (1967).

7. Dabora, E.K., Ragland, K.W., and Nicholls, J.A., "A Study of Heterogeneous Detonations," Astronautica Acta, 12, 1966, p. 9.

8. Zeleznik, F.J. and Gordon, S., "A General IBM 704 and 7090 Computer Program for Computation of Chemical Equilibrium Compositions, Rocket Performance, and Chapman-Jouguet Detonations," NASA TN D 1454, Oct. 1962.

9. Ragland, K.W., The Propagation and Structure of Two Phase Detonations, Ph.D. Thesis, The University of Michigan, 1967.

10. Engel, O.G., "Fragmentation of Waterdrops in the Zone Behind an Air Shock," J. of Res. Nat'l. Bur. Standards, 60, No. 3, March 1958.

11. Nicholson, J.E. and Hill, A.F., "Rain Erosion on Spike Protected Supersonic Radomes," Mithras, Inc., Cambridge, Mass., MC-61-6-R3, April 1963.

12. Clark, B. J., "Breakup of a Liquid Jet in a Transverse Flow of Gas," NASA TN D-2424, Aug. 1964.

13. Jaarsma, F. and Derksen, W., "Shock Tube Techniques for Fuel Droplet Combustion Studies," National Aerospace Laboratory, the Netherlands. Paper presented at the 30th AGARD Meeting, Propulsion and Energetics Panel on "New Experimental Techniques in Propulsion and Energetics Problems," Munich, Germany, Sept. 1967.

14. Portalski, S., "Studies of Falling Liquid Film Flow," Chem. Eng. Sci., 18, 787-804 (1963).

15. Morrison, R. B., "A Shock Tube Investigation of Detonative Combustion," Report UMM 97, The Univ. of Mich., Jan. 1952.

16. Komov, V. F. and Troshin, Ya. K., "The Structure and Detonation Mechanism of Heterogeneous Systems," Proceedings of the Academy of Science, USSR, 162, 1 (Physical Chemistry), 1965.

17. Borisov, A. A., Kogarko, S. M., and Lyubimov, A. V., "Ignition of Fuel Films Behind Shock Waves in Air and Oxygen," Eleventh Symposium (International) on Combustion, The Combustion Institute, Pittsburg, Pa., 1967.

18. Borisov, A. A., Kogarko, S. M., and Lyubimov, A. V., "Sliding of Detonation and Shock Waves on a Liquid Surface," Fizika Goreniya i Vzryva, No. 4, 1965 (Translated JPRS 36,674, 25 July 1966, U. S. Dept. of Commerce).

19. Borisov, A. A., Kogarko, S. M., and Lyubimov, A. V., "Instability of a Liquid Surface Along Which Detonation and Shock Waves are Sliding," Proceedings of the Academy of Science, USSR, 164, 1 (Physical Chemistry) (1965), p. 125-127.

20. Ragland, K. W., "Solution of the Blasius Boundary Layer Equation with Vaporization and Combustion at the Wall," NASA CR 72235, July 1967.

21. Taylor, G. I., "The Shape and Acceleration of a Drop in a High-Speed Air Stream," The Scientific Papers of G. I. Taylor, Edited by G. K. Batchelor, Vol. III, University Press, Cambridge, (1963).

22.   Morrell, G. , "Rate of Liquid Jet Breakup by a Transverse Shock
       Wave," NASA TN D-1728, May, 1963.

23.   Skinner, G. T. , "Calibration of Thin Film Gage Backing Materials, "
       ARS J. , 31, No. 5, May 1961, pp. 671-672.

24.   Laderman, A. J. , Hecht, G. J. , and Oppenheim, A. K. , "Thin Film
       Thermometry in Detonation Research, " Temperature — Its Measure-
       ment and Control in Science and Industry, 3, Pt. 2, 1962.

25.   Scagnetti, M. and Crabol, J. , "Sondes Thermométriques a Film
       de Platine a Réponse Rapide, " ONERA Report No. 83 (1963).

DISTRIBUTION LIST

NASA Lewis Research Center
21000 Brookpark Road
Cleveland, Ohio 44135
Attention: B. J. Clark (3)

NASA Lewis Research Center
21000 Brookpark Road
Cleveland, Ohio 44135
Attention: Library (2)

National Aeronautics and Space
  Administration
Washington, D. C. 20546
Attention: Office of Grants and
              Contracts (10)

NASA Goddard Space Flight Center
Greenbelt, Maryland 20771
Attention: Library

Jet Propulsion Laboratory
4800 Oak Grove Drive
Pasadena, California 91103
Attention: Library

NASA Manned Spacecraft Center
Houston, Texas 77001
Attention: Library

NASA Western Operations
150 Pico Blvd.
Santa Monica, Calif. 90406
Attention: Library

Applied Physics Laboratory
The Johns Hopkins University
Attn: W. G. Berl
8621 Georgia Avenue
Silver Spring, Maryland 20910

Princeton University
Forrestal Campus
Guggenheim Laboratories
Attn: I. Glassman
Princeton, New Jersey 08540

NASA Scientific and Technical
    Information Facility
Box 5700
Bethesda, Maryland
Attention: NASA Representative (6)

NASA Lewis Research Center
21000 Brookpark Road
Cleveland, Ohio 44135
Attention Report Control Office

NASA Ames Research Center
Moffett Field, California 94035
Attention: Library

NASA Flight Research Center
P. O. Box 273
Edwards, California 93523
Attention: Library

NASA Langley Research Center
Langley Station
Hampton, Virginia 23365
Attention: Library

NASA Marshall Space Flight Center
Huntsville, Alabama 35812
Attention: Library

Chemical Propulsion Information
    Agency
Attn: T. W. Christian
8621 Georgia Avenue
Silver Spring, Maryland 20910

University of Southern California
Dept. of Mechanical Engineering
Attn: M. Gerstein
University Park
Los Angeles, California 90007

Rocketdyne
A Div. of North American Aviation
Attn: E. C. Clinger
6633 Canoga Avenue
Canoga Park, California 91304

NASA Lewis Research Center
Attn: E. W. Conrad
21000 Brookpark Road
Cleveland, Ohio 44135

U. S. Naval Ordnance Test Station
Attn: D. Couch
China Lake, California 93555

Multi-Tech., Inc.
Attn: F. B. Cramer
601 Glenoaks Blvd.
San Fernando, California 91340

Aerospace Corporation
Attn: O. W. Dykema
P. O. Box 95085
Los Angeles, California 90045

Ohio State University
Dept. of Aeronautical and Astronautical
  Engineering
Attn: R. Edse
Columbus, Ohio 43210

TRW Systems
Attn: G. W. Elverum
1 Space Park
Redondo Beach, California 90278

University of Illinois
Aeronautical and Astronautical
  Engineering
Urbana, Illinois
Attn: R. A. Strehlow

NASA Headquarters
Attn: R. S. Levine, Code RPL
6th and Independence Avenue, S. W.
Washington, D. C. 20546

Pratt and Whitney Aircraft
Florida Research and Development Ctr.
Attn: G. D. Lewis
P. O. Box 2691
West Palm Beach, Florida 33402

Defense Research Corporation
Attn: B. Gray
P. O. Box 3587
Santa Barbara, California 93105

Princeton University
Forrestal Campus
Guggenheim Laboratories
Attn: D. Harrje
Princeton, New Jersey 08540

Aerojet-General Corporation
Attn: R. J. Hefner
P. O. Box 15847
Sacramento, California 95809

Dynamic Science Corporation
Attn: B. P. Breen
1900 Walker Avenue
Monrovia, California 91016

Office of Naval Research
Navy Department
Attn: R. D. Jackel, 429
Washington, D. C. 20360

Rocketdyne
A Div. of North American Aviation
Attn: R. B. Lawhead
6633 Canoga Avenue
Canoga Park, California 91304

Colorado University
Attn: C. E. Mitchell
Boulder, Colorado

NASA Lewis Research Center
Attn: R. J. Priem, MS-86-5
21000 Brookpark Road
Cleveland, Ohio 44135

Sacramento State College
Engineering Division
Attn: F. H. Reardon
60000 J. Street
Sacramento, California 95189

Thiokol Chemical Corporation
Reaction Motors Division
Attn: D. Mann
Denville, New Jersey 07834

Dartmouth University
Attn: P. D. McCormack
Hanover, New Hampshire 03755

University of Wisconsin
Mechanical Engineering Department
Attn: P. S. Myers
1513 University Avenue
Madison, Wisconsin 53705

University of California
Department of Chemical Engineering
Attn: A. K. Oppenhiem
6161 Etcheverry Hall
Berkeley, California 94720

Purdue University
School of Mechanical Engineering
Attn: J. R. Osborn
Lafayette, Indiana 47907

United Technology Center
Attn: R. H. Osborn
P. O. Box 358
Sunnyvale, California 94088

U. S. Naval Ordnance Test Station
Attn: E. W. Price, Code 508
China Lake, California 93555

Massachusetts Institute of Technology
Department of Mechanical Engineering
Attn: T. Y. Toong
Cambridge, Massachusetts 02139

Illinois Institute of Technology
RM 200 M. H.
Attn: T. P. Torda
3300 S. Federal Street
Chicago, Illinois 60616

NASA
George C. Marshall Space Flight Center
R-P and VE-PA, Attn: R J. Richmond
Huntsville, Alabama 35812

Bell Aerosystems Company
Attn: L. M. Wood
P. O. Box 1
Buffalo, New York 14205

Jet Propulsion Laboratory
California Institute of Technology
Attn: J. H. Rupe
4800 Oak Grove Drive
Pasadena, California 91103

University of California
Mechanical Engineering, Thermal Sys.
Attn: R. Sawyer
Berkeley, California 94720

ARL (ARC)
Attn: K. Scheller
Wright-Patterson AFB
Dayton, Ohio 45433

Institute of Defense Analysis
Attn: W. C. Strahle
Washington, D. C.

NASA Manned Spacecraft Center
Attn: J. G. Thibadaux
Houston, Texas 77058

Geophysics Corporation of America
Technology Division
Attn: A. C. Tobey
Burlington Road
Bedford, Massachusetts 01730

AFRPL (RPRR)
Attn: B. R. Bornhorst
Edwards, California 93523

U. S. Army Missile Command
AMSMI-RKL, Attn: W. W. Wharton
Redstone Arsenal, Alabama 35808

University of California
Department of Aerospace Sciences
Attn: F. A. Williams
La Jolla, California

The Warner and Swasey Company
Control Instrument Division
Attn: R. H. Tourin
32 - 16 Downing Street
Flushing, New York 11354

United Aircraft Corporation
Research Labs.
Attn: D. H. Utvick
400 Main Street
East Hartford, Connecticut 06108

General Electric Company
Schnectady, New York
Attn: D. R. White

Air Force Office of Scientific Research
Attn: B. T. Wolfson
1400 Wilson Blvd.
Arlington, Virginia 22209

Georgia Institute of Technology
Aerospace School
Attn: B. T. Zinn
Atlanta, Georgia 30332